

## ABSTRACT

SHUZHEN, WEI. Bioinspired Electrically Active Bistable Actuator. (Under the direction of Dr. Tushar K. Ghosh and Dr. Wei Gao).

Dielectric elastomer (DE) and bistable sheet are introduced as an actuator material and an efficient actuator structure in this dissertation. Dielectric elastomer is a type of electroactive polymers (EAPs) intensively investigated as a highly deformable material under electric field. Bistable structure has two stable shapes and mechanical instability in between. When subjected to an activation energy sufficient for snap-through, the structure self-equilibrates to and self-stabilizes in the other stable configuration. With incorporation of DE material into bistable structure, the induced deformation of DE is converted to bistable shape transformation of the actuator. Natural analogs of specialized actuators include bistable leave of Venus Flytrap with rapid closure speed [1], raptorial appendage of Mantis shrimp with ultrafast movement [2], and salamander's tongue enabled with extreme extrusion speed and precision at the target [3].

Inspired by these biological actuators, this work presents a novel multilayered bistable architecture originated from anisotropic strain field, which is reconfigured through DE actuation that triggers the bistable shape transformation. The bistable laminate with two orthogonal curvatures is fabricated through asymmetrically prestraining two DE films and attaching to a support film with higher stiffness. Both experiment and theoretical model are presented for studying the bistable shape and bistability of this laminated actuator, in which actuator's dimension, prestrains of DE layers and support layer stiffness are varied. The laminated actuator exhibits tunable bistable shape by changing prestrains or support layer stiffness. DE actuation is performed on one of the DE layers in the laminate, to activate the bistable shape

transformation. The electrical actuation of bistable actuators is evaluated by changing the prestrains of DE layers, electrode position and size. Upon activation, the actuator snaps from one shape to the other, generating a blocking force of around 4.5 mN.

© Copyright 2018 by Shuzhen Wei

All Rights Reserved

Bioinspired Electrically Active Bistable Actuator

by  
Shuzhen Wei

A thesis submitted to the Graduate Faculty of  
North Carolina State University  
in partial fulfillment of the  
requirements for the degree of  
Master of Science

Textile Chemistry

Raleigh, North Carolina

2018

APPROVED BY:

---

Dr. Tushar K. Ghosh  
Committee Co-Chair

---

Dr. Wei Gao  
Committee Co-Chair

---

Dr. Ericka Ford

## **DEDICATION**

To my parents, my boyfriend, and my advisor for their love and unconditional support.

## **BIOGRAPHY**

Shuzhen Wei was born in China and she received her Bachelor's degree in 2016 in Textile Chemistry from Jiangnan University, China. She participated in Chinese National Undergraduate Research in Jiangnan University, with research project aimed at bleaching cotton fabric at low temperature.

In the fall of 2015, she joined North Carolina State University via 3+x program as a senior student, and then transferred to Master's program in Textile Chemistry in the spring of 2016. During Master's period, she worked under the direction of Prof. Tushar K. Ghosh, on bi-stable dielectric elastomer.

## **ACKNOWLEDGMENTS**

I would like to thank my advisor Prof. Tushar K. Ghosh for his motivation and support during my Master's study. This research is my first formal and professional research experience where I am intensively exposed to new disciplines and science frontiers. Prof. Ghosh motivated me to think broader and deeper, and always supported me in my experimental ideas, research problems as well as issues in daily life.

I am grateful for the great opportunity NCSU gave me. This diverse community provided such brilliant research and living environment for students, and brought great people together. In this big community, our lab is like a small and warm home. I am thankful to my fellow labmates, Ashish Kapoor, Kony Chatterjee, Jordan Tabor, Xiaomeng Fang, Huiqi Shao and Aaloka Kotwal. They accompanied me during every hard time in my research journey, and gave me huge support and caring in many aspects.

Lastly, I want to thank my parents, my young brother, my boyfriend Bill, and Jesus my God. They are my comforters and intimate companions forever.

## TABLE OF CONTENTS

LIST OF TABLES .....	vi
LIST OF FIGURES .....	vii
Chapter 1 Introduction .....	1
Chapter 2 Background .....	3
2.1 Electroactive Polymer .....	3
2.1.1 Dielectric Elastomer .....	4
2.1.2 Dielectric Elastomer Actuators.....	11
2.2 Morphing Multistable Structures .....	22
2.2.1 Morphing Structures in Nature .....	24
2.2.2 Manmade Morphing Structures.....	30
Chapter 3 Bioinspired Dielectric Bistable Actuator .....	38
3.1 Introduction .....	39
3.2 Experimental .....	41
3.2.1 Parameter definition .....	41
3.2.2 Materials.....	42
3.2.3 Fabrication of tape spring DEBA.....	45
3.2.4 Experimental methods .....	46
3.3 Results and Discussions.....	50
3.3.1 Bistable shape of tape spring DEBA.....	50
3.3.2 Bistability analysis of tape spring DEBA.....	63
3.3.3 Electromechanical response of tape spring DEBA .....	65
3.3.4 Blocking force of the tape spring DEBA .....	70
3.4 Conclusion .....	72

<b>Chapter 4 Conclusion and Future Perspectives .....</b>	<b>73</b>
<b>REFERENCES .....</b>	<b>75</b>
<b>Appendix A Theoretical Analysis of Bistable Shape .....</b>	<b>83</b>
<b>Appendix B Theoretical Analysis of Bistability .....</b>	<b>85</b>

## LIST OF TABLES

Table 2-1.	Important properties of three typical dielectric materials.....	10
Table 2-2.	List of multistable structure categories, mechanisms and examples.....	35
Table 3-1.	Parameter definition.....	42
Table 3-2.	Properties and dimensions of DEBA films .....	44
Table 3-3.	Properties of compliant electrodes .....	45
Table 3-4.	Effect of prestrains on the bistable shape of tape spring DEBA.....	54
Table 3-5.	Effect of support layer stiffness on the bistable shape of tape spring DEBA. “-” means no reading because the sample is monostable in state 2 (cannot self-equilibrate in state 1) .....	60
Table 3-6.	Effect of prestrain on the snap-through of tape spring actuator (25 $\mu$ m thick PET is utilized as support layer) .....	68

## LIST OF FIGURES

Figure 2-1.	Schematic of dielectric elastomer actuation .....	5
Figure 2-2.	Comparison of actuation performances of actuator materials[35], [36] .....	6
Figure 2-3.	Examples of linear DEA[61], [74], [75] .....	14
Figure 2-4.	Examples of bending DEA[47], [50], [63], [76] .....	17
Figure 2-5.	Examples of rotational DEA[77]–[79] .....	20
Figure 2-6.	Summary of the methods to enhance the actuation performance via DEA design	21
Figure 2-7.	Energy diagrams of bistable structures .....	24
Figure 2-8.	Bistable morphing structures of plants[1], [87], [88] .....	27
Figure 2-9.	Morphing behaviors of animals[3], [89], [90] .....	29
Figure 2-10.	Bending behavior of synthetic morphing structure [102] [105] [108] .....	32
Figure 2-11.	Synthetic multistable structures[19], [104], [113] .....	36
Figure 3-1.	Stress-strain curve of VHB 4905 .....	42
Figure 3-2.	Adhesiveness of the middle electrode (between support layer and bottom DE layer) .....	44
Figure 3-3.	Fabrication of tape spring DEBA. (a) The top and bottom DE films are prestretched orthogonally, with a stiff support layer in the middle. A pair of compliant electrodes sandwich the bottom DE film for electric actuation. (b) The three layers are attached and cut along the dotted line, with a zoom-in shape in (c). After the removal of external constraints, the laminate self-equilibrates into (d) state 1 and, (e) state 2 .....	46
Figure 3-4.	Experimental flow of tape spring DEBA characterization. The flows in brackets (1) (2) (3) represent bistable shape characterization, dielectric actuation and blocking force measurement, respectively .....	47
Figure 3-5.	Bistable shape characterization of tape spring DEBA. (a) Schematic of two cameras in xz plane and yz plane. (b) Stage and camera setup for shape capturing. (c) Manually snapping the tape spring DEBA by tweezers. (d) A series of DE samples with $\epsilon_{xb}$ as the variable .....	48
Figure 3-6.	Electric actuation of tape spring DEBA. (a) tape spring DEBA sample. (b) Electric actuation setup. (c) Two steps of actuator movement: actuation step and	

snapping step.....	49
Figure 3-7. Schematic of blocking force measurement .....	50
Figure 3-8. Effect of actuator dimension on the bistable shape .....	52
Figure 3-9. Effect of prestrains on the bistable shape. The $C_{xz}$ (solid black line, ■), $S_{yz}$ (solid blue line, ▲) and calculated $C_{xz}$ (dotted black line, ●) change as we changed (a) prestrain in x direction in the bottom layer ( $\epsilon_{xb}$ ), (b) prestrain in y direction in the bottom layer ( $\epsilon_{yb}$ ), and (c) prestrain in the y direction in the top layer ( $\epsilon_{yt}$ ), while other prestrains were kept constant. Filled symbols represent bistable samples, and unfilled symbols represent monostable samples.....	56
Figure 3-10. The effect of support layer stiffness on the bistable shape. PET ( $E=4.9\text{GPa}$ ) and PI ( $E=2.5\text{GPa}$ ) as support layers. $C_{xz}$ (■) and $S_{yz}$ (▲) of the tape spring actuator with PET (dash line), and PI (solid line) as support layer plotted as a function of, (a) x-direction prestrain in the bottom layer ( $\epsilon_{xb}$ ), while $\epsilon_{xt}=0\%$ , $\epsilon_{yb}=80\%$ , $\epsilon_{yt}=200\%$ are held constant, and (b) x-direction prestrain in the bottom layer ( $\epsilon_{xb}$ ), while $\epsilon_{xt}=0\%$ , $\epsilon_{yb}=100\%$ , $\epsilon_{yt}=200\%$ are held constant. Filled symbols represent bistable samples, and unfilled symbols represent monostable samples.....	61
Figure 3-11. Prestrain-dependent bistability of the tape spring DEBA. (a) Change of moment of inertia about x axis in state 1 ( $I_x$ ), as we changed prestrains in DE layers. (b,c) Bistability of the prestrained tape spring laminates illustrated by the range of (b) $C_{yz}$ in state 1, and (c) the division of bending moment about x axis ( $M_x$ ) and bending moment about y axis ( $M_y$ ). Solid dots represent bistable samples, and unfilled dots represent monostable samples .....	64
Figure 3-12. Dielectric polymer based bistable tape spring actuation mechanism. (a) Schematic illustration of a dielectric polymer actuation mechanism. (b) Optical images showing the electric actuation process of a flat DE actuator and our tape spring DEBA. The biaxial prestrains of the flat actuator is the same as the biaxial prestrains on the bottom DE film of the tape spring DEBA.....	66
Figure 3-13. Influence of prestrain on the snap-through of tape spring actuator. The $\epsilon_{xb}$ is a variable while other prestrains are kept constant ( $\epsilon_{yt}=200$ , $\epsilon_{yb}=80$ , $\epsilon_{xt}=0$ ) (25 $\mu\text{m}$ thick PET is utilized as support layer).....	68
Figure 3-14. Influence of electrode position on the snap-through of tape spring actuator .....	69
Figure 3-15. Influence of electrode size on the snap-through of tape spring actuator .....	70
Figure 3-16. Blocking force of tape spring actuator. Prestrains of the actuator were kept at $\epsilon_{xb}=60\%$ , $\epsilon_{yb}=80\%$ , $\epsilon_{xt}=0\%$ , $\epsilon_{yt}=200\%$ .....	71

## Chapter 1 Introduction

Nature is full of ingenious sustainable solutions to problems spanning all aspects of human need. Human beings as one part of nature have learnt from and imitated nature to create useful tools and technologies, from reed-inspired sickle by Lu Ban in ancient China, to bird-inspired aircraft by the Wright brothers in 1903 [4]. It is important to improve our understanding of natural design for technological advancement and sustainable living. In the field of actuators (a component in the control system responsible for converting input energy into mechanical motion), conventional means consist of mostly pneumatic or electromagnetic actuation, i.e. producing all types of motion by using pressurized fluids, or electromagnetic field. However, such means are generally noisy, insufficient, and are restricted by limited input energy types and bulky peripheral components or overhead. Interestingly, natural actuators such as skeletal muscles, motor cells and even dead tissues generate many movements in plants and animals, with least amount of materials and naturally available energies.

Inspired by natural actuators, soft active materials and structures have been explored to substitute for the conventional actuators in some areas such as robotics [5]–[8], biomedical devices [9], and wearable assistive devices [9], [10]. With regard to active materials, shape memory alloys (SMAs) [11], [12], piezoelectric materials [13], [14] and electroactive polymers (EAP) [15], [16] are currently under intensive investigation. Dielectric elastomers (DE) featuring in low modulus and large strain, relatively high dielectric constant as well as high energy density constitute one important category of EAPs. With the development of responsive materials, one of the main challenges is how to incorporate these materials in innovative designs to controllably utilize their shape-change properties. Potential solutions being explored including

active material/stimuli allocation [17], [18] and actuator structural design [19]–[21]. One of the best examples of natural motion is that produced by the Venus Flytrap (VFT). The sudden closure (within 0.1 second) of the VFT is prompted by sudden change of turgor pressure that activates the bistable shape transformation of the leaves. Such bistability and morphing in nature is of great interest to the scientists because of their practical utility. Morphing multistable structures (denoted as morphing MS) undergo swift shape transformation upon activation, due to the mechanical instability between multiple stable shapes. The potential applications of morphing MSs include modulation of flight condition of aircrafts [22]–[24], vibration energy harvesting [25], [26], and wind turbine design for fracture minimization [27].

This work presents a novel polymer-based bistable actuator inspired by the VFT and salamander's tongue. The actuator is a laminated structure with two prestrained active layers that induces bistability of the shape. The bistable shape transformation is achieved by an applied electric field to the active layers.

Following the introduction in Chapter 1, this dissertation provides the background for this work in Chapter 2. The background covers an important category of responsive material - electroactive polymers (EAP) - with a particular focus on dielectric elastomers (DE). Further in Chapter 2, a review of the natural/biological design of adaptive structures, as well as their bioinspired counterparts with emphasis on the morphing MSs is presented. In Chapter 3, a novel design and fabrication of a polymer-based laminate with a tunable and predictable bistable shape, as well as its transformation is discussed. Chapter 4 contains a summary of this research as well as perspectives for future investigations.

## Chapter 2 Background

### 2.1 Electroactive Polymer

Known as artificial muscles, electroactive polymers (EAP) are composed of a variety of polymers that deform under an applied electric field. They combine favorable polymeric properties such as being flexible and lightweight, and electrical properties suitable for electrical actuation.

EAPs consist of two distinct classes based on their actuation mechanisms; electronic and ionic. Ionic EAPs undergo deformation when ions are subjected to an external electric field causing them to migrate directionally within the polymer matrix, resulting in an expansion on the ion accumulation side and shrinkage on the ion reduction side. This causes the ionic EAP film or strip to undergo bending. The materials for ionic EAPs include carbon nanotubes [28], electrically conductive polymers [29], electrorheological fluids [30], ionic polymer gels [16], and ionic polymer metallic composites [31]. On the other hand, electronic EAPs involve polarization reorientation, or Coulomb force induced motion due to the applied electric field. Five types of electromechanical effects including piezoelectric, ferroelectric, pyroelectric, electrostrictive and electrostatic effect, are caused by the electrical polarization capacity of the materials (orientation of polar groups in the polymer chain under electric field). Both electrostrictive and electrostatic effects always exist in dielectric materials, with electrostrictive shape change dominating at moderate electric fields, and electrostatic effects becoming significant at higher electric fields [32]. For example, polyurethane under electric field was observed to exert both electrostatic (up to 100MV/m) and electrostrictive (up to 10MV/m) effects [32], [33]. Electronic

EAPs include DEs, electrostrictive graft elastomers, electrostrictive papers, electro-viscoelastic elastomers, ferroelectric polymers, and liquid crystal elastomers [34].

In comparison, ionic EAPs offer the advantage of being able to undergo large deformations under small applied electric potential (2-7V) [34], but are restricted by their requirement of fluid for ion migration. Electronic EAPs can operate in ambient conditions, but require high electric fields (10-100V/ $\mu\text{m}$ ) [34]. Apart from the actuation characteristics, Figure 2-2 presents other key factors to consider in a competitive actuator material; actuation strain, actuation stress, and energy density [35], [36]. Dielectric elastomers (DE) form an important group within the electronic EAPs and stand out because of their large actuation strain and high energy density, and other desirable properties. The work presented here makes use of the unique properties of DE, therefore the following discussion is focused on the DE materials and DE-based actuators (DEA).

### 2.1.1 Dielectric Elastomer

DEs are known for achieving large induced strains under applied electric fields. The mechanism of deformation of DEs can be best explained using a simple parallel plate capacitor with a DE film as the medium placed between two soft compliant electrodes, see Figure 2-1. Upon application of the electric field, opposite charges in the electrodes attract each other and develop a compressive stress on the dielectric medium, while like charges on the same electrode repel each other. The resulting compressive stress (Maxwell stress) experienced by the DE can be expressed as [37].

$$\sigma = \epsilon_0 \epsilon_r E^2 = \epsilon_0 \epsilon_r (V/d)^2 \quad \text{Equation 2-1}$$

Here,  $\epsilon_0$  and  $\epsilon_r$  are the dielectric permittivity of free space and relative permittivity of the DE film respectively, and  $E$  is the applied electric field.  $V$  is applied voltage, and  $d$  is the thickness of the dielectric medium. The compliant electrode materials used for DEs include carbon black, graphite, carbon grease, CNT in various forms, electrolytes, and conducting polymers [38]–[41].

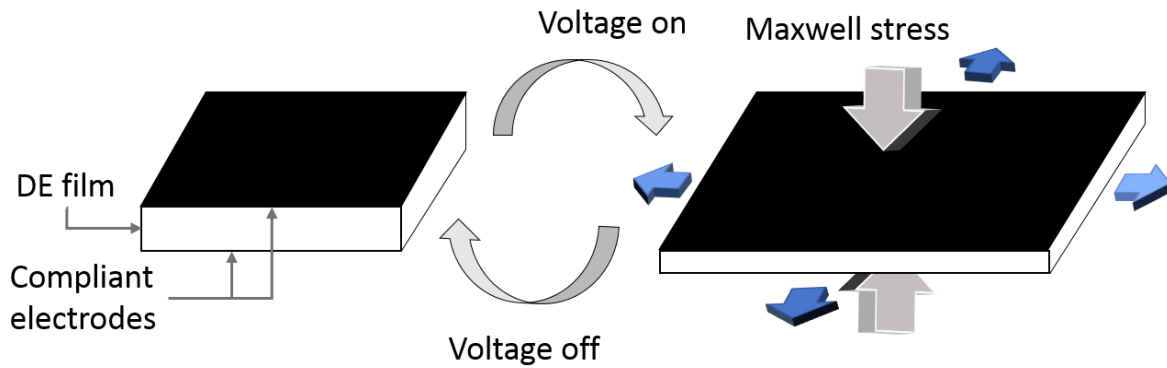


**Figure 2-1. Schematic of dielectric elastomer actuation.**

DEs have been intensively studied in recent three decades. However the discovery of DE actuation can be tracked back to 1880, when the German physicist Rontgen found that rubber strip undergoes compressive deformation under an electric field [42]. About a century later, the electro-mechanical behavior of DEs was intensively analyzed and incorporated into spatial light modulator to control the light waves in space and time [43], which enhanced the HDTV projection technology [44]. At the turn of 21st century, the investigation of DEs had attracted great attention in various disciplines, and being considered as a competitive actuator material. Scientists at the SRI international [35] compared DEs with some popular active materials, and showed high energy density and actuation strain of DE, which is comparable to the natural

muscle (Figure 2-2a). Shankar et al [36] updated these important actuator performance parameters in 2007 and presented an important enhancement of actuation performance of DE materials (Figure 2-2b). Some of the pioneering research in the late 1990s and at the turn of the century [34], [37], [45], [46], [47], [48], [49], [50] led the way toward broader participation of the scientific community from many disciplines in DE related research. Since then, significant progress has taken place in DE materials, modeling, and DEA applications.

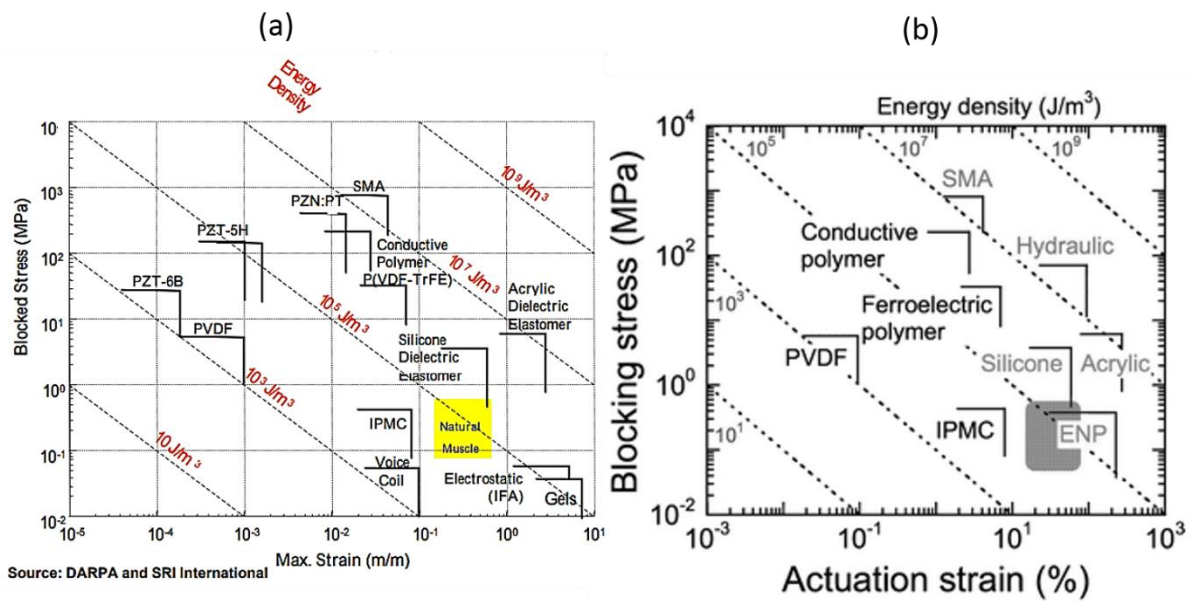


**Figure 2-2. Comparison of actuation performances of actuator materials [35], [36].**

The landscape of DE materials includes three primary elastomers, acrylate, silicone, and polyurethane. Other reported DE materials include thermoplastic block copolymers [15], [51], and chemically modified polymer compositions with tunable crosslink density [52], interpenetrating networks [53], etc.

Acrylic elastomers have the advantages of both mechanical and electrical properties to produce large actuation strain, compared to other dielectric elastomers. The most commonly

investigated acrylic elastomer is the VHB brand of adhesive tapes (3M VHB™ adhesive) manufactured by the 3M corp. The VHB tape is commercially available in various thicknesses and has been explored often due to its high elasticity, moderate dielectric constant, large actuation strain, and excellent adhesiveness. It offers a range of desirable properties such as Young's modulus lower than 1MPa, large strain at break (more than 500%), electrically induced areal strain up to 380% [49], high dielectric constant from 4-6 [54], high dielectric strength of 25V/μm for non-prestretched film and 215V/μm for prestretched ones [49], high energy density of 3.4 MJ/m<sup>3</sup>[45], and good thermal stability from -10 to 80°C[55]. An important characteristic of the VHB is its adhesiveness. DE films are normally pretrained to reduce their thickness in order to reduce electric potential for actuation while improving dielectric breakdown strength and actuation strain by suppressing electromechanical instability (EMI) [56]. Dielectric breakdown occurs when the driving voltage reaches a level where the electric current flows through the DE material, causing the material to fail. EMI of a DE - also referred to as pull-in effect - is due to the synergetic effect of both electric field increase and film thickness decrease, especially for strain-softening materials [56]. DE film is generally attached to a rigid frame in order to maintain the prestrain. In case of the VHB film, the material of rigid frame is selected according to the bonding strength of the VHB film and substrate surface. The materials with high surface energy such as metal, glass, polyimide, polyester, etc. [55] have high bonding strength to the VHB and thus can be utilized as the support frame.

Although VHB tape is good for assembling into actuators, it is known to undergo viscoelastic relaxation manifesting in significant mechanical hysteresis. Mechanical loss in prestretched film due to stress decay over time, results in poor performance reproducibility

[57]. Due to high viscoelastic effect, it is limited in terms of deformation speed and frequency-response during electrical actuation. The elastic modulus of VHB 4910 drops dramatically with the temperature increment from  $-25^{\circ}\text{C}$  to  $75^{\circ}\text{C}$ , while the silicone retains its modulus almost unchanged [57].

Polydimethylsiloxane (PDMS) elastomer or silicone, commercially available in a large variety of properties is another important material being studied as a potential DE. The backbone of silicone is composed of alternate covalently bonded silicon atoms and oxygen atoms - providing unique properties. It exhibits good elasticity with a wide range of Young's modulus, hydrophobicity, low chemical reactivity, high temperature stability, electrical insulation, and high electromechanical speed for some silicone materials [57].

Certain classes of polyurethanes (PU) display both electrostrictive and electrostatic behavior [32], [58]–[60]. The PU molecule is composed of hard segments and soft segments enabling stiffness (crystals in hard segment region) and flexibility (amorphous region of soft segments), respectively. Zhenyi et al. in 1994 discovered the interesting electromechanical performance of PU thin film, when they were searching for a material with both good piezoelectric behavior and low modulus [58]. Three years later, Su, et al. [60] reported details on the electromechanical response of PU film as a function of electric field, film thickness, frequency and temperature, demonstrating about 0.8% actuation strain, and charge injection phenomenon in thin PU films. Later, Arora, et al [61] compared the electromechanical response of prestretched PU and silicone tubes, and reported smaller actuation strain of PU, but significantly higher blocking force. They also reported smaller axial (prestretch direction)

actuation strain and larger radial actuation strain as a result of mechanical conditioning of the tubes through repeated strain-cycling.

Table 2-1 lists some important material properties as well as actuation properties of commonly studied DE materials. The properties of DE materials reported in Table 2.1 should be used for comparative purpose only. The values are sensitive to the composition of the materials, applied prestretch, and actuation setup. It is important to note that DEs are commonly prestrained not only to reduce their thickness and thereby the necessary electric potential, but to enhance their actuation strain, dielectric strength [49], dielectric constant [49], as well as to reduce the electromechanical instability (EMI) [56].

**Table 2-1. Important properties of three typical dielectric materials.**

DE material	Mechanical property		Electric properties		Electromechanical properties	
	Young's modulus (MPa)	Energy density (J/cm <sup>3</sup> )	Dielectric constant (at 1kHz)	Dielectric strength (MV/m)	Actuation stress (MPa)	Actuation strain (% area strain)
Polyurethane	17[46]	0.087[46]	7[46]	80 [8]	1.6[46]	11[46]
Polyacrylate (VHB)	0.3	3.4[45]	4.7-6[54]	412[45]	7[45] [7]	158[45]
Silicone (Dow Corning HS3)	0.125[46]	0.026[46]	2.8[46]	110[45]	0.3[45]	93[45]
Block copolymer (SEBS217) [62]	0.133	0.289	-	22	-	245

\*Note that mechanical and electrical properties are sensitive to preparation of the materials, prestretch and measurement setup, and thus the values in the chart cannot be simply applied to a certain type DE material.

Despite all the progress made in improving the electromechanical performance of the DE materials, one of the critical issues impeding widespread adoption of these materials in

practical devices is the requirement of high electric potential. In order to generate useful levels of actuation strain, operating electric field for DE films ranges from 50V/ $\mu\text{m}$  to more than 100V/ $\mu\text{m}$ , typically requiring applied voltage of 5-10 kV [48]. The required potential can be reduced by reducing the material thickness (see Equation 2.1), and by increasing its dielectric constant.

As is mentioned earlier, prestraining the DE film is one of the methods to enhance the electromechanical performance, mainly due to the thickness reduction [49]. However, increasing prestrain comes with the requirement of additional overhead and problems of stress dissipation over time. Ha [53] proposed a potential solution by creating an interpenetrating network (IPN) in the DE film. In this method, a secondary polymer network is created in the prestretched acrylic elastomer by adding a crosslinking agent (1,6-hexanediol diacrylate). The secondary polymer network withholds the prestretch at the expense of higher DE stiffness that limits the actuation strain.

Potential solutions to eliminating prestretch also include fabricating ultrathin DE films [63], lowering the stiffness of the DE material [15], [51], [52], and increasing the dielectric constant of the DE materials [64]–[66]. For example, Duduta [63] fabricated ultrathin (25 $\mu\text{m}$  to 30 $\mu\text{m}$  thickness) DE films from UV-curable acrylic oligomers, with operating voltage around 1-2 kV. The crosslinking agent used for creating IPN for by Ha et al [53] is here to the acrylic to tune the adhesiveness and actuation performance of DE film. Higher crosslink content increases the Young's modulus of the material, and the resulting smaller viscoelastic effect improves the electrical actuation bandwidth (or frequency) albeit with lower deformation. Similarly, Zhao [52] altered the elastic modulus of DE film by adjusting the content of two thermal curable

acrylate monomers, one serving as soft segment while the other as crosslinking agent with reactive functional groups.

Efforts to improve the dielectric constant of DE materials include adding sub-percolation levels of conducting “fillers” in the DE matrix [65], [67], [68]. In order to reduce the current leakage the conducting fillers have also been encapsulated with insulating materials [69], or by adding fillers in the middle DE layer that is sandwiched between two dielectric layers [66]. In this manner, both dielectric property and breakdown field can be enhanced.

Another efficient method to enhance and employ the electrically induced strain is to produce directional deformation through anisotropic actuation. The anisotropic actuation strain has been reported in asymmetrically prestretched DE tubes [61], and by using aligned CNT electrodes [70], and by directionally embedding reinforcing elements (fiber, etc.) [6], [71], and selectively corrugating DE film [72]. Anisotropic actuation would be described further in Section 2.1.2.

Last but not least, to inhibit EMI and associated dielectric breakdown, in addition to prestraining the film as described earlier, electrode-free actuation via corona discharge from needle electrodes has also been explored [73].

## **2.1.2 Dielectric Elastomer Actuators**

Dielectric elastomer actuators (DEA) are promising for many applications including human assistive devices [10] and soft robotics due to their flexibility, low weight, large actuation strain, and high energy density [6], [8], [47]. In addition to the ongoing research to improve the performance of the DE materials, efforts are underway to design DE-based

actuators (DEA) and devices to harness the material's potential. The primary goal in designing a DEA is to maximize some of the important performance parameters, such as, energy output, power output, energy conversion efficiency, response time, displacement, force, velocity, stiffness, damping, accuracy, repeatability, sensitivity, environmental tolerance, durability, reliability and input impedance [34]. Depending on the intended application some of the parameters may be more important than others. Although DEs stand out due to its many desirable properties, there are some ongoing issues:

1. Need of high electric field.
2. Accuracy and durability is limited by the viscoelastic damping of the material.
3. Frequency response is restricted by the charge and discharge speed of the material, as well as their mechanical properties. If the frequency of alternative current (AC) is too high, the actuation electric field would decrease due to the insufficient charge and discharge. Besides, if the material has high viscoelasticity, the induced deformation and recovery speeds restrict the actuation frequency.
4. Need to maintain electric potential to maintain strain, leading to dielectric breakdown.
5. Researchers have made great strides to address these deficiencies, by material enhancement and actuator structural design. The following discussion focuses on structure design of DEA. The designs proposed in the literature is divided into three categories based on their mode of actuation; linear, bending and rotational. The discussion also includes their potential applications.

## Linear DEA

These actuators are designed to transform the areal expansion of DEs into linear motion. Three examples of this kind are shown in Figure 2-3.

A DE-based fiber actuator that can be potentially manufactured using bicomponent fiber manufacturing was proposed by Arora et al. The prototype fiber actuators were fabricated by using a DE tube made of silicone with inner and outer surfaces coated with compliant electrodes. Upon application of an electric field the actuator expanded radially and axially. It was found that longitudinal prestretch reduces the axial actuation strain, and thus enhances the longitudinal elongation [61] (Figure 2-3a).

The longitudinal force output of the tubular DEA was sufficient to use for refreshable braille displays, see Figure 2-3b. The compact, light-weight and highly deformable DE tube made with silicone is capable of moving the braille upward and downward, and thus creating patterns for the tactile sensation [74].

A bistable truss and two DEAs were assembled to make a linear binary actuator for robotic applications by attaching the DE films on a diamond-shaped rigid frame [75]. The linear actuation results from two DEAs work in an antagonistic way. The area expansion of the top DE generates an actuation force to snap the bistable truss, and the bottom DEA under dielectric actuation can snap the bistable truss upward, see Figure 2-3c. Multi-layered DEA is used to enhance the force output [75].

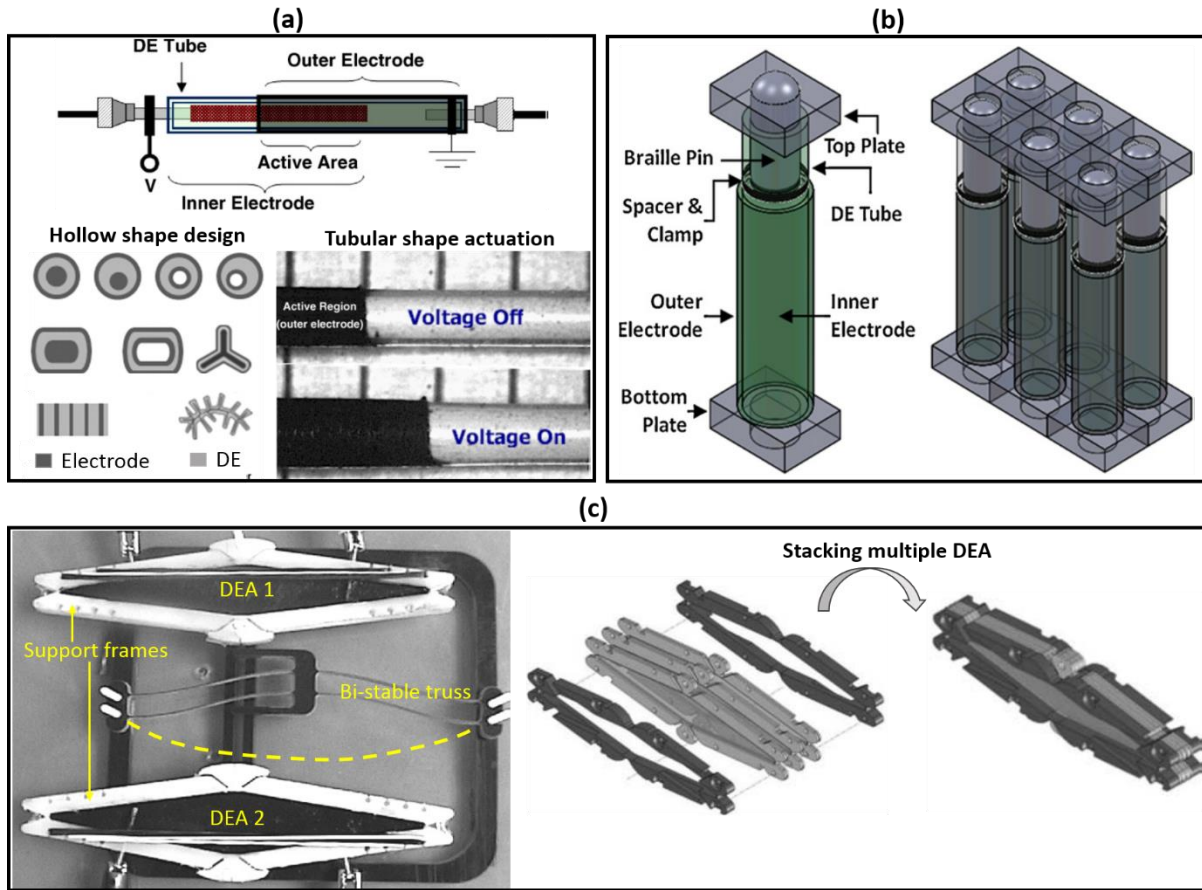


Figure 2-3. Examples of linear DEA [61], [74], [75].

### Bending DEA

Bending motion is commonly achieved by stacking active elements of DE and inactive elements, as shown in Figure 2-4. The actuation of active DE generates bending moment for the laminate, while the inactive element serves as neutral plane/axis. Unidirectional bending motions are exemplified in Figure 2-4a, b, c, and multi-directional bending is shown in Figure 2-4d. Enhanced bending behavior is achieved by introducing anisotropic mechanical response with stiff fiber reinforcement, shown in Figure 2-4c.

A series of figures in Figure 2-4a present the bending behavior of laminated DEA, as well as electrodes array design for 4 individual active regions. The DEA is composed of 12 layers ultra-thin acrylic elastomer (20-30 $\mu$ m for each), with a pair of compliant electrodes on each DE layer, and a thin stiff polymeric sheet as support layer. Due to area expansion of DE layers and inactive stiff plastic layer, a bending moment is created in the laminate that produces out-of-plane deformation. The 4 individual active regions are composed of 4 pairs of electrodes, and the dielectric actuation of different active regions produces multiple actuation patterns. The profound deflection at relatively low actuation voltage (1-2kV) is achieved by using ultrathin DE films. Moreover, this paper compares three UV-curable acrylic elastomers in terms of their adhesiveness to electrode material (CNT), crosslink content, mechanical strength and actuation behavior, which gives valuable guide to the acrylic DEA exploration [63].

In Figure 2-4b, the electromechanical performance of DE is used to unbend a gripper structure. The closure of gripper's legs helps grab object. Instead of triggering the closure of the gripper legs, this novel DEA gripper is stable in the closure status, meaning the electrical energy is utilized to unbend the gripper. Once grabbing the object, the electrical voltage can be removed. The tulip-shaped structure of the DEA gripper is formed after the strain energy minimization of the elastic-rigid laminates. By prestretching the DE film, and attaching plastic strips at certain locations on the prestretched DE, the contraction of DE upon removal of external load results in strain redistribution, and thus leads to the self-organized shape. In this paper, DE not only serves as an energy storing medium, but also works as an electromechanically active element to morph the structure. By applying two compliant electrodes on the DE film and external voltage, the expansion of DE film flattens the structure.

The output force (blocking force) is measured to be about 7mN (at 2kV). The self-organized shape and electrical unbending force is being explored in this paper as a soft gripper [50].

Similar laminated structure is also presented in Figure 2-4c, with tunable bending direction assisted by different orientation of aligned fibers. The output force is utilized to grab objects with various shapes. In the laminates composed of DE film and inactive stiff elastic film, the voltage-induced in-plane stress of DE produces bending moment of the laminates that results in the out-of-plane deformation. The out-of-plane actuation is oriented to a certain direction with reinforced fiber directionally embedded in DE matrix. As a result, the fiber reinforced elastic-plastic laminates have tunable bending patterns under electric field [76].

A multiple degree-of-freedom (DOF) rolled (sometime referred to as spring roll also) DEA was designed with selective actuation of discretely distributed active DE regions. In this structure, the antagonistic actuation force selectively bends the structure in different direction. The schematic shown in Figure 2-4d describes the electrode patterning on a flat DE film, and the stacking of active part by rolling up the film. DE film is rolled around a compressed spring. After release of the compressive force on the spring, the DE film is stretched longitudinally. For every layer of the rolled tubular DEA, there are four pairs of electrodes, corresponding to four DOF. Linear motion can also be generated by simultaneous actuation of the four pairs of electrodes. And the multiple layers of active area plying together increase the force output. Moreover, multiple DOF is achieved by connecting rolled DEA units in sequence, which is promising in providing multiple motions [47]. In the following context, the multiple DOF with electrode patterning strategy is exploited as rotational DEA with various applications including artificial eyeball motion [77], soft motor [78] and biomimetic walking robot [79].

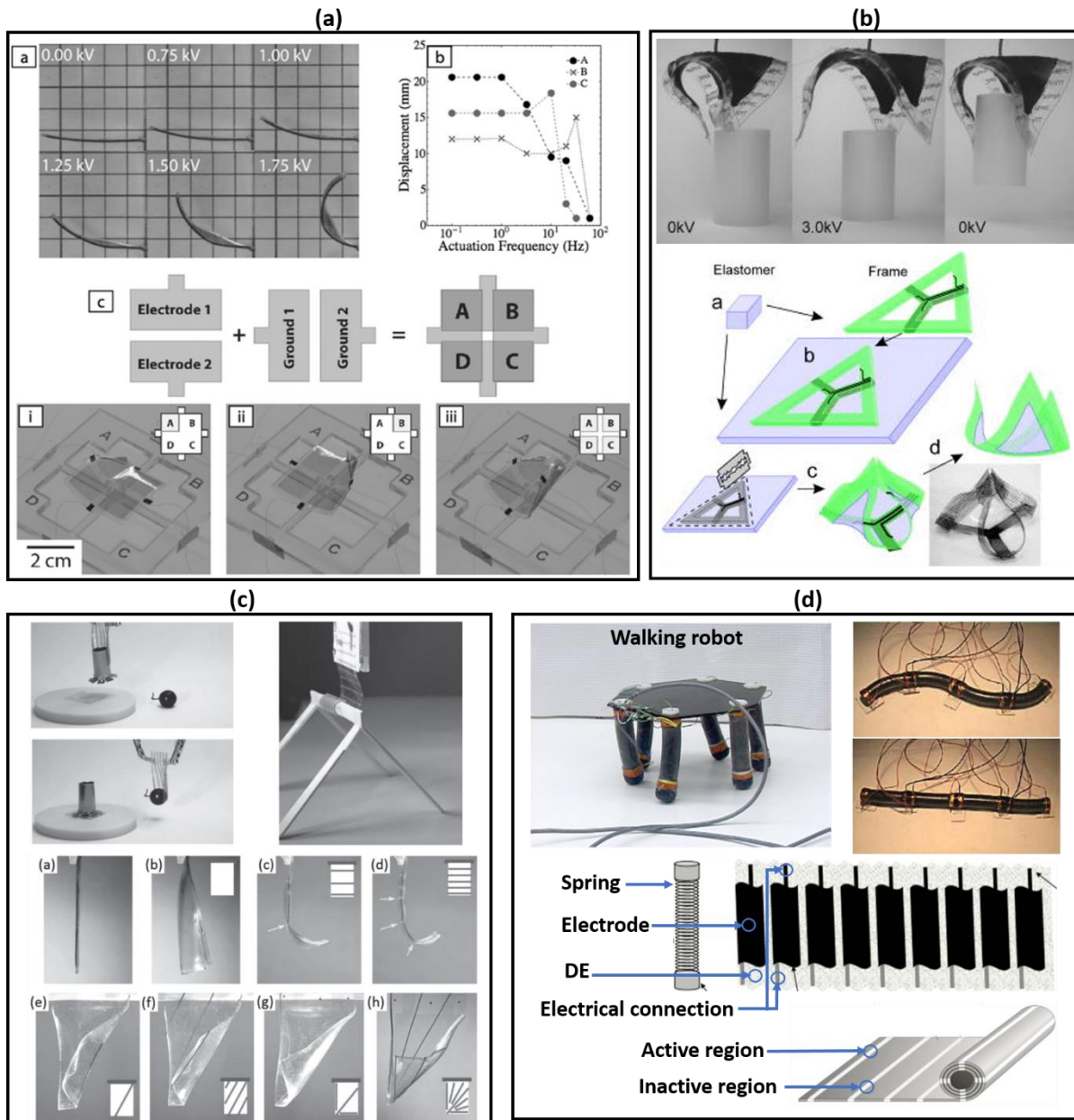


Figure 2-4. Examples of bending DEA [47], [50], [63], [76].

## Rotational DEA

To mimic the rotational motion of human eyes, two-degree-of freedom (2-DOF) DEA is utilized as the ocular muscle that controls eye motion (Figure 2-5a). The 2-DOF DEA is composed of two prestretched DEA units, each frame is symmetrically flexible in folding. Specifically, VHB 4910 is prestretched and attached to one symmetrically foldable frame with a circular hole in the middle and coated with a pair of electrodes, serving as one DEA unit. Two units combined with half of each frame glued together, and the other half fixed in-plane on a planar support. Thus, the 2-DOF DEA is fabricated with rotatable mid-arc about its symmetric axis, controlled by actuation of two DE films. By inflating the system with pressured air chamber beneath, the DEA achieves higher actuation strain (represented in this system as rotate angle) with input voltage around 3.5-4kV [77].

Two examples of 6-DOF DEAs shown in Figure 2-5b works as a bearing-free motor. The prestretched DE film (VHB 4905) is adhered to a large rigid ring support on the outside and a small ring (gear) on the inside, and discretely coated with 6 pairs of compliant electrode. A shaft fixed into the inner ring with minimum friction, can be rotated, tilted or laterally repositioned by applying electric field to different combination of electrodes [78].

A DE-based walking device with 6 legs was designed as a biomimetic walker. Each leg was designed to move upward and downward (linear motion), as well as forward and backward (bending and rotational motion), owing to the three DOF generated by antagonistic actuation of 4 separate DE actuators, shown in Figure 2-5c. The DE material is composed of two silicone compounds with optimized mixture ratio for electrical and mechanical performance. After casting the silicone film, it was prestrained and glued to an annular frame. One film acts as two

DEAs in the antagonistic actuation design by applying separated electrodes on the film. By combining two annular frame-supported DE film together with a stiff bar separating the DE films to a distance, the three-degree-of-freedom DEA came into shape [79].

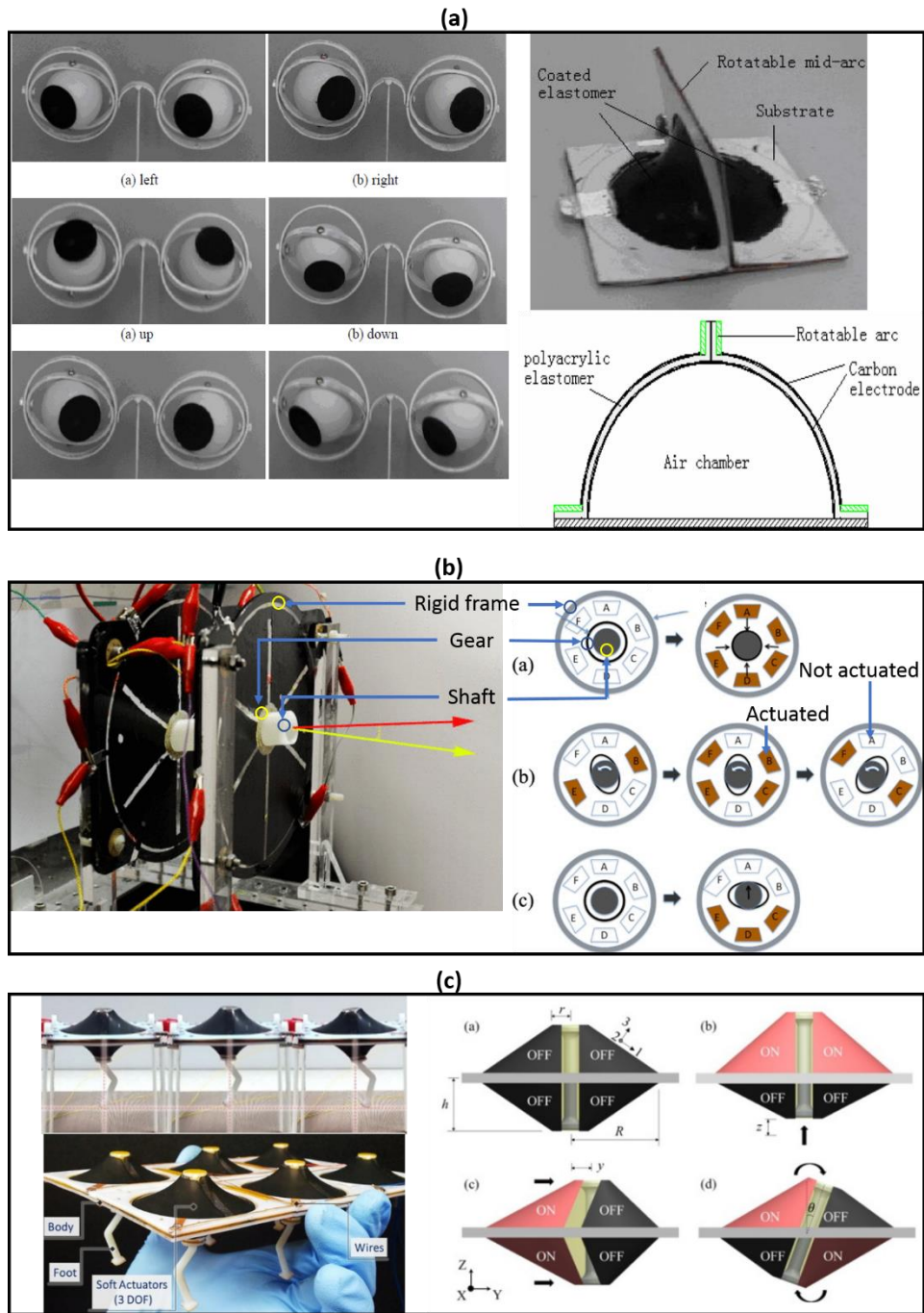


Figure 2-5. Examples of rotational DEA [77]–[79].

With various structural design shown in Figure 2-3, Figure 2-4, and Figure 2-5, the areal expansion of DEA can be transformed into linear, bending and rotational motions.

Considerations are given to actuation force/displacement improvement, reducing actuation voltage, actuation speed enhancement and structural robustness design. Some of the solutions presented in the DEA examples, can be summarized as following:

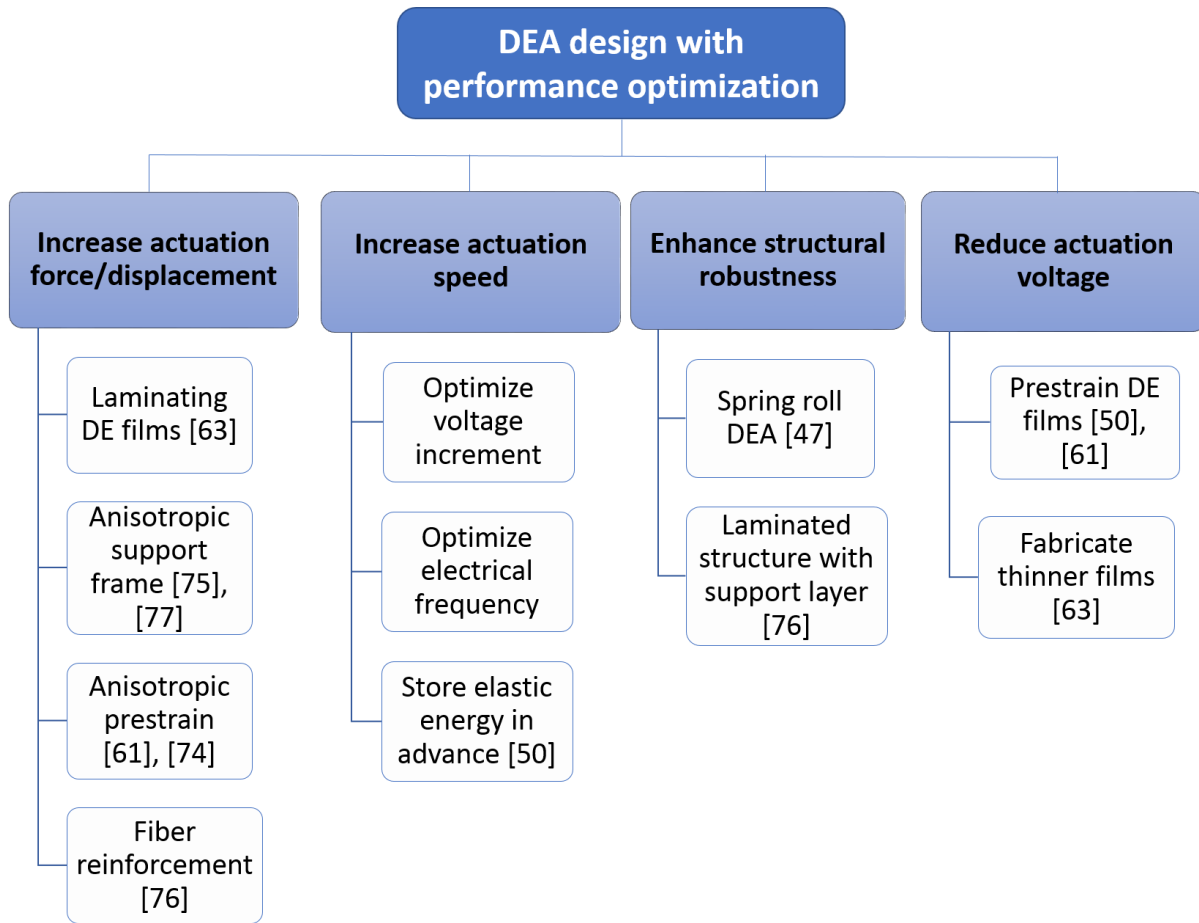


Figure 2-6. Summary of the methods to enhance the actuation performance via DEA design.

## 2.2 Morphing Multistable Structures

Morphing or shape transformation can be a very important and useful performance attributes in many applications. Morphing in nature help plants and animals adapt and function under many environmental conditions [1]-[3]. Biomimetic shape-changing systems have been an active area of research for a long time. Among different morphing structures, morphing multistable structures (denoted as morphing MS) are mechanically robust and deform fast between several stable shapes. A morphing MS has more than one structural stable configurations and undergoes mechanical instability between stable states. Shape transformation from one stable state to another is called “snap-through” [107]. From energy point of view, each stable state has an energy valley where the structure can stabilize without external energy supply, and is able to sustain environmental turbulence to some extent. During morphing, the mechanical instability configurations have high energy stored in the structure, which tend to release the energy and shift to stable configurations. Figure 2-7 shows the energy diagrams of bistable structures. Bistable structure is one type of morphing MSs with two stable states. Symmetric bistable and asymmetric bistable are defined according to the energy status of two stable states. For symmetric bistable structure, the activation energy amount is the same for snap forth and back, while for the asymmetric bistable structure the activation energy levels are different.

The advantages of morphing MSs for shape transformation are as follows:

1. Mechanically robust in the deformed state (Note that the deformed state is one of the stable shapes).
2. Pre-programmable shape deformation.

3. Large shape transformation without high energy cost.
4. Tunable power output (or morphing speed) by modulating multistable characteristics (elastic energy storage, multistable shape).

The morphing MSs can be classified by the stimulus (activation energy) used for snapping. Passive morphing MSs use environmental change (air flow, etc) to activate the snap-through of the structure, and is utilized in aerospace [23], vibration energy harvesting [26], and turbine shape adaptation for wind energy [27]. In particular, bistable shapes have been utilized to design morphing aerofoils for optimized flight conditions as well as for wind turbine blades which can withstand higher wind speeds without fracture [27]. However, active morphing MSs are realized by application variety of stimulus. By employing smart materials such as shape memory alloys (SMAs) [80], or piezoelectric materials [81], the linear shape change of these smart materials provides activation moment to snap the MSs. The active deployment of MSs has potential application in actuators that transform energy input into mechanical motion.

The following section gives insight into the morphing principles and varieties displayed by natural world and found in manmade engineering work.

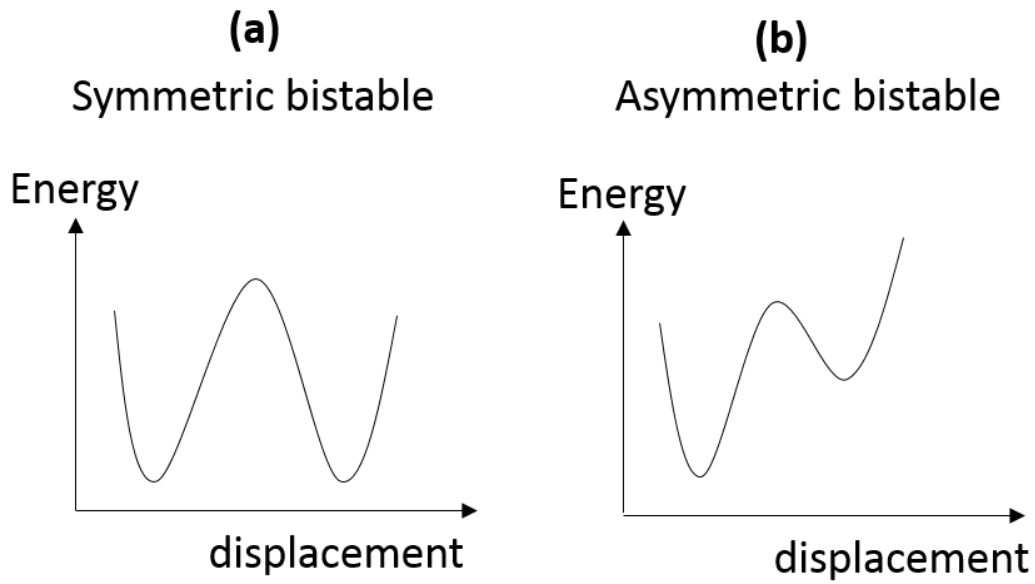


**Figure 2-7. Energy diagrams of bistable structures.**

### **2.2.1 Morphing Structures in Nature**

Many marvelous morphing of shape transformations, including movements in plants and animals are achieved by sensing and actuation behavior of different organs, and there are great review papers describing these phenomena and mechanisms of natural motion [82], [83]. In biological systems, the actuation elements such as motor cells in plants, or muscle cells in animals, are responsible for the morphing behavior of the related organs. In order to generate the movements with greatest efficiency and precision, they perform under stringent principle of signal acquisition, analysis, transduction and output. In this chapter, we only take a brief look at the signal output, and more specifically the macroscopic morphing behavior of plants and animals.

The shape change of plants can be generally divided into two categories, active and passive. Active shape adaption involves active sensing and transformation, metabolic energy

consumption, active potential transportation, change of water/ion permeability in cell membranes, and turgidity of the whole organ for load bearing [84]. Among the active motion in plants, thigmonasty and thigmotropism refer to rapid response of certain specialized organ of plants to external mechanical stimuli (touch) [85]. For example, rapid coiling of tendril of peas within minutes after sensing the touch is due to the differential cell growth induced by osmotic pressure change [86]. The coiling direction is affected by the location of touch, a phenomenon known as thigmotropism [85]. However, the fast closure of Venus Flytrap (VFT) upon mechanical stimulation is not affected by the direction of the stimulus, and thus called nastic response or thigmonasty. The VFT exploits a unique power amplification system that is responsible for the fast leaf closure. Further explanation of closure mechanism of VFT is presented later. Passive shape adaptation includes the environmental humidity change induced passive swelling or shrinkage of dead organs. Opening of pine cone and chiral seed pod are two common examples of passive shape change. After the plants become mature, the scales of pine cone (valves of seed pod) open to spread seeds inside the valves, while the environmental humidity decreases. The bending or twisting of corresponding tissues induced by anisotropic shrinkage are responsible for the opening motions of these plants [87], [88]. Figure 2-8 and following context explained three interesting morphing examples in botanical world.

Venus Flytrap in the botanical kingdom possesses highest leaf closure speed (within 0.1s). Its trigger hairs on the inner surface (red side in Figure 2-7b) of the shell-shaped valve is able to sense mechanical force, which generates action potential. Then the biochemical action potential is transported to motor cells in the leaf that is responsive to the morphology change. Motor cells change the osmotic pressure by actively changing the water permeability in the cell

membrane. For example, the active water influx increases the osmotic pressure that leads to the expansion of cells and enlargement of tissue. The osmotic pressure change drives the shape deformation, but is not the key factor of fast closure of the valves. The fast closure speed is due to the bistable shell structure of the valve. Upon activation of motor cells, the mechanical instability between two stable states facilitates the rapid deformation of the valve. The bistable valve bending structure, in molecular scale, is generated by differential cell elongation and cell wall reinforcement in the inner surface and outer surface, and the resultant anisotropic mechanical strength lead to differential strain (Figure 2-8b) of the valve in two perpendicular directions during cell expansion. The cells in the outer surface are highly elongated and reinforced by microfibrils in x direction, and the strain energy stored speed up the inward bending of the valves [1].

Another example of bistable morphing is the opening of pine cone. When the pine cone is mature, the scales grow into well-distinguished two-layered manner with inner and outer layer composed of two types of tissues, sclerenchyma fibrils and sclerids, respectively (Figure 2-8c). Perpendicular orientation of cellulose fibers on two types of cells and resultant differential hygroscopic expansion is a crucial factor for the development of bistable configuration and bending movement. When environmental humidity decreases, the scales undergo differential shrinkage due to the different coefficients of hygroscopic expansion of two layers, and thus lead to the bending behavior [87]. Experiments were carried out to demonstrate the reverse motion of the pine cone scale by increase the moisture. The opening of chiral seed pod is similar to that of pine cone, while their mature morphing organs are both dead, and thus belongs to the passive shape morphing.

Similar to the bending of the scale of pine cone, the two valves of chiral seed pod (Figure 2-8a) are composed of two layers differentiated by the orientation of cellular fibrils which is main component of the cell wall. The cellular fibrils on two layers oriented perpendicular to each other, and  $\pm 45^\circ$  to the longitudinal direction of the seed pod, resulting in the helix development along longitudinal direction when humidity decreases [88]. Armon et al designed the synthetic analog of this twisting structure by perpendicularly prestressing and laminating two elastic films, and cutting strips out of the laminate at a specific angle. The elastic energy balance lead to twisting shape (Figure 2-8a).

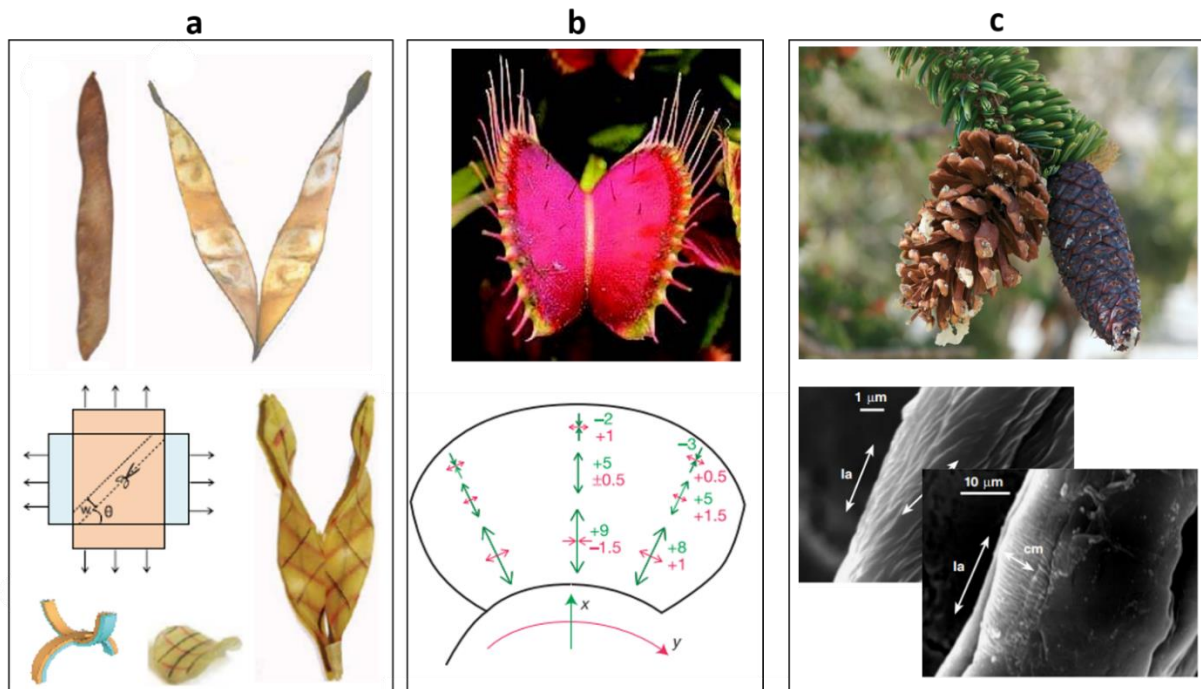


**Figure 2-8. Bistable morphing structures of plants [1], [87], [88].**

Daily movements of animals are much more complicated than the movements in plants. Movements in animals are enabled by the collaboration of muscle contraction and relaxation,

energy storage and release in tendon and rotation of joints. Researchers found that the whole body acts as a continuum to balance the mechanical force such as self-weight, in order to stabilizing the shape and reducing physical impact. Due to the seamless connection between the internal cytoskeleton of cells and extracellular matrix (ECM) by integrin, and connections among multiple types of filaments (actin-microfilaments, microtubules, intermediate filaments) for integrity of cells, the tissues and organs composed of cells and ECMs share the tension and compression. From molecular and cellular scale to the body scale, the mechanical force balance is maintained by the so called structural tensegrity (tension integrity). The opposing tension and compression elements (cytoskeleton filaments) generate internal tension (prestress) which help maintain the equilibrium of mechanical force and thus stabilize the shape [84].

Muscle as a natural actuator controls the movement by contraction and extension. The actuation signal is transported in nerve cells by releasing of  $\text{Ca}^{2+}$  ions [82]. The output mechanical energy can be directly or indirectly transformed from metabolic energy to the sensing, transportation and actuation processes. In particular, fast actuation in animals is commonly achieved by prestretching muscles or other elastic elements in advance. During movements, the elastic energy stored in the muscle or elastic tissues is rapidly released to generate fast mechanical response (high power output).

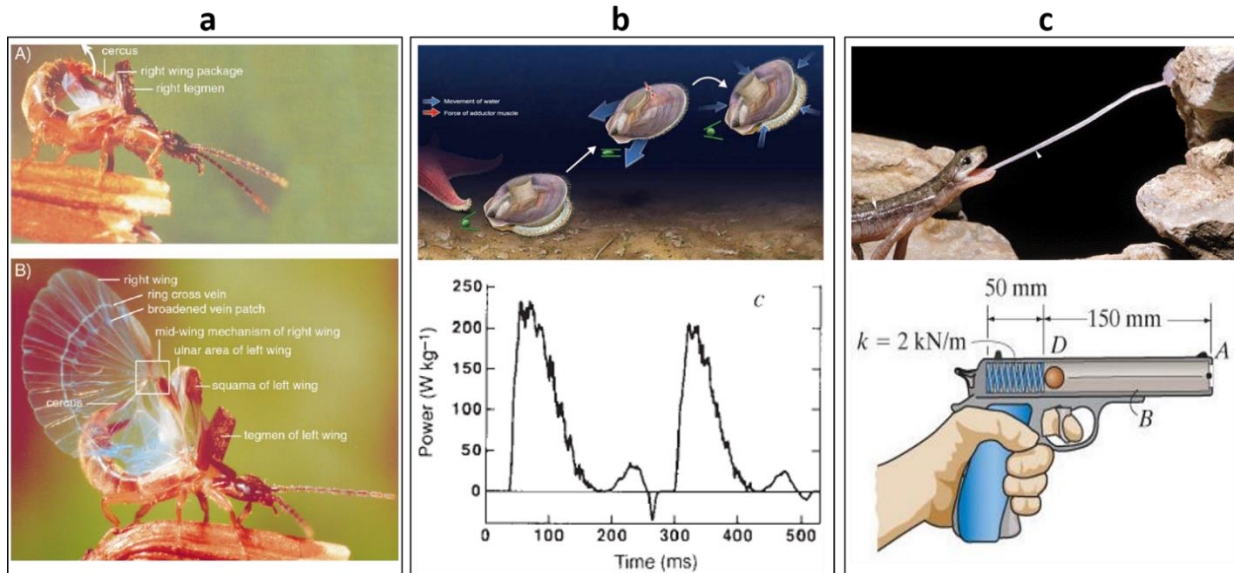


**Figure 2-9. Morphing behaviors of animals [3], [89], [90].**

Dermaptera (Figure 2-9a) is one type of the insects whose wing folding pattern is amazingly textured, while the fully extended wing area is 10 times larger than the folded shape. The continuous wing deployment and adaptation is facilitated by controlling the resilin (a protein with high elasticity) in the elastic vein joint [89].

The jet-propelled locomotion of scallop is due to the bivalve structure connected by an adductor muscle near the hinge (Figure 2-8b). The active contraction and relaxation of rubbery adductor muscle cause the closure and opening of the two valves. It moves forward when the muscle contract and eject water out of the ventral portion. In vivo mechanical performance of scallop during jet-propelled swimming were analyzed by the aquatic pressure and flow rate. The measured power output can be up to 225W/kg [82].

The fast movement by rapid elastic energy release is performed such as ballistic tongue projection in chameleon [91]–[93], take-off of quail (*Coturnix chinensis*) [94], jet propulsion

swimming of the scallop [90], etc. has been examined with great interest. Salamander (Hydromantes) for instance, achieves high performance of ballistic tongue projection by contracting protractor muscle in advance (Figure 2-9c). The release of strain energy in the protractor muscles generates the mechanical energy which projects the whole protractor muscle outside its body, just like a bullet being projected out by the spring [3] (Figure 2-9c). Chameleons make use of the same principle of strain energy storage and release for fast tongue projection. The power output (mean body-mass-specific power) in chameleon's tongue projection process can be up to 3185 W/kg [93], much overwhelming when compared to that of bird hovering around 80W/kg [94], or to that of a young man jumping which is about 60 W/kg [95]. In order to capture the prey in a fast and effective way, the tongue movement is not only extreme in speed, but also possesses great adhesive force and comprehensive adhesivity on the tip of tongue. The projection force in a horned frog tongue was measured of up to 1000 mN when it touched a glass slide, and the pulling force can be higher than 1500 mN [96].

### **2.2.2 Manmade Morphing Structures**

Compared to the smart, light weight, flexible and mostly polymer-based natural actuation systems, conventional man-made actuators including electromagnetic motor and combustion engine are limited in terms of power supply, bulk, and low energy efficiency [48]. Inspired by the understanding of biological actuation system and limitation of conventional actuators, a variety of biomimetic shape morphing soft actuators with potential application in aerospace [22], [23], biomedicine [9] and robotics [97], have been designed and developed. Stimuli-responsive material-based soft morphing strategies including solvent swelling [17], [98],

thermal expansion/contraction [99], [100], hydration/dehydration [99], [101], photo-induced isomerization [102], [103], electrical actuation [12], [29], [79], etc. have been evaluated.

Structural designs relevant to morphing developed together with material advancement, including anisotropic structure [17], morphing MSs [19], [24], [80], hierarchical structure [104], antagonistic systems [77], etc. Taking anisotropic structures for example, anisotropic mechanical strength and hydrophilicity can be generated using various approaches, enabling the actuator to morph along certain directions. For example, polymer composites possessing mechanical anisotropy is one of the biomimetic solutions. Inspired by the differential mechanical properties in plant cell wall or organs, which are commonly generated by directional fiber reinforcement, artificial polymer composites fabricated through additive manufacturing have been investigated. For example, 4D printing [17] is able to print smart materials by embedding structural reinforcing elements (fibrils [17], crystals [102], [105], composite tubes [23]) into isotropic matrix as well as control over the alignment. The resulting composites possess anisotropic strength or hydrophilicity, due to the different properties of elements. Anisotropy can also be obtained by other means, including chemical and physical modification on isotropic materials [17], [102], [105], hierarchical structure design [15], [104], anisotropic stretch [22], etc. The resulting anisotropic materials can change shape along preferential directions under a given stimulus.

To illustrate the anisotropic deformation, three examples in Figure 2-10 present bending motions activated by light, heat and water. While in Figure 2-10a and c, the anisotropic properties (thermal expansion, hydrophilicity, mechanical strength) are generated in different

layers, Figure 2-10b exploits directional applied stimuli to produce anisotropic deformation of a homogeneous active matrix.

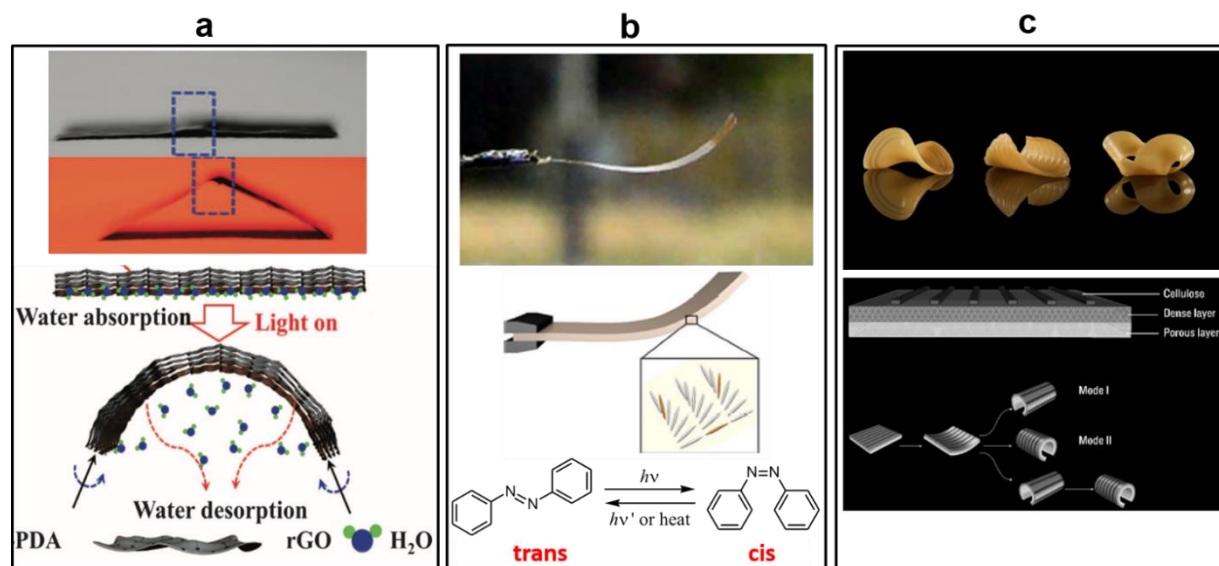


**Figure 2-10. Bending behavior of synthetic morphing structure [102] [105] [108].**

In Figure 2-10a, a light-induced bending of a strip is created as a self-walking device using photoresponsive bilayered graphene paper composed of graphene oxide (GO) and reduced graphene oxide (rGO). The bending is induced by light due to the excellent photothermal property of graphene. The thermal expansion of rGO layer and water desorption of GO layer help develop the bending moment on the bilayered thin film [99].

Photoisomerization, the molecular behavior in which structural change of isomers (cis and trans) activated by different wavelengths of light, induces macroscopic shape change that takes place in certain liquid crystalline polymer (azobenzene). Kumar et al found that fluorinated azobenzene doped nematic liquid crystal film can keep oscillating bending while being exposed alternatively to green ( $\lambda=530\text{nm}$ ) and blue light ( $\lambda=405\text{nm}$ ). Further analytical

experiment demonstrated that the green light activates trans-cis isomerization, and blue light activates cis-trans isomerization. Increasing in trans isomers causes bending of the film [102].

Morphing can be induced by anisotropic swelling of polymer composites under isotropic stimulus (water). MIT Media Lab developed a transformable food in “flat packaging” convenient for shipping. The designed product is flat in the shipping process, and change shape after being immersed in water, which reduces the shipping cost. In the experiment, the researchers made use of different hydrophilicity and stiffness of ethyl cellulose (low water absorption) and gelatin (higher water absorption), and developed a three-layered structure which can bend directionally during hydration. Gelatin film serves as the matrix with density gradient during film casting, with higher density on the top and porous structure in the bottom of the film. This difference in density in gelatin film causes differential water absorption in both rate and capacity, leading to the upward and downward bending behavior. Additionally, the directionally aligned ethyl cellulose fibers on the top of the gelatin matrix affects the bending direction due to the higher stiffness of cellulose fibers, and also impacts the water absorption of top surface of gelatin matrix [106].

Another promising strategy of structural design is morphing MSs that stand out for large displacement, fast morphing speed, shape stability and energy conservation. There are several methods to create morphing MSs (Table 2-2), and a variety of stimuli can be applied to activate the shape transformation.

**Table 2-2. List of multistable structure categories, mechanisms and examples.**

Multistable structures	Causes	Examples
Laminated sheet	Residual thermal stress	Asymmetric laminating of carbon fiber reinforced prepreg [107]
	Residual elastic energy	Prestressed Nylon reinforced polymer matrix [108]
	Induced elastic energy	Globally [109], [110] or selectively [111] prestressed lamina
Buckled tensegrity structure	Boundary constraints (strained when balanced)	Thin shell with compressive in-plane force around the boundary [19], [112]
	Boundary constraints (unstrained when balanced)	Cured 3D pleated structure [113]; Von Mises Truss with elastic joints [104]

Figure 2-11 shows 4 examples of morphing MSs, representing the two general categories of morphing MSs design including film laminating, and buckling with constraint boundaries.

Figure 2-11a represents an explorative research in both material and structure inspired by the VFT. The bistable shell structure with responsive surface was created and triggered via multiple stimuli. The plate buckling and confined boundary contributed to the development of bistable configurations as well as stress-induced shape transition. For the bistable shape design, a silicone substrate with numerous holes and another thin silicone film attached to the holes were used. By inflating the substrate and casting a thin silicone film seamlessly on the holes of the substrate, followed by deflation, a compressive in-plane stress around the border of silicone film is developed. The in-plane stress buckles the 2D film and produces 3D bistable domes, with either convex or concave shapes. The bistable shape transformation is induced by differential

volume change on top and bottom of the thin silicone film. By introducing oxygen plasma into the shell outer surface, the chemical reaction induces volumetric decrease which causes convex-concave transition, while the solvent induced increase of osmotic pressure on the outer shell surface gave rise to the concave-convex transition [19].

In Figure 2-11c, a novel design of deployable skin inspired by the pleated wing of *Demaptera*, is proposed as adaptive camouflage. The bistable structure has simple fabrication steps but complex load bearing capacity (stiffness tailoring) due to the origami texture. It is fabricated by curing silicon into a predefined 3D configuration, reinforced with a piece of paper. The two stable structures are stress free, while during morphing, the stresses are concentrated on the folded lines. The snap-through is activated by applying vertical load to the structure [113].

The von Mises truss is a simple bar structure consisting of two bars connected at the top to each other [104]. Following the shape of Von Mises Truss (VMT), a bistable actuator was created with a defined stroke length and force bearing capacity (Figure 2-11d). It was followed by the design of hierarchical structures based on the bistable unit. The VMT is composed of a pin for linear motion, 4 stiff trusses, 1 bracket for boundary set, and 8 elastic joints connecting the trusses and bracket that are crucial in buckling instability. When the external load is applied to linearly move up the center pin, compressive forces are generated by the elastic joints, which deform the joint to facilitate the buckling. The elastic energy accumulated in the joints reaches to a maximum in the snap-through point, after which the bistable unit rapidly deforms to the other stable state [104].

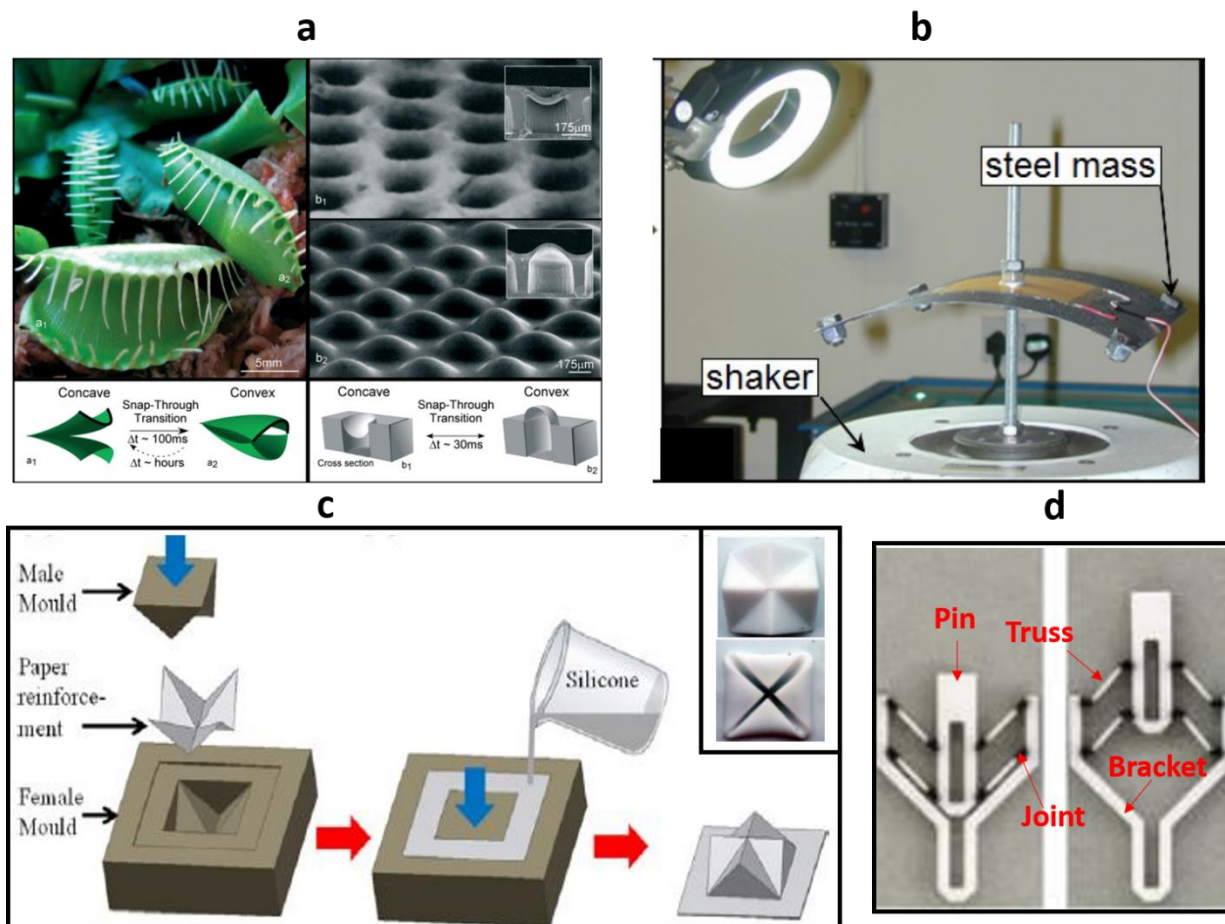


Figure 2-11. Synthetic multistable structures [19], [104], [113].

Among all the methods for designing morphing MSs, plying of fiber-reinforced polymer sheets is the most investigated. Often the analysis of these structures using finite element analysis (FEA) [114], composite sheet (beam) bending theory, as well as the energy approximation theory [107] for bistable shape prediction and blocking force analysis has been reported. Bistable laminated structures have been investigated following Hyer [107], [114], [115] to show that thin unsymmetric laminates cured into cylindrical structures rather than saddle shapes. By embedding directionally aligned carbon fibers into isotropic polymeric matrix (epoxy) at high temperature, anisotropic mechanical strength is obtained within the composite.

By unsymmetrical stacking of anisotropic composite and curing, the initial flat thin prepreg laminates bend into bistable cylindrical shape, due to anisotropic thermal contraction and mismatch of contraction in different layers during cooling down.

More specifically, the low thermal expansion coefficient along fiber direction and high thermal expansion coefficient perpendicular to fiber direction, leads to the anisotropic in-plane expansion. When multiple layers are plied at an angle, the mismatch of in-plane expansion leads to the development of bending or twisting moments along different directions, leading to the multistable configurations. The multistability and magnitude of out-of-plane deformation are influenced by several parameters, such as the stiffness of laminate [116], fiber alignment, ply angle and number of layers [117]. According to these parameters, experiments are performed to study the fiber-reinforced composite MSs.

Figure 2-11b is an application based bistable structures investigation aimed at ambient vibrational energy harvesting. The bistable carbon fiber reinforced polymer (CFRP) is studied together with the adhered macrofiber composite (MFC), in order to convert the vibrational energy to electrical energy. The MFC is a great piezoelectric material which can transform the mechanical energy into electrical energy, or morph under electric activation. The vibration is provided by a shaker, and amplified by attaching four steel cubes [25].

## Chapter 3 Bioinspired Dielectric Bistable Actuator

### Abstract

Dielectric elastomers (DE) are promising actuator materials that feature large actuation strain under applied electric field. In general, they have relatively low elastic modulus and excellent extensibility comparable to natural muscles. DE-based actuators (DEA) are developed to mimic the properties and functionalities of human muscles, with versatile applications in soft robotics [6], [8], human assistive devices [10], etc.

In this work, we describe a novel approach to build a robust multi-layered dielectric bistable actuator (DEBA) that can be actuated under moderate electric field (40-60 V/ $\mu\text{m}$ ). Upon snap-through of the bistable shape, DEBA self-equilibrates to another stable state within seconds and self-stabilizes in the deformed state without the need of continuous voltage supply to maintain the shape. The concept of bistable shape presented here is inspired by the Venus Flytrap that closes its leaves within in 0.1 second upon contact, due to the turgor pressure activated bistable shape transition. We also present another actuator concept inspired by the elastic energy management of the salamander's tongue, the ballistic extrusion of which employs the spring mechanism for high power output. In this research, the DEBA is composed of three structural layers – two prestrained DE layers sandwiching a stiffer polymer layer - for bistable shape construction, and a pair of electrodes forming the electroactive region in one of the DE layers.

We investigated the shape and bistability dependence, the electric field required to trigger the snap-through ( $E_c$ ), as well as the blocking force it can generate. With experimental and theoretical analyses we predicted bistable shape and range, which allow us to optimize the

actuation and performance. The DEBA yields in-plane robustness, low weight (0.3g) and small total thickness of around  $300\mu\text{m}$ , fast morphing speed up to  $150\text{mm/s}$ , and can be electrically actuated at an electric field of  $40\text{-}60\text{V}/\mu\text{m}$ , generating a blocking force of about  $4.5\text{mN}$ .

### 3.1 Introduction

Dielectric elastomers (DE) belong to a class of electroactive polymers (EAP) that undergo large deformation (380% areal strain after prestretch [118]) under an applied electric field. The working principle of DE materials is best explained using a parallel plate capacitor with two compliant electrodes and the DE as the medium. The Maxwell stress (electrostatic stress) produced between the two compliant electrodes deforms the DE and can be harnessed into necessary motion.

After the discovery of DE actuation in 1880 by a German physicist, Rontgen [42], much work is carried out to better understand the principle of DE actuation as well as, enhance its utility and performance. Despite many seminal developments in DE materials and fabrication [37], [119], electrode materials [39], [40] and design [119], significant limitations such as high operating voltage (5-10 kV) and the necessity to apply continuous electric field to maintain deformation leading to dielectric breakdown, restrict the wider application of the DEs. As a result, one of the primary focus of research in DE has been on the improvement of actuation strain at lower voltage. Approaches in this regard, involve judicious prestretching of DE films [49], [56], fabrication of thinner [63] and softer [52], [62] DE films, enhancing dielectric behavior [51], [65], [67].

Bistable structures offer many opportunities to design actuators with low-energy shape transformation and stability in multiple states. Natural examples of bistable structures include bistable leaves of Venus Flytrap [1], chiral seed pod in response to the humidity change [88], saddle-shaped elastic element in the appendage of the Mantis shrimp [121], etc. are excellent designs to adapt in this effort.

Bistable shells can be created by using single film with boundary constraints [19], [112], or by using multiple films laminated with asymmetric elastic stresses [109], [111], [122]. For the latter one, the in-plane stresses deform 2D elements into 3D shapes, such as orthogonal curved disk [112] and helix with opposite handedness [88]. Various external stimuli can be used to trigger the snap-through for transformation of the bistable shape, according to the materials being used as well as the applications. For example, smart materials such as SMA and MFC can be attached to the bistable CFRP to transfer the electrical energy to mechanical snapping of the bistable shape [80], [81], [123].

In this research, we explore a laminated prestrain-induced bistable DEA, similar to the bistable leaves of Venus flytrap and elastic energy management for salamander's tongue extrusion (described in Chapter 2.2.1). In our trilayered structure forming the tape spring actuator, two dielectric elastomer (DE) layers are used both for elastic energy storage and actuation, while a thin polymer film with significantly higher stiffness is placed in the middle for providing a neutral plane for bending. This experiment exhibits a simple way to create an all-polymer bistable structure, and a novel exemplar of DE actuation. Needless to say, the actuator does not require continuous application of potential to maintain either of the two states and therefor is energy efficient.

## 3.2 Experimental

### 3.2.1 Parameter definition

Table 3-1. Parameter definition

<b>W</b>	Width of the tape spring DEBA
<b>L</b>	Length of the tape spring DEBA
<b><math>h_t</math> <math>h_b</math> <math>h_s</math> <math>h</math></b>	Thickness of the (top and bottom DE layers, middle support layer, tape spring laminate)
<b><math>E_s</math> <math>E_a</math></b>	Young's modulus of the (support layer, DE active layer)
<b><math>\epsilon_{xb}</math> <math>\epsilon_{yb}</math> <math>\epsilon_{xt}</math> <math>\epsilon_{yt}</math></b>	Prestrain on the (x- and y-direction on the bottom layer and on the top layer)
<b><math>\sigma_{xb}</math> <math>\sigma_{yb}</math> <math>\sigma_{xt}</math> <math>\sigma_{yt}</math></b>	Stress due to the prestrains of DE layer, obtained from stress-strain curve of DE film
<b><math>P_{xb}</math> <math>P_{yb}</math> <math>P_{xt}</math> <math>P_{yt}</math></b>	Contractile force due to the prestrains of the two DE layer
<b><math>e_t</math> <math>e_b</math></b>	Distances between the mid-planes of the prestrained DE layers and neutral plane of the laminate (support layer)
<b><math>\rho_{xz}</math> <math>C_{xz}</math></b>	Radius and curvature of the shape in state 1 in xz-plane. $\alpha=W/(2\rho_{xz})$
<b><math>\alpha</math></b>	Angle of the bent shape in state 1 in xz-plane
<b><math>S_y</math></b>	Roll-up speed of tape spring DEBA from flat state to state 2, in yz-plane
<b><math>M_x</math></b>	Bending moment of the tape spring DEBA about x-axis, induced by prestrains in y-direction
<b><math>M_y</math></b>	Bending moment of the tape spring DEBA about y-axis, induced by prestrains in x-direction
<b><math>I_y</math></b>	Moment of inertia in yz-plane with respect to y-axis for tape spring DEBA in flat state
<b><math>I_x</math></b>	Moment of inertia in xz-plane with respect to x-axis for tape spring DEBA in state 1

### 3.2.2 Materials

The laminated bistable actuators are fabricated by bonding two orthogonally prestrained acrylate adhesive elastomer films (VHB-4905, 3 M Corp., MN) as dielectric

elastomer (DE) layers to a support layer of either polyimide (PI, Kapton 100HPP-ST, DuPont, DE) or polyester (PET RF025, DUNMORE Aerospace, PA) films of the same thickness (25 $\mu$ m) but different elastic moduli, see Table 3.2. The DE films serving as top and bottom layers, were pre-stretched biaxially using a pantograph-like stretching device. The films were held in stretched state until bonded to the support layer. The stress-strain curve of VHB was measured using a tensile tester and is shown in Figure 3-1. During fabrication, VHB 4905 was pre-stretched biaxially in order to introduce the strain energy, as well as to decrease the film thickness for electrical actuation. Pre-stretch value and anisotropic pre-stretch ratio were crucial in bi-stable structure design and actuation performance.

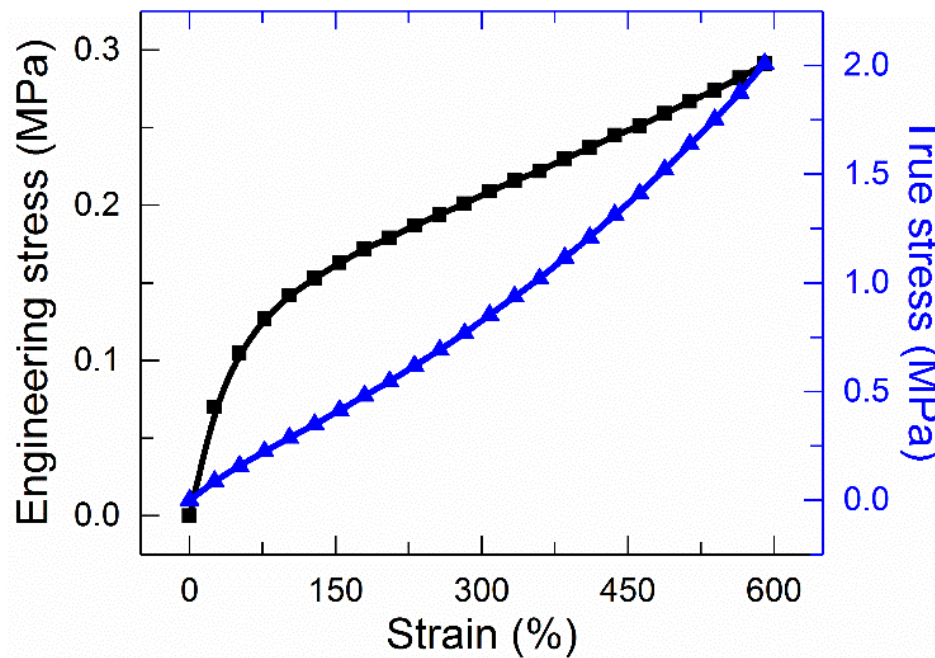


Figure 3-1. Stress-strain curve of VHB 4905.

**Table 3-2. Properties and dimensions of DEBA films.**

<b>Laminates' Components</b>	<b>Material</b>	<b>Thickness (<math>\mu m</math>)</b>	<b>Young's modulus (GPa)</b>	<b>Dielectric constant (at 1kHz)</b>
DE layer	VHB 4905	500	0.00022	3.21
Constraint layer	Polyimide film	25	2.5	3.4
	Polyester film	25	4.9	3.2

\*Young's modulus of DE film was obtained from experiment, and other numbers listed are product information from company website.

Prior to bonding the films together, electrodes were applied to the appropriate positions of the actuators (See Figures 3-3a). We needed to place one pair of electrodes around the bottom DE layer (refer to Figure 3-3a, design to be discussed later); one inside the laminate and the other on the outside. We used two types of electrode materials in fabricating the actuators, carbon grease (Chemtronics Circuit Works, Kennesaw, GA) and PEDOT/PSS, (Orgacon™ EL-P5015, Agfa-Gevaert N.V.) for the inside and outside electrodes, respectively. Adhesion to both DE and the support layer was a key consideration in choosing PEDOT/PSS for the inside electrode. The PEDOT:PSS was screen printed onto support layer using 110 mesh screen and cured in an oven at 130 °C for 3 minutes before use. The easily applicable carbon grease electrodes on the outside of the DE layers were applied using a brush and a mask of polyethylene film. The properties of electrodes were listed in Table 3-3.

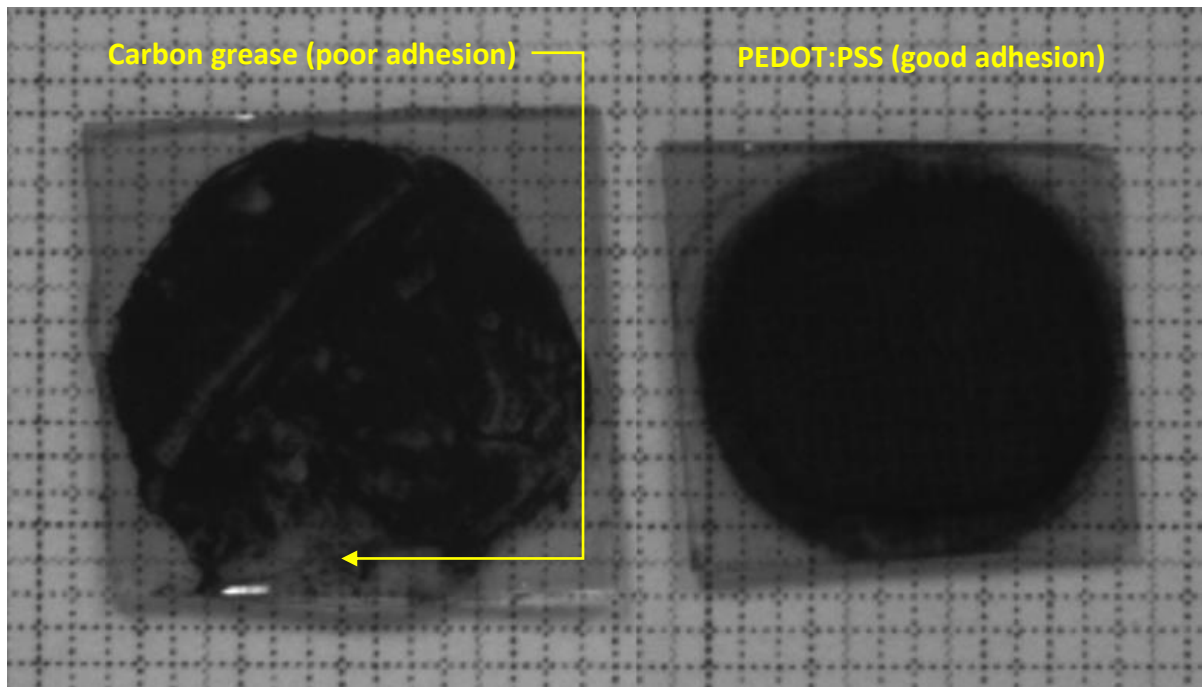


**Figure 3-2. Adhesiveness of the middle electrode (between support layer and bottom DE layer).**

**Table 3-3. Properties of compliant electrodes**

Electrode	Resistivity	Reason of use
Carbon grease [39]	50 $k\Omega/cm$	Good adhesion, inexpensive
PEDOT:PSS [124]	0.0359 $\Omega/cm$	Excellent adhesion, uniform

In order to connect the electrodes to the power supply, soft and flexible electrical leads were established using very lightweight CNT yarns (Nanocomp Technologies, Inc., NH) with one end attached to the electrode using a small bead of silver epoxy (MG Chemicals, B.C., Canada).

### 3.2.3 Fabrication of tape spring DEBA

The directional prestrains in the DE layers are critical in bending the laminates and thus creating the bistable shape, as well as determining the electromechanical response of the

laminated actuators. The top layer was prestrained unidirectionally in the  $y$ -direction ( $\epsilon_{yt}$ ) and the bottom layer was prestrained in both  $x$ -( $\epsilon_{xb}$ ) and  $y$ -directions ( $\epsilon_{yb}$ ) (Figure 3-3a). In our design the bottom layer serves as the active layer for electric actuation.  $x$ -direction prestrain ( $\epsilon_x$ ) helps develop bending moment about  $y$ -axis ( $M_y$ ), and the curvature in  $xz$ -plane thereby increases the area moment of inertia in about  $x$ -axis ( $I_x$ ) sufficiently to help stabilize state 1, while the additional prestrain in  $y$ -direction in the bottom layer ( $\epsilon_{yb}$ ) is applied to decrease its thickness of bottom layer to further increase the electric field produced during electrical actuation. The middle support layer with high elastic modulus helps hold the DE layers in the prestrained state and provides a zero-strain neutral plane for the resulting curved shape. Then the laminate was cut into tape spring shape (similar to the frog tongue) (Figure 3-3b). After the external stretch was released, the contractive stresses as shown in Figure 3-3c, contribute to equilibrium state 1 and 2, respectively (Figure 3-3d, e).

In order to actuate the bottom DE layer, two circular shaped electrodes and two CNT leads were attached to both electrodes (Figure 3-3a). The middle electrode was PEDOT:PSS and was printed on one side of support layer, while the bottom electrode was carbon grease and was brushed evenly on the bottom side of the bottom DE film. Two CNT yarns tip coated with silver epoxy were used to connect the electrodes and external voltage supply. The tape spring DEBA as shown in Figure 3-3d, e, was then mounted on the acrylic stage for shape characterization and electric actuation.

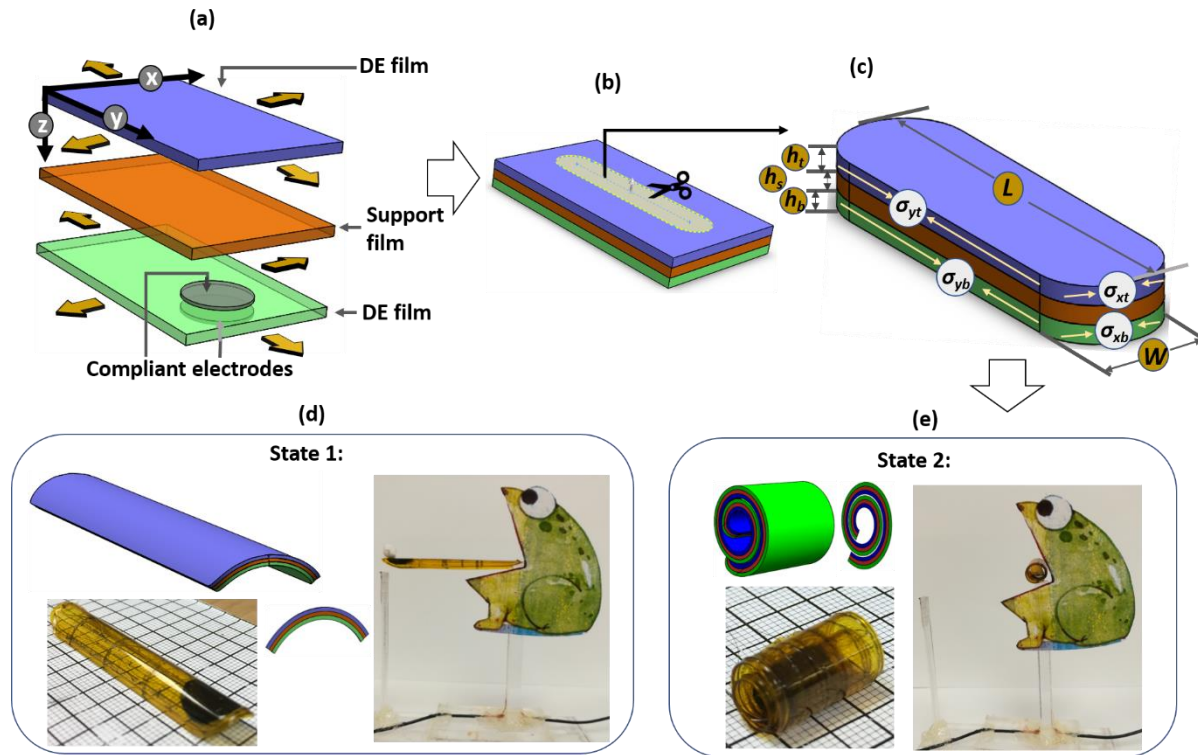


**Figure 3-3. Fabrication of tape spring DEBA.** (a) The top and bottom DE films are prestretched orthogonally, with a stiff support layer in the middle. A pair of compliant electrodes sandwich the bottom DE film for electric actuation. (b) The three layers are attached and cut along the dotted line, with a zoom-in shape in (c). After the removal of external constraints, the laminate self-equilibrates into (d) state 1 and, (e) state 2.

### 3.2.4 Experimental methods

After the fabrication, the bistable shape of tape spring DEBA was recorded by a two-camera imaging setup for subsequent image analysis. In the electric actuation step, the sample was connected to external high voltage supply, while the voltage output was controlled by the computer. Finally, the blocking force measurement was carried out by MTS tensile test equipment and results were visualized on the computer (Figure 3-4).

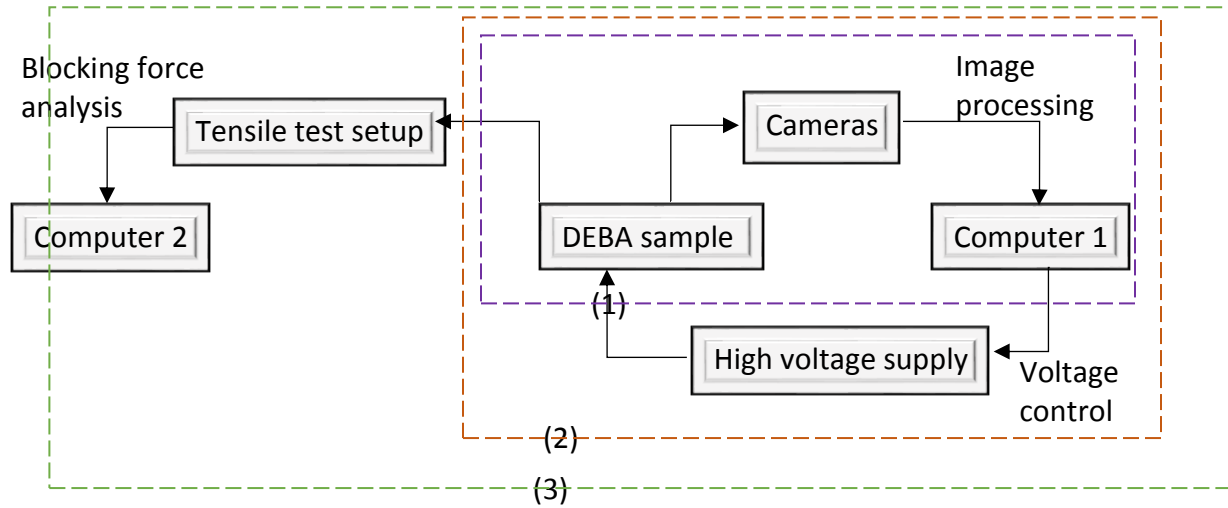


**Figure 3-4. Experimental flow of tape spring DEBA characterization.** The flows in brackets (1) (2) (3) represent bistable shape characterization, dielectric actuation and blocking force measurement, respectively.

### 3.2.4.1 Bistable shape characterization

Bistable shape was characterized by curvature in  $xz$ -plane ( $C_{xz}$ ) for state 1, and roll-up speed in  $yz$ -plane ( $S_{yz}$ ) for state 2. After fabrication steps, the tape spring DEBA was mounted on actuation stage made of acrylic board with embedded electric circuit. Two cameras were placed on  $xz$ -plane and  $yz$ -plane to capture the  $C_{xz}$ , and  $S_{yz}$  when tape spring DEBA was actuated from state 1 to state 2, respectively (Figure 3-5a, b). A tweezer is used to manually actuate the snap-through of the tape spring DEBA for  $S_{yz}$  measurement (Figure 3-5c). The results of bistable shape were visualized by Measurement and Automation Explorer, recorded by screen recorder (CamStudio™) and analyzed frame by frame with Image analysis program (Image J, NIH).

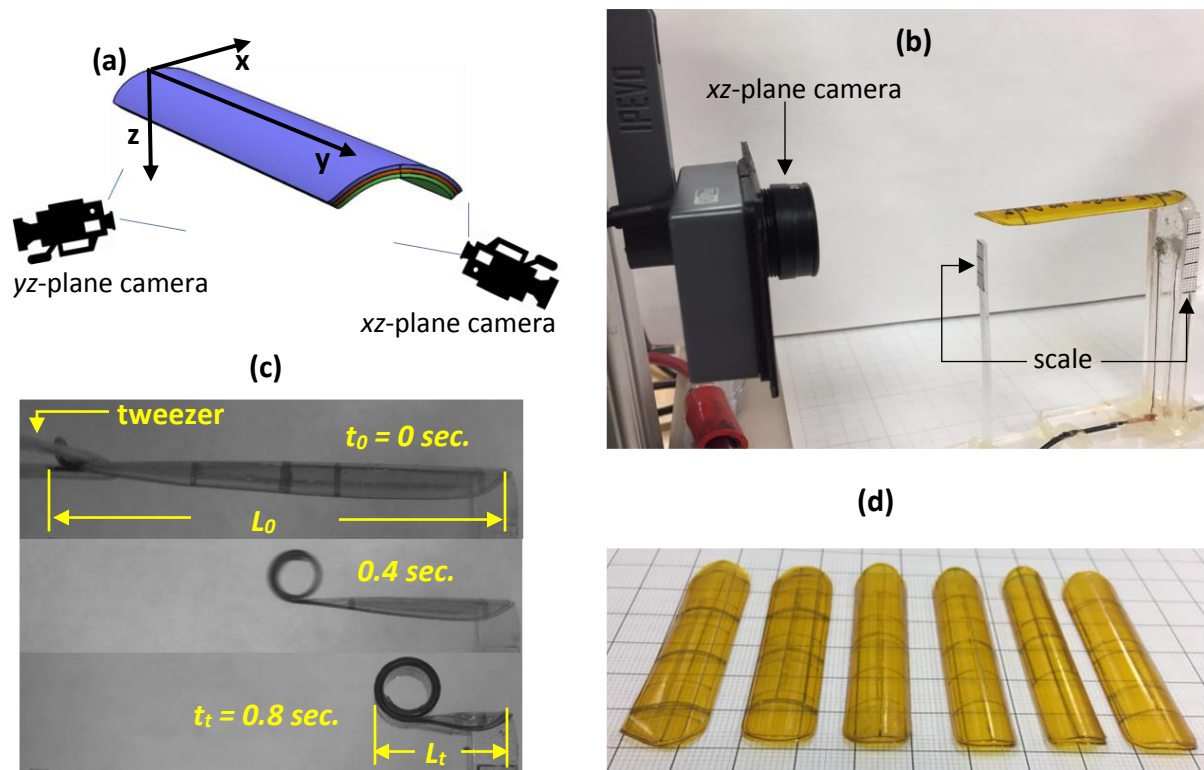


**Figure 3-5. Bistable shape characterization of tape spring DEBA.** (a) Schematic of two cameras in xz plane and yz plane. (b) Stage and camera setup for shape capturing. (c) Manually snapping the tape spring DEBA by tweezers. (d) A series of DE samples with  $\epsilon_{xb}$  as the variable.

### 3.2.4.2 Electrical actuation

We used CNT yarns tip coated with silver epoxy for reducing contact resistance, to connect the electrode with a Bertan 225-30R high-voltage power supply (Spellman High Voltage Electronics Corp., Hauppauge, NY). The voltage was increased at a constant rate of 500 V/sec from 0V. The voltage increment and visualization of snap-through behavior of the actuator were programmed by LabView and Measurement and Automation Explorer.

As applied voltage is increased, the movement of the tape spring can be described as two steps (Figure 3-6c). First step is the actuation part where the electric field induced expansion of the bottom DE layer begins to unbend the  $C_{xz}$  in the active part of the actuator,

leading to the reduction of  $I_x$ . This is followed by a rapid snap-through part which generates a displacement in the  $y$ -direction within seconds, characterized as  $S_{yz}$ . The critical voltage (or critical electric field) required to snap the actuator is defined as  $V_c$  (or  $E_c$ ). We used same camera setup as shape characterization in Figure 3-5a, b to record the change of  $C_{xz}$  and dynamic snap-through behavior. Image signal and real-time voltage were simultaneously presented on each frame in the video. The results were analyzed frame by frame with Image analysis program (Image J).

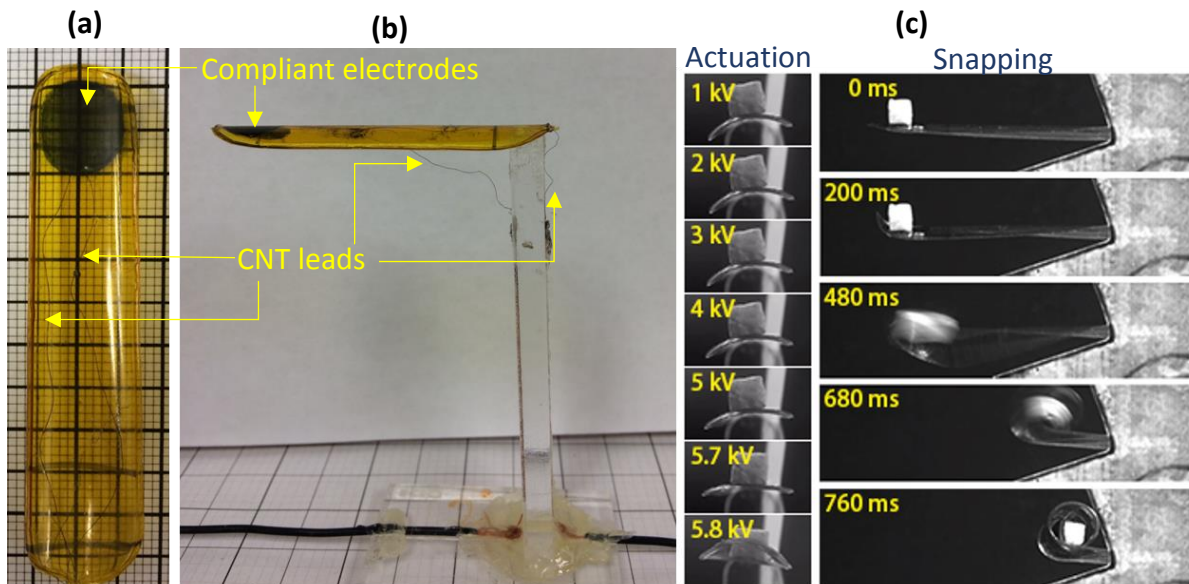


**Figure 3-6. Electric actuation of tape spring DEBA. (a)** tape spring DEBA sample. **(b)** Electric actuation setup. **(c)** Two steps of actuator movement: actuation step and snapping step.

### 3.2.4.3 Blocking force measurement

When the input voltage increases from 0V, the enhancement of actuation strain of the bottom DE layer unbends the actuator, leading to the reduction of  $C_{xz}$ . At the point when the external voltage reached the  $V_c$ , and the  $I_x$  is decreased to an extent not large enough to sustain

the  $M_x$  (induced by  $\epsilon_y$ ), the tape spring actuator snaps to state 2. The vertical force (z-axis) generated at the snap-through point is defined as the blocking force. At the snap-through point, the blocking force is captured by tensile test equipment (MTS Systems Corporation, MN). 1N load cell was used together with a 3D printed plastic (polymethacrylate) screw for force transduction and electrical insulation. One tip of screw is circular with a diameter of 6mm as contact surface between load cell and laminate actuator (Figure 3-7).

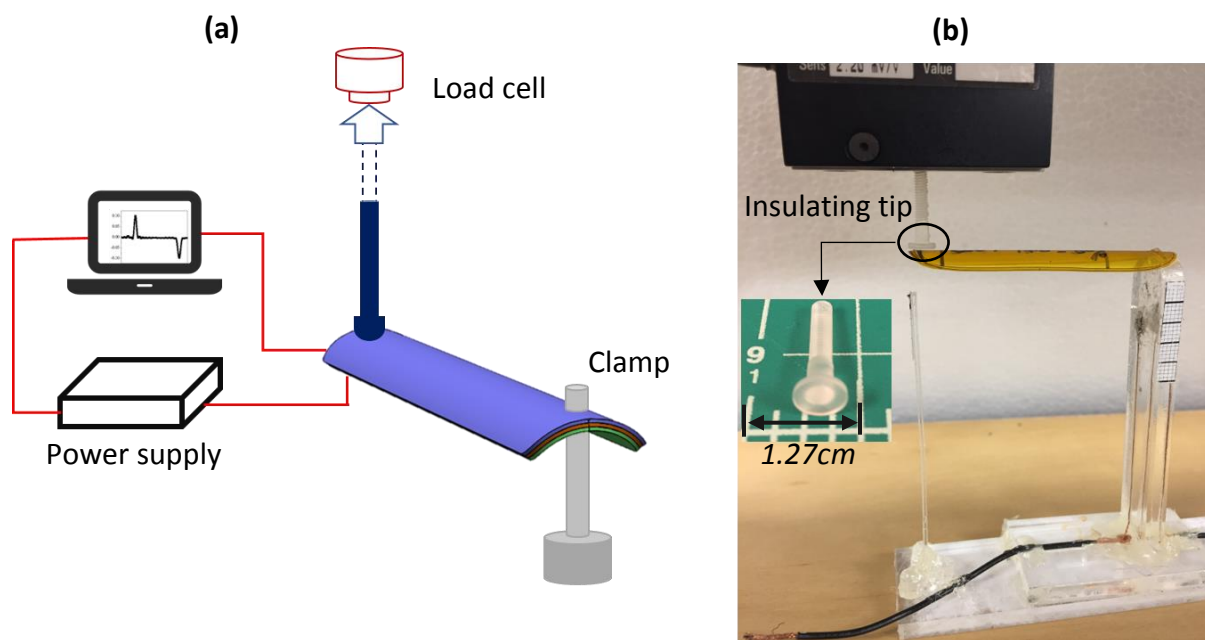


**Figure 3-7. Schematic of blocking force measurement.**

### **3.3 Results and Discussions**

#### **3.3.1 Bistable shape of tape spring DEBA**

The shape of the bistable laminated actuator is mainly determined by the applied prestrains on the top and bottom DE layers, as well as the bending modulus of middle support layer. The curvatures in  $xz$ -plane ( $C_{xz}$ ) of state 1, and the average roll-up speed along the  $y$ -

direction in  $yz$ -plane ( $S_{yz}$ ) were used to characterize the shape of the bistable structure. We selected  $S_{yz}$  but not curvature in  $yz$ -plane for shape characterization of state 2 due to the following reasons: (1) In our experiment design, speed is an important parameter of the actuator performance, showing the amplified power output. (2) Curvature of the actuator for state 2 is hard to determine because of the stacking of rolled part (Figure 3-3). Here we studied the influence of three important parameters (actuator dimension, prestrain level, as well as the stiffness of support layer) on the bistable shape of tape spring DEBA. In all cases, the  $x$ -direction prestrain in the top layer ( $\epsilon_{xt}$ ) was held at 0%.

#### **3.3.1.1 Effect of actuator dimension.**

To explore the effect of dimensional parameters on the bistable tape spring shape, the width of the bistable structure,  $W$ , was varied between 3- 35mm while the length  $L$  is held constant 35mm. Kapton film with thickness of 25 $\mu$ m and VHB 4905 were used, and the prestrain levels in the top and bottom layers were held constant at,  $\epsilon_{xb} = 30\%$ ,  $\epsilon_{yb} = 100\%$ , and  $\epsilon_{yt} = 200\%$ . The  $C_{xz}$  were plotted as a function of the non-dimensional parameter,  $W/L$  (Figure 3-8). As expected the curvature remains constant over the range of  $W/L$ , however, at higher values of  $W/L$ , the measured curvature seems to drop due to the material's own weight. Overall, we can still assume that the morphology of this bistable structure is independent of the dimension, which is supported by theoretical analysis of bistable shape (see Appendix).

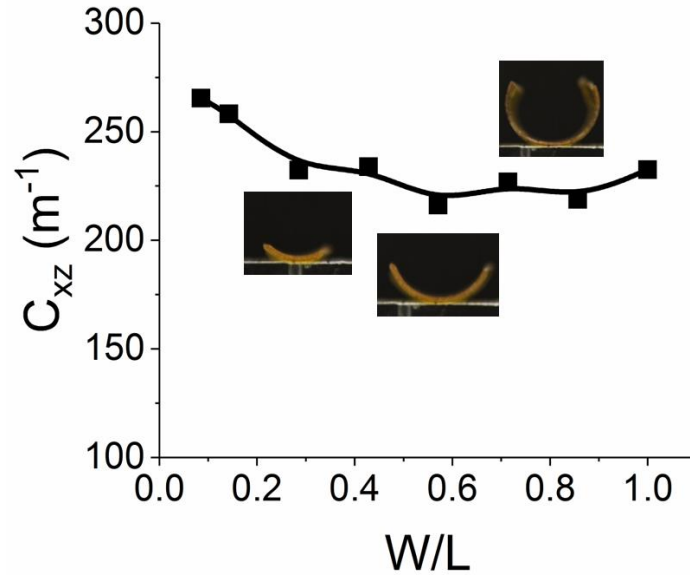


**Figure 3-8. Effect of actuator dimension on the bistable shape.**

### 3.3.1.2 Effect of prestrains

The variation of biaxial prestrains on DE layers brings about the change of film thickness, which amplifies the complexity of the bending behavior. As shown in the true stress-strain curve of VHB 4905 in Figure 3-1, we assume the elastic modulus of DE remains constant at various prestrains. Figure 3-1. Stress-strain curve of VHB 4905.

The effect of prestrains in the two DE layers was studied with VHB 4905 and Kapton with thickness of  $25\mu m$ , by systematic variation of one prestrain while keeping the other prestrains unchanged, and the dimension of actuator constant ( $W=15mm$ ,  $L=60mm$ ). and Table 3-4 showed the results of bistable shape change, and great consistency between experimental  $C_{xz}$  and theoretical  $C_{xz}$ .

In order to understand the bending behavior of the laminate and predict the morphology of the bistable shapes, we came up with theoretical analysis on the prestressed bistable laminate shape. The theoretical  $C_{xz}$  was derived by the standard force balance analysis

used in determining stress distribution in prestained concrete structures [125]. We assumed linear bending behavior of the laminate as well as ignore the loading due to gravity. The resulting equilibrium  $C_{xz}$  was expressed as following (see Appendix for calculation details),

$$C_{xz} = \frac{M_y}{EI_y} = \frac{2(\sigma_{xb}h_b^2 - \sigma_{xt}h_t^2)}{5E_a(h_t^3 + h_b^3) + E_s h_s^3} \quad \text{Equation 3-1}$$

where all parameters are listed in Table 3-1 and Figure A 1.

According to the equation, we noticed that the length ( $L$ ) and width ( $W$ ) of the tape spring DEBA have no effect on the  $C_{xz}$ , which is supported by the experimental results (Figure 3-8).

**Table 3-4. Effect of prestrains on the bistable shape of tape spring DEBA.**

	Prestrains on top layer		Prestrains on bottom layer		Experimental curvature ( <i>exp</i> $C_{xz}$ )	Calculated curvature ( <i>calc</i> $C_{xz}$ )	Roll-up speed ( $S_{yz}$ )
	$\epsilon_{xt}$	$\epsilon_{yt}$	$\epsilon_{xb}$	$\epsilon_{yb}$			
<b>Unit</b>	%	%	%	%	$m^{-1}$	$m^{-1}$	$mm/s$
<b>Effect of <math>\epsilon_{xb}</math></b>	0	200	<b>10</b>	100	153.246	64.78778	0
	0	200	<b>30</b>	100	155.3647	108.9768	0.862373737
	0	200	<b>50</b>	100	169.8413	115.1557	30
	0	200	<b>70</b>	100	158.6722	109.1923	90
	0	200	<b>90</b>	100	141.6968	99.41288	193.8
<b>Effect of <math>\epsilon_{yb}</math></b>	0	200	50	<b>20</b>	530.329	245.4036	0
	0	200	50	<b>40</b>	449.1761	200.0017	0
	0	200	50	<b>80</b>	221.883	136.8315	14.10815
	0	200	50	<b>100</b>	148.562	115.1557	80
	0	200	50	<b>120</b>	108.941	97.99686	138.23
	0	200	50	<b>160</b>	82.36	73.12295	238.367
<b>Effect of <math>\epsilon_{yt}</math></b>	0	<b>100</b>	50	100	100	95.08571	200
	0	<b>150</b>	50	100	130.35	107.2912	74.674
	0	<b>200</b>	50	100	170.6027	115.1557	46.965
	0	<b>250</b>	50	100	210.1959	120.4741	38.528
	0	<b>300</b>	50	100	225.5435	124.2371	35.24364
	0	<b>350</b>	50	100	257.1177	127.0049	35.52545

In the experimental part, when the  $\epsilon_{yt}$  and  $\epsilon_{yb}$  remained fixed at 200% and 100%, and  $\epsilon_{xb}$  was increased in steps, from 10% to 90%, the  $C_{xz}$  increased initially, reaching a peak, and then decreased, while  $S_{yz}$  increased continuously (Figure 3-9a). Increasing the  $\epsilon_{xb}$  has two effects on the shape of state 1:

(1) decreases the bottom layer thickness ( $h_b$ ) which reduces the bending stiffness of the laminate about  $x$  and  $y$ -axis;

(2) decreases  $h_b$  which lowers  $M_y$  (due to the decrease of  $e_b$ ), but increases  $M_x$ ;

(3) increases the contractile stress ( $\sigma_{xb}$ ) which contributes to the increase of  $M_y$ .

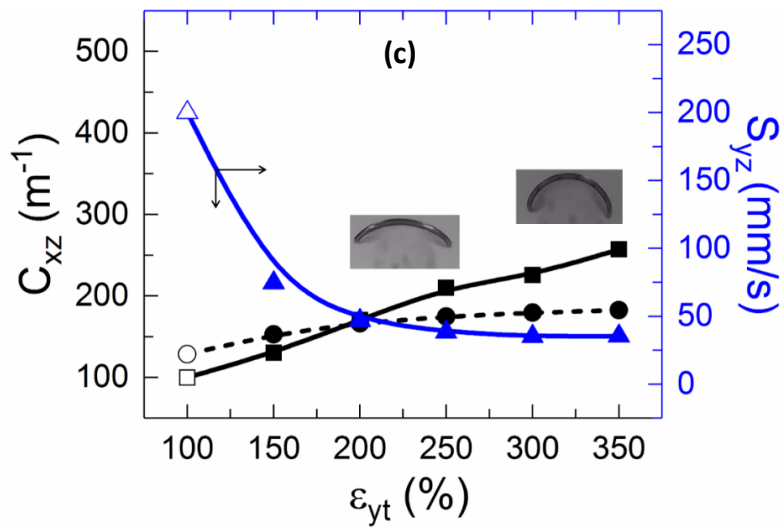
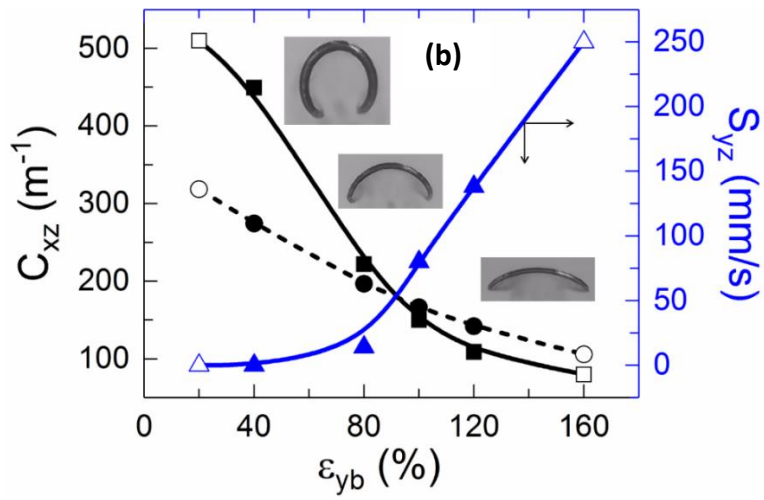
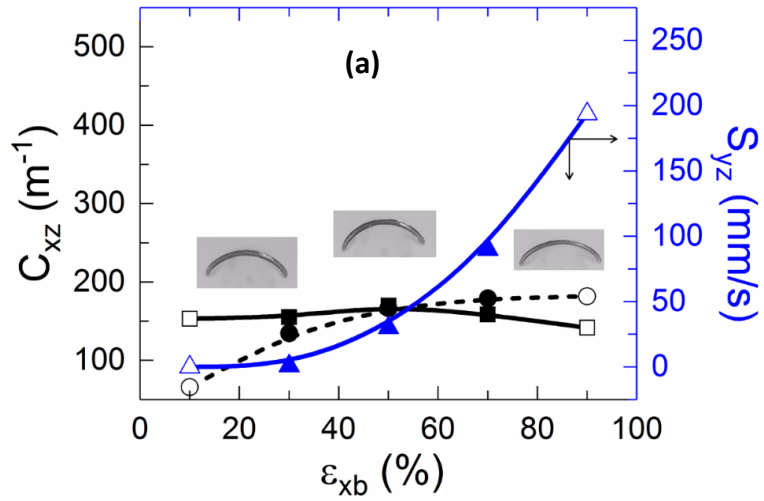
According to Equation 3-1, (1) and (3) have positive effect on building the curvature in  $xz$ -plane ( $C_{xz}$ ), while (2) exerts negative effect on that. (1) and (2) also exert positive effect on laminate's bending about  $x$ -axis, which is shown in Figure 3-9a as the increase in  $S_{yz}$ . More specifically, when  $\epsilon_{xb}$  is below 50%, the increase in  $M_y$  due to the rise of  $\sigma_{xb}$  as well as the reduction of  $EI_y$  have predominated effect on the enhancement of  $C_{xz}$ , while further increasing  $\epsilon_{xb}$ , the reduction of  $h_b$  plays a major role in reduction of  $M_y$  and thus reduces  $C_{xz}$ . Overall, the increase of  $\epsilon_{xb}$  leads to faster  $S_{yz}$ . This is because of the reduction of  $h_b$  and thus the decrease of bending stiffness ( $EI_x$ ).

On the other hand, if we increase the  $\epsilon_{yb}$  from 20% to 160%, and keep the other prestrain levels constant ( $\epsilon_{xb} = 50\%$ ,  $\epsilon_{yt} = 200\%$ ), the  $C_{xz}$  drops dramatically, and the  $S_{yz}$  keeps increasing (Figure 3-9b). Here we need to note that the continuous thickness drop in the bottom layer ( $h_b$ ) determines the monotonous reduction of  $C_{xz}$ . Because the increasing of  $\epsilon_{yb}$  reduces  $h_b$ , which decreases the  $M_y$  far more remarkably than the decrease of  $EI_y$ . Although  $S_{yz}$  increases monotonously, the effect of  $\epsilon_{yb}$  is a lot more complex. The increase of  $\epsilon_{yb}$  gives rise to

the  $\sigma_{yb}$  which lowers the overall  $M_y$ , and exerts negative effect on the enhancement of  $S_{yz}$ . However, the increase of  $\epsilon_{yb}$  also decreases  $h_b$ , which enhances the overall  $M_y$ , and thus help increase  $S_{yz}$ . Moreover, the resulting reduction of bending stiffness of the laminate improves  $S_{yz}$ . Right now, we cannot make quantitative explanation on this complex effect, but simply considering it as that the cumulative positive effects of  $\epsilon_{yb}$  increase on the transition speed (induces reduction in bending stiffness and improvement in bending moment  $M_y$ ) overcome the negative effect of  $\epsilon_{yb}$  increase (induces decrease in bending moment  $M_y$ ). This consideration is in consistency with the phenomenon seen in Figure 3-9a, where  $C_{xz}$  starts to go down when  $\sigma_{xb}$  keeps increasing.

Lastly, we increased the  $\epsilon_{yt}$  from 100% to 300%, in steps of 50%, while keeping other prestrains constant ( $\epsilon_{xb}=50\%$ ,  $\epsilon_{yb}=100\%$ ), and the  $C_{xz}$  of the tape spring DEBA increases almost linearly (Figure 3-9c), while the  $S_{yz}$  drops. The rise of  $C_{xz}$  is simply owing to the reduction of  $EI_y$  induced by the decrease of  $h_t$ . Although  $S_{yz}$  decreases monotonously, the complexity effect of  $\epsilon_{yt}$  on this transition speed is similar to the monotonous  $S_{yz}$  increase. Again, the induced reduction of  $h_b$ , the resulting reduction in bending stiffness, and two opposite induced change in  $M_y$ , can only be simplified as such: the negative effect of  $\epsilon_{yt}$  increase on the transition speed (reduction in  $M_y$ ) overcomes the positive effect of  $\epsilon_{yt}$  increase (reduction in bending stiffness, enhancement in  $M_y$ ).

**Figure 3-9. Effect of prestrains on the bistable shape.** The  $C_{xz}$  (solid black line, ■),  $S_{yz}$  (solid blue line, ▲) and calculated  $C_{xz}$  (dotted black line, ●) change as we changed **(a)** prestrain in x direction in the bottom layer ( $\epsilon_{xb}$ ), **(b)** prestrain in y direction in the bottom layer ( $\epsilon_{yb}$ ), and **(c)** prestrain in the y direction in the top layer ( $\epsilon_{yt}$ ), while other prestrains were kept constant. Filled symbols represent bistable samples, and unfilled symbols represent monostable samples.



In this section, we demonstrated the importance and complexity of the prestrain combinations of DE layers on the bistable shape of the tape spring actuator. Excitingly, the experimental results and theoretical analysis are highly consistent. However, there are still limitations required further improvement:

Theoretically, we made some assumptions:

(1) Curvature in xz-plane is small, and the materials are linearly elastic (to comply with the Euler-Bernoulli beam theory). (However, in the real case, the experimental curvatures of under some prestrain combinations are quite large; and from the stress-strain curve, DE film has viscoelastic property, albeit small)

(2) In calculating the bending moments, we assume that support layer serves as neutral plane, and the stresses in DE layers along z axis decrease linearly from the neutral plane ( $\sigma$  is obtained from true stress strain curve of VHB 4905), to the most outside of the DE layers ( $\sigma=0$ ).

(3) The flexural rigidity of the trilayered laminate follows the bending behavior of symmetrical sandwiched beam, with some modification.

Experimental derivations are:

(1) The manual process of laminate fabrication might induce some prestrain derivation, and misalignment in laminating the three layers.

(2) The manual cutting (with blade) of the laminate into tape spring (frog tongue) shape might induce small stress redistribution at the boundary.

(3) Although the VHB 4905 tape has generally good adhesion to the support layer (Polyimide and PET), there is still small shrinkage on the boundary of the laminate (around 1mm).

(3) In the shape imaging process, we fix the scale at a constant related spatial distance to the tape spring actuator (Figure 3-5b), which eliminates the variation of the results among samples. However in the image, the value of  $C_{xz}$  is dependent on the related distance between scale and sample, there is inevitable derivation of the  $C_{xz}$  captured from camera to the real  $C_{xz}$ .

### 3.3.1.3 Effect of stiffness of support layer

To elucidate the effect of modulus of support layer, we performed further experiments with two types of support layer (PET film, Kapton film), and compared the shape differences of the tape spring DEBA. PET film has the elastic modulus almost twice of the Kapton film (Table 3-2). The dimension of the tape spring DEBA is same throughout the experiment, unless specified ( $L = 60mm$ ,  $W = 15mm$ ). The experimental results are shown in Table 3-5 and Figure 3-10.

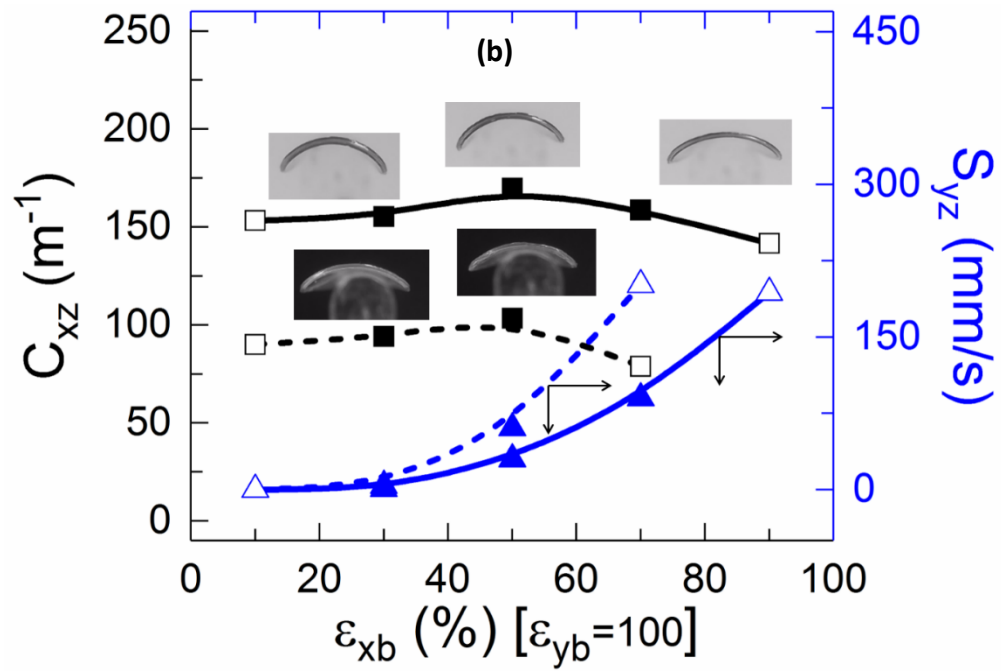
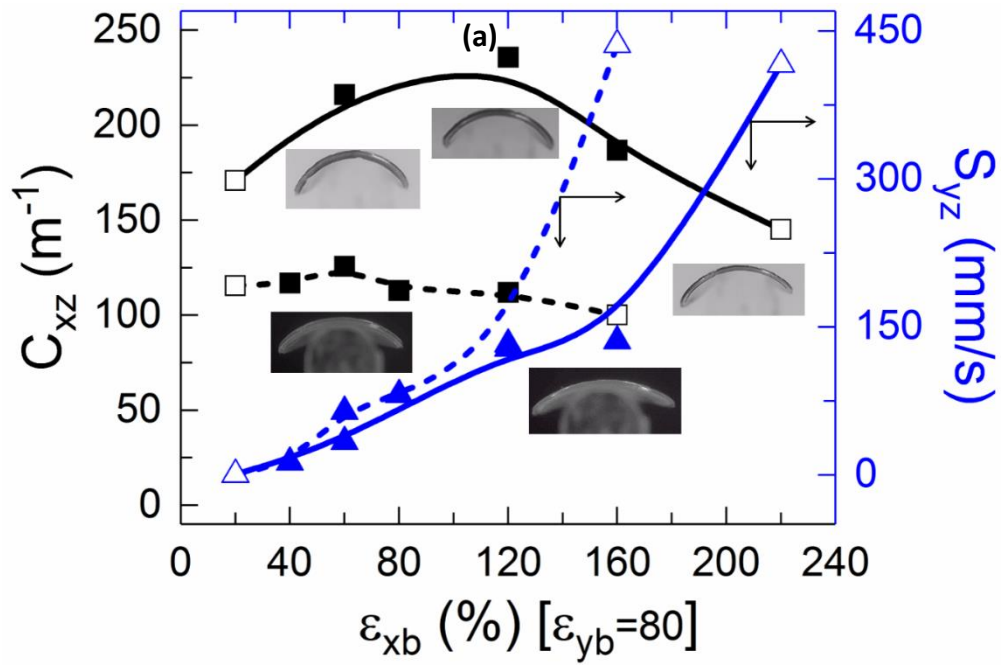
**Table 3-5. Effect of support layer stiffness on the bistable shape of tape spring DEBA. “-” means no reading because the sample is monostable in state 2 (cannot self-equilibrate in state 1).**

Prestrains on top layer		Prestrains on bottom layer		$C_{xz}$ -Kapton as support layer	$C_{xz}$ -PET as support layer	$S_{yz}$ -Kapton as support layer	$S_{yz}$ -PET as support layer
$\epsilon_{xt}$	$\epsilon_{yt}$	$\epsilon_{xb}$	$\epsilon_{yb}$				
%	%	%	%	$m^{-1}$	$m^{-1}$	$mm/s$	$mm/s$
0	200	<b>20</b>	80	170.9067	115.6368	0.553	0
0	200	<b>60</b>	80	216.0838	125.6899	33.72727	64.48833
0	200	<b>120</b>	80	235.7329	111.9672	128.3667	132.3767
0	200	<b>160</b>	80	186.7987	100.1256	135.8333	436.16
0	200	<b>220</b>	80	145.1498	-	416	-
0	200	<b>10</b>	100	153.246	90	0	0
0	200	<b>30</b>	100	155.3647	94.09129	0.862373737	3.885366
0	200	<b>50</b>	100	169.8413	103.4586	30	60.74667
0	200	<b>70</b>	100	158.6722	78.91236	90	201.36
0	200	<b>90</b>	100	141.6968	-	193.8	-

By increasing  $\epsilon_{xb}$  from 20% to 220%, while keeping other prestrains constant ( $\epsilon_{yb}=80\%$ ,  $\epsilon_{yt}=200\%$ ),  $C_{xz}$  of Kapton supported laminate is larger than  $C_{xz}$  of PET supported laminates, and both increases, shows a peak of maximum  $C_{xz}$ , and then decreases.  $S_y$  increases in both groups while the PET supported laminates has lower  $S_{yz}$  than the Kapton supported laminates. Moreover, they are both monostable in state 1 when  $\epsilon_{xb}$  is 20%. And as the  $\epsilon_{xb}$  increases, both groups become bistable until PET supported laminate stays monostable in state 2 when  $\epsilon_{xb}$  is 160%. However, Kapton supported laminate becomes monostable in state 2 when  $\epsilon_{xb}$  reaches 220% (Figure 3-10a). In the second plot, we elevate  $\epsilon_{yb}$  to 100%, and keep  $\epsilon_{yb}=100\%$ ,  $\epsilon_{yt}=200\%$ . Then we increase the  $\epsilon_{xb}$  from 10% to 90%. The resultant  $C_{xz}$  of both PET and Kapton supported laminates (Figure 3-10b) are lower than those in the first plot (when  $\epsilon_{yb}$  is constant at 80%), and the bistable range (regarding the  $\epsilon_{xb}$  change) is smaller. In another word, the difference of  $\epsilon_{yb}$  results in differences in bistable shape and bistability of the laminate (explanation of this phenomenon can refer to Chapter 3.1.1.2 Effect of prestrains).

Overall, the modulus of support layer is demonstrated to be significant in the bistable configuration, while the higher modulus results in smaller  $C_{xz}$  and  $S_{yz}$ , as well as smaller bistable range when we varied the prestrains. For the bending behavior of a simple beam or sheet, the bending stiffness is directly proportional to the elastic modulus. Kapton has about half elastic modulus (2.5 *Gpa*) of PET (4.9 *Gpa*), and thus exerts about half resistance to bending compared to PET, which illustrated in the bistable shape of tape spring DEBA as almost twice  $C_{xz}$ .

**Figure 3-10. The effect of support layer stiffness on the bistable shape.** PET ( $E=4.9\text{GPa}$ ) and PI ( $E=2.5\text{GPa}$ ) as support layers.  $C_{xz}$  (■) and  $S_{yz}$  (▲) of the tape spring actuator with PET (dash line), and PI (solid line) as support layer plotted as a function of, **(a)** x-direction prestrain in the bottom layer ( $\epsilon_{xb}$ ), while  $\epsilon_{xt}= 0\%$ ,  $\epsilon_{yb}= 80\%$ ,  $\epsilon_{yt}= 200\%$  are held constant, and **(b)** x-direction prestrain in the bottom layer ( $\epsilon_{xb}$ ), while  $\epsilon_{xt}= 0\%$ ,  $\epsilon_{yb}= 100\%$ ,  $\epsilon_{yt}= 200\%$  are held constant. Filled symbols represent bistable samples, and unfilled symbols represent monostable samples.



### 3.3.2 Bistability analysis of tape spring DEBA

While changing the prestrains of the DE layers, the resulting laminated structure was not always bistable. For example, if the flexural rigidity ( $EI_x$ ) about  $x$ -axis is not large enough to resist the bending moment ( $M_x$ ) induced by prestrains in  $y$ -direction ( $\varepsilon_y$ ), the laminated structure would result in monostable in state 2. Otherwise, if the  $EI_x$  is too large for the  $M_x$  to bend the laminates, and the structure would result in monostable in state 1. Note  $I_x$  is the area moment of inertia of the bent laminate in state 1 (bent state) in  $xz$ -plane.

In order to further analyze the bistability of the tape spring actuator, we evaluate the flexural rigidity of the bent shape in  $xz$ -plane, about  $x$  axis ( $EI_x$ ), and the bending moment induced by biaxial prestrains of two DE layers ( $M_x, M_y$ ). We adopted two parameters for defining bistability range. One is the  $C_{yz}$  in state 1 (see details in Appendix), while the other is the ratio of bending moment about  $x$  axis and  $y$  axis ( $M_x/M_y$ ) (see details in Appendix).

Due to the dimensional factor ( $L \gg W$ ) and extreme stiffness difference between the support layer and the DE layers ( $E_s \gg E_d$ ), there is no curvature observable in  $yz$ -plane  $C_{yz}$  when actuator was in state 1 (See Appendix for detailed derivation). However, Pezzulla, M. et al [126] found there is a small amount of curvature confined to a boundary layer at the edges. Besides,  $C_{yz}$  (in state 1) can be expressed as  $M_x/EI_x$  according to beam bending theory. The results shown in Figure 3-11a are plotted for all combinations of prestrains we conducted previously (Figure 3-9). Interestingly, the results illustrate the bistable range of the tape spring actuator in terms of  $C_{yz}$  (in state 1), despite of the low magnitude. This curvature-driven bistability is consistent with the snap-through behavior of cylindrical shells subjected to a decreasing curvature [127].

Another analogous way to evaluate the shape bistability is simply comparing the bending moment about x axis ( $M_x$ , induced by prestrains in y direction), and bending moment about y axis ( $M_y$ , induced by prestrains in x direction). The results shown in Figure 3-11b is  $M_x/M_y$  plotted with variables same as those in Figure 3-11a. The clear separation of bistability and monostability of the tape spring actuator again validates the observation we made earlier in Figure 3-11a. See Appendix for detailed derivation of moment ratio.

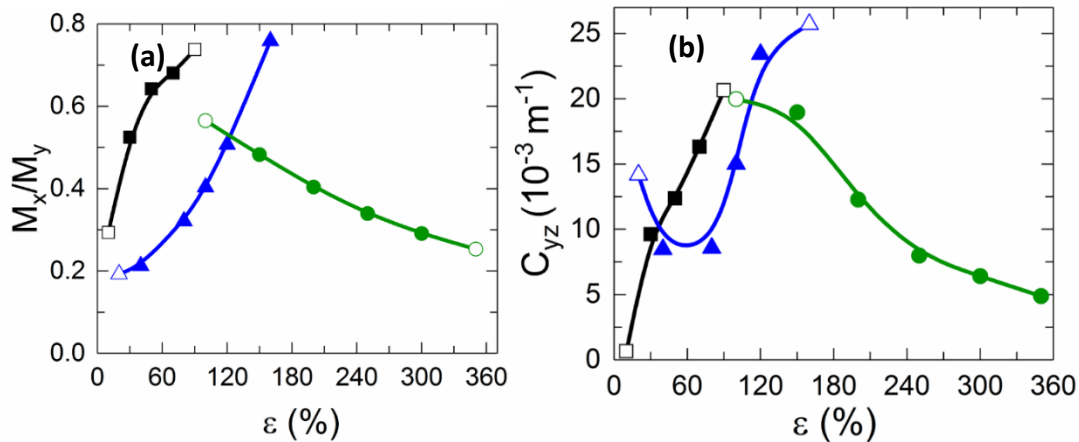


**Figure 3-11. Prestrain-dependent bistability of the tape spring DEBA. (a)**  $C_{yz}$  in state 1, and **(b)** the division of bending moment about x axis ( $M_x$ ) and bending moment about y axis ( $M_y$ ). Solid dots represent bistable samples, and unfilled dots represent monostable samples.

The difference between two plots is that the moment ratio ( $M_x/M_y$ ) is a calculated parameter, whereas the curvature of the actuator in yz-plane ( $C_{yz}$ ) is half calculated and half experimental ( $I_x$  is calculated from curvature of the bent shape in xz-plane,  $C_{xz}$ ). Although the two results can to some extent define the boundary of bistability in this experiment, there are limitations due to assumptions and experimental deviations:

Assumptions: In addition to the assumptions made in Chapter 3.3.1.2, we also assume the bending stiffness (flexural rigidity) of the curved laminate. Here in order to simplify the

calculation of bending stiffness of the bent shape in  $xz$ -plane, we follow the “Rule-of-Mixture” used in determining stiffness of fiber-reinforced composites [128], and assume the bent laminate in  $xz$ -plane is an arc of a ring. Experimental deviations (See Chapter 3.3.1.2).

Thus, further improvement of the theoretical analysis and computer modeling is required in the future work.

### **3.3.3 Electromechanical response of tape spring DEBA**

The bistable tape spring actuator was electrically activated by applying appropriate electric field using a pair of compliant electrodes attached to both sides of the bottom DE layer. The principle of DE actuation is described in Chapter 2.1.1. Under the electric field, the compliant electrodes provide compressive force to the DE film, which induces lateral expansion with minimum mechanical constraint from the electrodes. Therefore, when the DE layer is electrically activated in a laminate structure, an in-plane stress potentially induces bending moment of the laminate [126]. In our case, this mechanism was used to unbend the bistable tape spring actuator in state 1, resulting in lower  $I_x$  in the  $xz$ -plane (actuation part), and thereby trigger the snapping of the bi-stable structure (snapping part) (Figure 3-6c). The DE actuation mechanism, and comparison between flat DE actuation and tape spring DEBA actuation is shown in Figure 3-12.

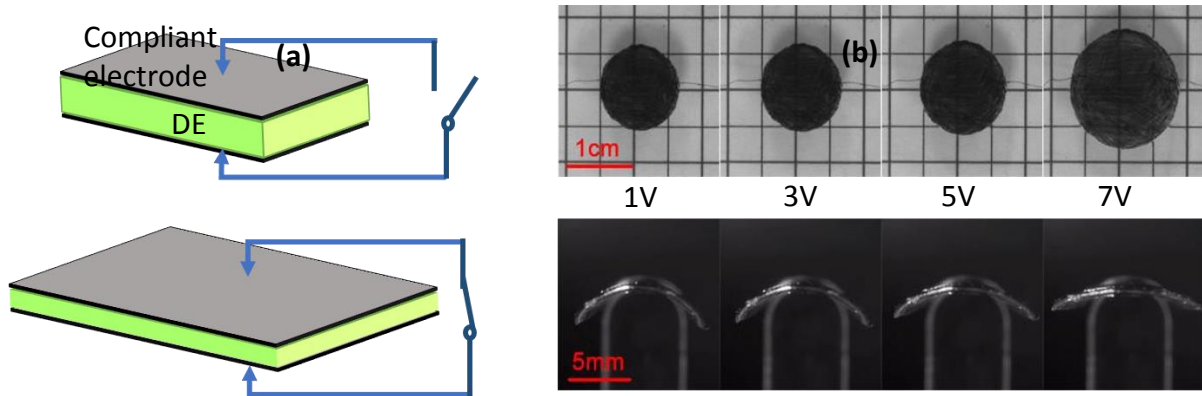


**Figure 3-12. Dielectric polymer based bistable tape spring actuation mechanism. (a)** Schematic illustration of a dielectric polymer actuation mechanism. **(b)** Optical images showing the electric actuation process of a flat DE actuator and our tape spring DEBA. The biaxial prestrains of the flat actuator is the same as the biaxial prestrains on the bottom DE film of the tape spring DEBA.

The critical actuation voltage required for snapping ( $V_c$ ), as well as the critical actuation electric field ( $E_c$ , calculated with  $V_c$  and nominal thickness of prestrained bottom DE layer,  $h_b$ ), are investigated as a function of prestrain of DE layer ( $\epsilon_{xb}$ ), electrode position ( $l/L$ ), and electrode size ( $d/W$ ).

The influence of prestrain on dielectric actuation was studied by using  $25\mu\text{m}$  thick PET film as support layer, and VHB 4905 as two DE layers, and  $\epsilon_{yt} = 200\%$ ,  $\epsilon_{yb} = 80\%$ ,  $\epsilon_{xt} = 0\%$  were remained constant, while  $\epsilon_{xb}$  was increased from 60% to 180%, in steps of 60%. Note that PEDOT:PSS and carbon grease with diameter of 11 mm were used as middle and bottom electrodes, respectively. As a result,  $V_c$  was decreased, but the  $E_c$  was increased (Figure 3-13). The reduction of  $V_c$  from 7.3 kV to 5.8 kV is prominent, which might be due to the overwhelming bottom layer thickness decrease and some minor reduction of curvature in  $xz$ -plane,  $C_{xz}$  (Table 3-6).

The increase in  $E_c$  might result from several factors:

(1) Larger constraint effect imposed on the DE film with the reduction of  $h_b$ , as the induced in-plane strain closer to the support layer is further limited.

(2) Prestrain-decreased relative dielectric constant of VHB ( $\epsilon_r$ )[49] imposes higher  $E_c$  to induce the critical actuation stress.

**Table 3-6. Effect of prestrain on the snap-through of tape spring actuator (25 $\mu$ m thick PET is utilized as support layer).**

Prestrains on the top layer		Prestrains on the bottom layer		Thickness of bottom layer ( $h_b$ )	Initial curvature in $xz$ -plane ( $C_{xz}$ )	Critical Voltage ( $V_c$ )	Critical electric field ( $E_c$ )
$\epsilon_{xt}$	$\epsilon_{yt}$	$\epsilon_{xb}$	$\epsilon_{yb}$				
%	%	%	%	$\mu\text{m}$	$\text{m}^{-1}$	kV	$\text{V}/\mu\text{m}$
0	200	60	80	173.6	111.8	7.3	42.0
0	200	120	80	126.3	110.1	6.0	47.5
0	200	180	80	99.2	106.6	5.8	58.5

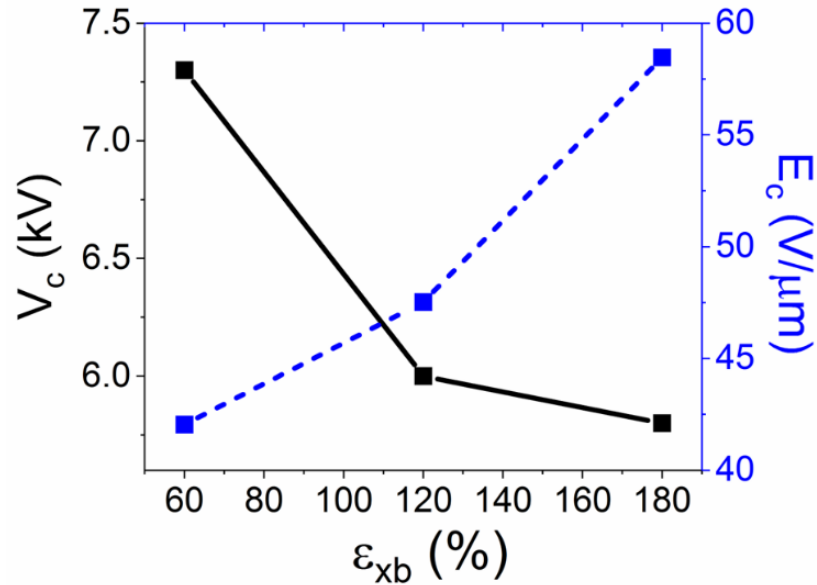


**Figure 3-13. Influence of prestrain on the snap-through of tape spring actuator.** The  $\epsilon_{xb}$  is a variable while other prestrains are kept constant ( $\epsilon_{yt} = 200$ ,  $\epsilon_{yb} = 80$ ,  $\epsilon_{xt} = 0$ ) (25 $\mu\text{m}$  thick PET is utilized as support layer).

The relationship between  $E_c$  and electrode position ( $l/L$ ) was investigated by keeping prestrains constant ( $\epsilon_{xb} = 80\%$ ,  $\epsilon_{yb} = 100\%$ , and  $\epsilon_{xt} = 0\%$ ,  $\epsilon_{yt} = 160\%$ ). As shown in Figure 3-14, the  $E_c$  increases as the active area was placed further away from the free end of the tape spring structure. Obviously, the electrode distance away from the free end imposes higher levels of boundary constraints on the active area from all sides of the actuator and the overall work required to snap is higher. Thus, the optimal electrode position for actuation of bistable tape spring structure is that closest to the free end of the structure. Here we should notice that the electrodes were placed sufficiently away from the edges of the laminate, to avoid charge leakage.

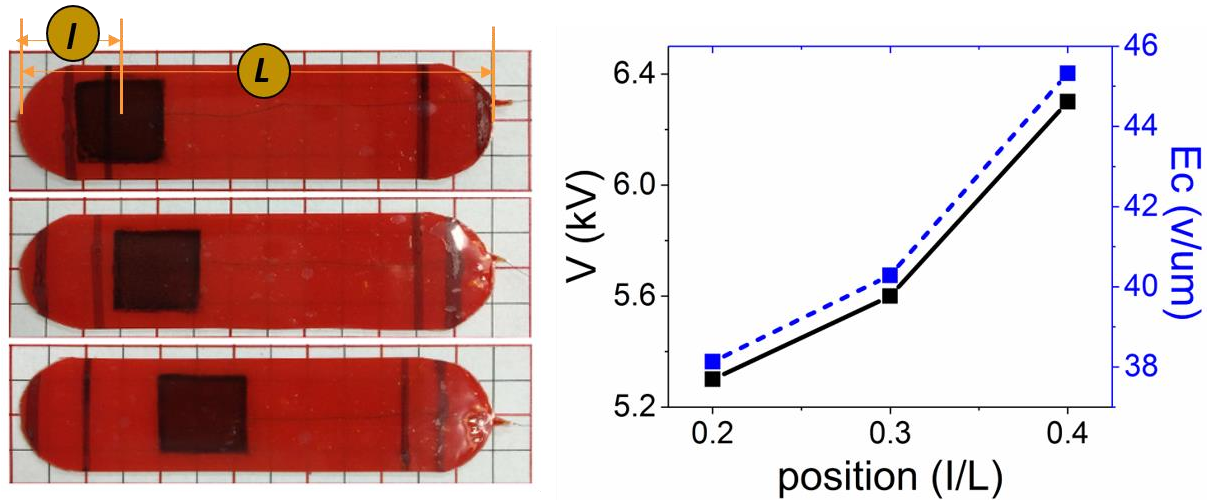


**Figure 3-14. Influence of electrode position on the snap-through of tape spring actuator.**

The influence of electrode size on the tape spring DEBA actuation was investigated by altering the ratio of the electrode diameter and width of the tape spring DEBA ( $d/W$ ), while keeping prestrains constant ( $\epsilon_{xb} = 80\%$ ,  $\epsilon_{yb} = 100\%$ , and  $\epsilon_{xt} = 0\%$ ,  $\epsilon_{yt} = 160\%$ ). Figure 3-15 showed almost linear reduction of  $E_c$  with decreasing  $d/W$  ratio while the electrode position remains fixed, which is predictable because larger electrode area induces higher Maxwell force, leading to larger actuation strain under the same electric field. Again, to avoid charge leakage at boundary of the laminate, there is a maximum electrode size.

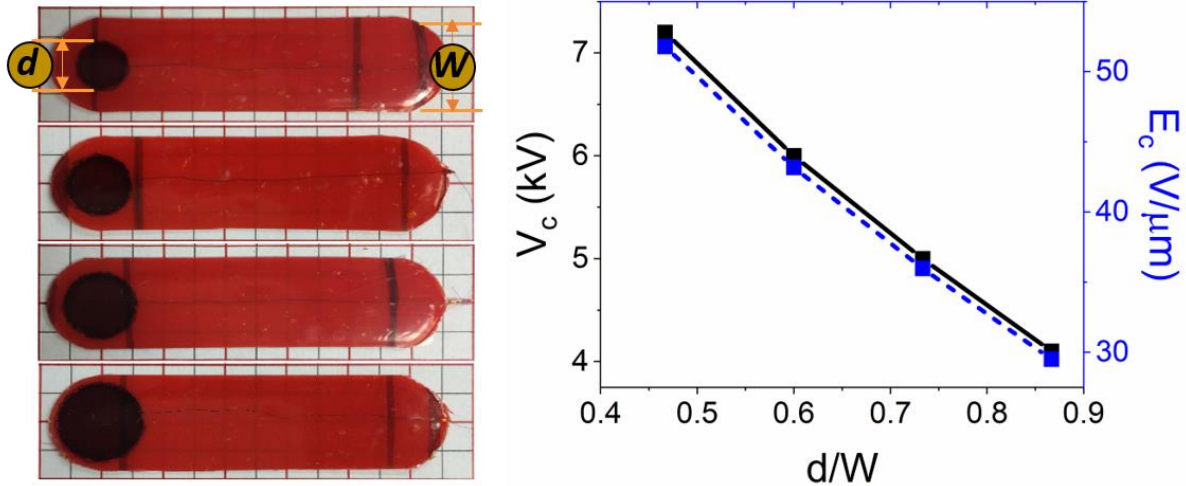
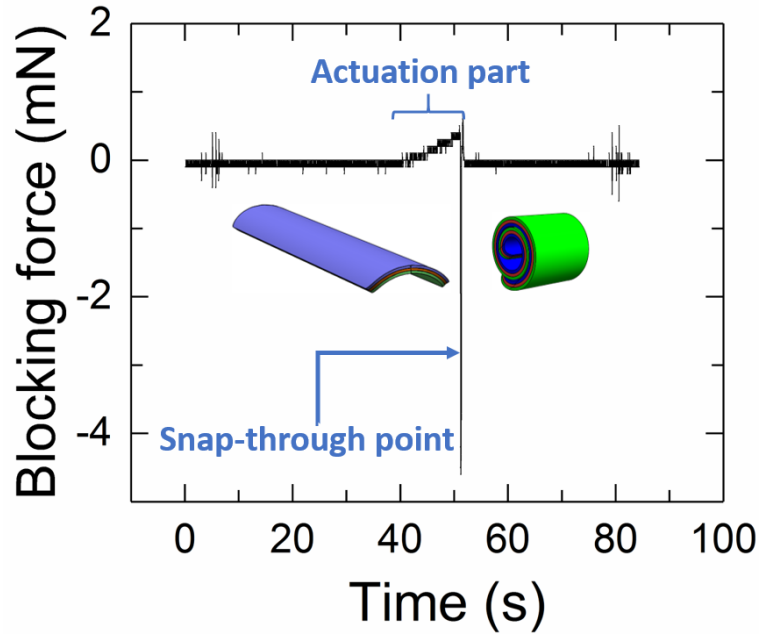


Figure 3-15. Influence of electrode size on the snap-through of tape spring actuator.

### 3.3.4 Blocking force of the tape spring DEBA

When the applied electric field reached the level of critical electric field ( $E_c$ ), the tape spring DEBA snaps from state 1 to state 2, and the vertical force (along  $z$  axis) generated at the snap-through point is defined as the blocking force, which was captured by MTS tensile test machine (Figure 3-7). For the tape spring actuator with  $\epsilon_{xb} = 60\%$ ,  $\epsilon_{yb} = 80\%$ ,  $\epsilon_{yt} = 200\%$ , the external power supply took 13 seconds to increase the input electric field from 0 to the  $E_c$  ( $44.35 \text{ V}/\mu\text{m}$ ), at a voltage increment speed of  $100\text{V}/200\text{ms}$ . Upon snap-through, the blocking force was measured to be around  $4.5\text{mN}$ .



**Figure 3-16. Blocking force of tape spring actuator.** Prestrains of the actuator were kept at  $\epsilon_{xb}=60\%$ ,  $\epsilon_{yb}=80\%$ ,  $\epsilon_{xt}=0\%$ ,  $\epsilon_{yt}=200\%$ .

### 3.4 Conclusion

In this work, we explored the dielectric elastomer (DE) in a novel way, by incorporating smart structure (bistable tape spring structure) and smart material (dielectric electro-active material) into a simple laminated morphing system. Compared to other novel actuation stimuli such as solvent, heat and light, the electrical actuation of DE is easier to conduct and control. In addition, the bistable structure lowers the energy consumption and reduces the possibility of electric breakdown of DE. Moreover, the prestraining of DE layers help create and tune the bistable structure of the tape spring DEBA, promote the morphing speed due to the rapid relaxation of the elastic energy, as well as enhance the electric field during electrical actuation. This all-polymer actuator has very lightweight (0.3g), desirable in-plane robustness and out-of-plane flexibility, fast transition speed (up to 150mm/s), large displacement (length direction), moderate actuation electric field (40-60V/ $\mu\text{m}$ ) with blocking force of 4.5mN.

We demonstrate simple fabrication process of the bistable tape spring actuator, by laminating prestrained DE films and a polymer film. The DE films serve both as structural and active element, and stiff polymeric layer served as neutral plane for bending. Bistable shape and actuator performance can be easily tuned by varying prestrain combination on the DE layers, or the stiffness of support layer, within the structural bistability range. Our theoretical analysis on the bistable shape and bistability provides qualitative guidance to the design of bistable structures. We also demonstrate electric field induced morphing/snapping behavior of the actuator and elucidate the actuation effect of multiple parameters (prestrain combination, electrode size and electrode position). The dielectric actuation of the tape spring DEBA

demonstrate that the critical electric field ( $E_c$ ) for snap-through is around  $40\text{-}60\text{ V}/\mu\text{m}$ , and the corresponding critical voltage ( $V_c$ ) is about  $6\text{ kV}$  to  $7.5\text{ kV}$ .

## Chapter 4 Conclusion and Future Perspectives

An all-polymer light-weight tape spring DEBA is fabricated through simple prestretching-laminating process. The tape spring DEBA has shown tunable initial bistable shape originated from the elastic energy of the biaxially prestrained DE films and stiffness of the support layer. Upon activation with an external electric field around  $40\text{-}60\text{ V}/\mu\text{m}$ , it snaps from one stable state to the other within few seconds and sustains the deformed shape by itself, and generate the blocking force of  $4.5\text{ mN}$  at the snap-through moment in the vertical direction. This novel DEA structure addressed two issues of dielectric actuation and actuator assembly:

1. Most current DEA works under continuous external voltage supply to maintain the deformation or force, which induces more possibility of dielectric breakdown. In the tape spring DEBA, the activation voltage is only needed to unbend the structure in one stable state, which is followed by rapid snap-through due to the total energy minimization in the laminate.
2. Prestretching is an important process for most DE to decrease voltage supply, which requires a rigid frame to maintain the prestretch. The additional frame increases the volume and weight of the system. In the tape spring DEBA, the functionality of rigid frame replaced by an ultrathin polymer layer ( $25\mu\text{m}$  thickness) with high Young's modulus. The support layer well maintains the prestrain level in DE, as well as serves as neutral plane for bilateral bending. The whole tape-spring DEBA is only  $0.3\text{g}$ .

The prestrain level in two DE layers and stiffness of support layer play important role in the bistable shape, snapping speed, bistability of the structure as well as the actuation voltage required. We developed theoretical analysis in the prestraining-bending behavior, and the calculated bent shape is in great consistency with the experimental results. Prestrain-induced bistable range is also estimated theoretically.

This work only touches the surface of prestrain-induced bistable structure and bistable DEA. There are several assumptions we made for the theoretical analyses, such as small deflection for Euler-Bernoulli theory. The analyses need to be further revised and confirmed with more experimental results and computer simulation. We are continuously working on simulations methods and incorporating them into this experimental model. Besides, due to the limited DE thickness available commercially, we cannot make further inspection on the influence of DE thickness that is very crucial. Moreover, the bilateral actuation is not conducted for tape-spring actuator, due to the very low energy state for state 2. Besides this work, further investigation could be conducted as following:

1. Conducting simulation on the bistable shape and actuation of the prestrained laminate.
2. Improve theoretical model in the bistable shape and bistability.
3. Acquiring DE with more choices of thickness.
4. Further improve the actuation strain of the constrained DE.
5. Assembling the bistable unit into useful actuator application.

## REFERENCES

- [1] Y. Forterre, J. M. Skotheim, J. Dumais, and L. Mahadevan, "How the Venus flytrap snaps," *Nature*, vol. 433, no. 7024, pp. 421–425, Jan. 2005.
- [2] S. N. Patek, W. L. Korff, and R. L. Caldwell, "Biomechanics: Deadly strike mechanism of a mantis shrimp," *Nature*, vol. 428, no. 6985, p. 819, Apr. 2004.
- [3] S. M. Deban, D. B. Wake, and G. Roth, "Salamander with a ballistic tongue," *Nature*, vol. 389, no. 6646, p. 27, Sep. 1997.
- [4] "The Wright Brothers | The First Successful Airplane." [Online]. Available: <https://airandspace.si.edu/exhibitions/wright-brothers/online/fly/1903/>. [Accessed: 16-Feb-2018].
- [5] P. Chirarattananon, K. Y. Ma, and R. J. Wood, "Adaptive control for takeoff, hovering, and landing of a robotic fly," in *2013 IEEE/RSJ International Conference on Intelligent Robots and Systems*, 2013, pp. 3808–3815.
- [6] M. Duduta, D. R. Clarke, and R. J. Wood, "A high speed soft robot based on dielectric elastomer actuators," in *2017 IEEE International Conference on Robotics and Automation (ICRA)*, 2017, pp. 4346–4351.
- [7] B. Gorissen, D. Reynaerts, S. Konishi, K. Yoshida, J.-W. Kim, and M. De Volder, "Elastic Inflatable Actuators for Soft Robotic Applications," *Adv. Mater.*, vol. 29, no. 43, p. n/a-n/a, Nov. 2017.
- [8] L. Hines, K. Petersen, G. Z. Lum, and M. Sitti, "Soft Actuators for Small-Scale Robotics," *Adv. Mater.*, vol. 29, no. 13, p. n/a-n/a, Apr. 2017.
- [9] L. Connelly, Y. Jia, M. L. Toro, M. E. Stoykov, R. V. Kenyon, and D. G. Kamper, "A Pneumatic Glove and Immersive Virtual Reality Environment for Hand Rehabilitative Training After Stroke," *IEEE Trans. Neural Syst. Rehabil. Eng.*, vol. 18, no. 5, pp. 551–559, Oct. 2010.
- [10] E. C. Goldfield *et al.*, "Bio-Inspired Design of Soft Robotic Assistive Devices: The Interface of Physics, Biology, and Behavior," *Ecol. Psychol.*, vol. 24, no. 4, pp. 300–327, Oct. 2012.
- [11] C. Liu, H. Qin, and P. T. Mather, "Review of progress in shape-memory polymers," *J. Mater. Chem.*, vol. 17, no. 16, pp. 1543–1558, 2007.
- [12] W. Wang, H. Rodrigue, and S.-H. Ahn, "Deployable Soft Composite Structures," *Sci. Rep.*, vol. 6, p. srep20869, Feb. 2016.

- [13] P. Berik, W.-Y. Chang, and X. Jiang, "Piezoelectric d36 in-plane shear-mode of lead-free BZT-BCT single crystals for torsion actuation," *Appl. Phys. Lett.*, vol. 110, no. 5, p. 052902, Jan. 2017.
- [14] "Analysis of morphing, multi stable structures actuated by piezoelectric patches - ScienceDirect." [Online]. Available: <http://www.sciencedirect.com/science/article/pii/S0045794907000685>. [Accessed: 19-Oct-2017].
- [15] R. Shankar, T. K. Ghosh, and R. J. Spontak, "Electromechanical Response of Nanostructured Polymer Systems with no Mechanical Pre-Strain," *Macromol. Rapid Commun.*, vol. 28, no. 10, pp. 1142–1147, May 2007.
- [16] H. B. Schreyer, N. Gebhart, K. J. Kim, and M. Shahinpoor, "Electrical activation of artificial muscles containing polyacrylonitrile gel fibers," *Biomacromolecules*, vol. 1, no. 4, pp. 642–647, 2000.
- [17] A. Sydney Gladman, E. A. Matsumoto, R. G. Nuzzo, L. Mahadevan, and J. A. Lewis, "Biomimetic 4D printing," *Nat. Mater.*, vol. 15, no. 4, pp. 413–418, Apr. 2016.
- [18] S. Tibbits, "4D Printing: Multi-Material Shape Change," *Archit. Des.*, vol. 84, no. 1, pp. 116–121, Jan. 2014.
- [19] D. P. Holmes and A. J. Crosby, "Snapping Surfaces," *Adv. Mater.*, vol. 19, no. 21, pp. 3589–3593, Nov. 2007.
- [20] H. Fang, K. W. Wang, and S. Li, "Asymmetric energy barrier and mechanical diode effect from folding multi-stable stacked-origami," *Extreme Mech. Lett.*, vol. 17, no. Supplement C, pp. 7–15, Nov. 2017.
- [21] V. S. C. Chillara and M. J. Dapino, "Stability considerations and actuation requirements in bistable laminated composites," *Compos. Struct.*, vol. 184, pp. 1062–1070, Jan. 2018.
- [22] S. Daynes and P. M. Weaver, "Stiffness tailoring using prestress in adaptive composite structures," *Compos. Struct.*, vol. 106, no. Supplement C, pp. 282–287, Dec. 2013.
- [23] C. Thill, J. Etches, I. Bond, K. Potter, and P. Weaver, "Morphing skins," *Aeronaut. J.*, vol. 112, no. 1129, pp. 117–139, Mar. 2008.
- [24] M. R. Schultz, "A Concept for Airfoil-like Active Bistable Twisting Structures," *J. Intell. Mater. Syst. Struct.*, vol. 19, no. 2, pp. 157–169, Feb. 2008.
- [25] D. N. Betts *et al.*, "Investigation of bistable piezo-composite plates for broadband energy harvesting," *Proc. SPIE*, vol. 8688, Apr. 2013.

- [26] R. L. Harne and K. W. Wang, "A review of the recent research on vibration energy harvesting via bistable systems," *Smart Mater. Struct.*, vol. 22, no. 2, p. 023001, 2013.
- [27] X. Lachenal, S. Daynes, and P. M. Weaver, "Review of morphing concepts and materials for wind turbine blade applications," *Wind Energy*, vol. 16, no. 2, pp. 283–307, Mar. 2013.
- [28] R. H. Baughman *et al.*, "Carbon Nanotube Actuators," *Science*, vol. 284, no. 5418, pp. 1340–1344, May 1999.
- [29] R. H. Baughman, "Conducting polymer artificial muscles," *Synth. Met.*, vol. 78, no. 3, pp. 339–353, Apr. 1996.
- [30] Q.-A. Nguyen, S. J. Jorgensen, J. Ho, and L. Sentis, "Characterization and Testing of an Electrorheological Fluid Valve for Control of ERF Actuators," *Actuators*, vol. 4, no. 3, pp. 135–155, Jun. 2015.
- [31] B. Kim, D.-H. Kim, J. Jung, and J.-O. Park, "A biomimetic undulatory tadpole robot using ionic polymer–metal composite actuators," *Smart Mater. Struct.*, vol. 14, no. 6, p. 1579, 2005.
- [32] A. Ask, A. Menzel, and M. Ristinmaa, "Electrostriction in electro-viscoelastic polymers," *Mech. Mater.*, vol. 50, pp. 9–21, Jul. 2012.
- [33] J. Su, Q. M. Zhang, C. H. Kim, R. Y. Ting, and R. Capps, "Effects of transitional phenomena on the electric field induced strain–electrostrictive response of a segmented polyurethane elastomer," *J. Appl. Polym. Sci.*, vol. 65, no. 7, pp. 1363–1370, Aug. 1997.
- [34] Y. Bar-Cohen, *Electroactive Polymer (EAP) Actuators as Artificial Muscles: Reality, Potential, and Challenges*. SPIE Press, 2004.
- [35] DARPA and SRI International, "Comparison of EAPs with other actuator technologies." .
- [36] R. Shankar, T. K. Ghosh, and R. J. Spontak, "Dielectric elastomers as next-generation polymeric actuators," *Soft Matter*, vol. 3, no. 9, pp. 1116–1129, 2007.
- [37] R. Pelrine, R. Kornbluh, and G. Kofod, "High-Strain Actuator Materials Based on Dielectric Elastomers," *Adv. Mater.*, vol. 12, no. 16, pp. 1223–1225, Aug. 2000.
- [38] W. Yuan *et al.*, "Fault-Tolerant Dielectric Elastomer Actuators using Single-Walled Carbon Nanotube Electrodes," *Adv. Mater.*, vol. 20, no. 3, pp. 621–625, Feb. 2008.
- [39] F. Carpi, P. Chiarelli, A. Mazzoldi, and D. De Rossi, "Electromechanical characterisation of dielectric elastomer planar actuators: comparative evaluation of different electrode materials and different counterloads," *Sens. Actuators Phys.*, vol. 107, no. 1, pp. 85–95, Oct. 2003.

- [40] J. Su, Q. Zhang, P.-C. Wang, A. G. MacDiarmid, and K. J. Wynne, "Preparation and characterization of electrostrictive polyurethane films with conductive polymer electrodes," *Polym. Adv. Technol.*, vol. 9, no. 6, pp. 317–321, Jun. 1998.
- [41] J. Liang, L. Li, X. Niu, Z. Yu, and Q. Pei, "Elastomeric polymer light-emitting devices and displays," *Nat. Photonics*, vol. 7, no. 10, p. 817, Oct. 2013.
- [42] W. C. Röntgen, "Ueber die durch Electricität bewirkten Form- und Volumenänderungen von dielectrischen Körpern," *Ann. Phys.*, vol. 247, no. 13, pp. 771–786, Jan. 1880.
- [43] K. Hess, R. Dandliker, and R. Thalmann, "Deformable Surface Spatial Light Modulator," *Opt. Eng.*, vol. 26, no. 5, p. 265418, May 1987.
- [44] R. Gerhard-Multhaupt *et al.*, "Viscoelastic spatial light modulators and schlieren-optical systems for HDTV projection displays," presented at the Large-Screen and Projection Displays II, 1990, vol. 1255, pp. 69–79.
- [45] R. Pelrine, R. Kornbluh, Q. Pei, and J. Joseph, "High-Speed Electrically Actuated Elastomers with Strain Greater Than 100%," *Science*, vol. 287, no. 5454, pp. 836–839, Feb. 2000.
- [46] R. Pelrine, R. Kornbluh, J. Joseph, R. Heydt, Q. Pei, and S. Chiba, "High-field deformation of elastomeric dielectrics for actuators," *Mater. Sci. Eng. C*, vol. 11, no. 2, pp. 89–100, Nov. 2000.
- [47] Q. Pei, M. Rosenthal, S. Stanford, H. Prahlad, and R. Pelrine, "Multiple-degrees-of-freedom electroelastomer roll actuators," *Smart Mater. Struct.*, vol. 13, no. 5, p. N86, 2004.
- [48] P. Brochu and Q. Pei, "Advances in Dielectric Elastomers for Actuators and Artificial Muscles," *Macromol. Rapid Commun.*, vol. 31, no. 1, pp. 10–36, Jan. 2010.
- [49] G. Kofod, P. Sommer-Larsen, R. Kornbluh, and R. Pelrine, "Actuation Response of Polyacrylate Dielectric Elastomers," *J. Intell. Mater. Syst. Struct.*, vol. 14, no. 12, pp. 787–793, Dec. 2003.
- [50] G. Kofod, W. Wirges, M. Paajanen, and S. Bauer, "Energy minimization for self-organized structure formation and actuation," *Appl. Phys. Lett.*, vol. 90, no. 8, p. 081916, Feb. 2007.
- [51] Mohammad Vatankehah-Varnosfaderani *et al.*, "Bottlebrush elastomers: a promising molecular engineering route to tunable, prestrain-free dielectric elastomers (Conference Presentation)," 2017, vol. 10163, pp. 1016323-10163–1.
- [52] Y. Zhao, J.-W. Zha, L.-J. Yin, Z.-S. Gao, Y.-Q. Wen, and Z.-M. Dang, "Remarkable electrically actuation performance in advanced acrylic-based dielectric elastomers without pre-strain at very low driving electric field," *Polymer*.

- [53] S. M. Ha, W. Yuan, Q. Pei, R. Pelrine, and S. Stanford, "Interpenetrating Polymer Networks for High-Performance Electroelastomer Artificial Muscles," *Adv. Mater.*, vol. 18, no. 7, pp. 887–891, Apr. 2006.
- [54] T. G. McKay, E. Calius, and I. A. Anderson, "The dielectric constant of 3M VHB: a parameter in dispute," presented at the Electroactive Polymer Actuators and Devices (EAPAD) 2009, 2009, vol. 7287, p. 72870P.
- [55] 3M, "Technical data of 3M VHB tapes." 2015.
- [56] S. J. A. Koh *et al.*, "Mechanisms of large actuation strain in dielectric elastomers," *J. Polym. Sci. Part B Polym. Phys.*, vol. 49, no. 7, pp. 504–515, Apr. 2011.
- [57] S. Michel, X. Q. Zhang, M. Wissler, C. Löwe, and G. Kovacs, "A comparison between silicone and acrylic elastomers as dielectric materials in electroactive polymer actuators," *Polym. Int.*, vol. 59, no. 3, pp. 391–399, Mar. 2010.
- [58] M. Zhenyi, J. I. Scheinbeim, J. W. Lee, and B. A. Newman, "High field electrostrictive response of polymers," *J. Polym. Sci. Part B Polym. Phys.*, vol. 32, no. 16, pp. 2721–2731, Dec. 1994.
- [59] Y. Kurita, T. Ueda, T. Kasazaki, and T. Hirai, "Polyurethane elastomer actuator," US5977685 A, 02-Nov-1999.
- [60] J. Su, Q. M. Zhang, and R. Y. Ting, "Space-charge-enhanced electromechanical response in thin-film polyurethane elastomers," *Appl. Phys. Lett.*, vol. 71, no. 3, pp. 386–388, Jul. 1997.
- [61] S. Arora, T. Ghosh, and J. Muth, "Dielectric elastomer based prototype fiber actuators," *Sens. Actuators Phys.*, vol. 136, no. 1, pp. 321–328, May 2007.
- [62] R. Shankar, T. K. Ghosh, and R. J. Spontak, "Electroactive Nanostructured Polymers as Tunable Actuators," *Adv. Mater.*, vol. 19, no. 17, pp. 2218–2223, Sep. 2007.
- [63] M. Duduta, R. J. Wood, and D. R. Clarke, "Multilayer Dielectric Elastomers for Fast, Programmable Actuation without Prestretch," *Adv. Mater.*, vol. 28, no. 36, pp. 8058–8063, Sep. 2016.
- [64] G. Ouyang, K. Wang, and X. Y. Chen, "TiO<sub>2</sub> nanoparticles modified polydimethylsiloxane with fast response time and increased dielectric constant," *J. Micromechanics Microengineering*, vol. 22, no. 7, p. 074002, 2012.
- [65] Q. M. Zhang *et al.*, "An all-organic composite actuator material with a high dielectric constant," *Nature*, vol. 419, no. 6904, p. nature01021, Sep. 2002.

- [66] Y. Chen *et al.*, “Enhanced dielectric properties of amino-modified-CNT/polyimide composite films with a sandwich structure,” *J. Mater. Chem. A*, vol. 2, no. 34, pp. 14118–14126, 2014.
- [67] G. Gallone, F. Carpi, D. De Rossi, G. Levita, and A. Marchetti, “Dielectric constant enhancement in a silicone elastomer filled with lead magnesium niobate–lead titanate,” *Mater. Sci. Eng. C*, vol. 27, no. 1, pp. 110–116, Jan. 2007.
- [68] B. Wang *et al.*, “Two-layer materials of polyethylene and a carbon nanotube/cyanate ester composite with high dielectric constant and extremely low dielectric loss,” *Carbon*, vol. 54, pp. 224–233, Apr. 2013.
- [69] T. Li, Z. Zou, G. Mao, and S. Qu, “Electromechanical Bistable Behavior of a Novel Dielectric Elastomer Actuator,” *J. Appl. Mech.*, vol. 81, p. 1019, Nov. 2013.
- [70] X. Fang, A. Li, O. Yildiz, H. Shao, P. D. Bradford, and T. K. Ghosh, “Enhanced anisotropic response of dielectric elastomer actuators with microcombed and etched carbon nanotube sheet electrodes,” *Carbon*, vol. 120, no. Supplement C, pp. 366–373, Aug. 2017.
- [71] X. Fang, “Anisotropic D-EAP Electrodes and their Application in Spring Roll Actuators,” Ph.D., North Carolina State University, United States -- North Carolina, 2017.
- [72] M. Benslimane, H.-E. Kiil, and M. J. Tryson, “Electromechanical properties of novel large strain PolyPower film and laminate components for DEAP actuator and sensor applications,” presented at the Electroactive Polymer Actuators and Devices (EAPAD) 2010, 2010, vol. 7642, p. 764231.
- [73] C. Keplinger, M. Kaltenbrunner, N. Arnold, and S. Bauer, “Röntgen’s electrode-free elastomer actuators without electromechanical pull-in instability,” *Proc. Natl. Acad. Sci.*, vol. 107, no. 10, pp. 4505–4510, Mar. 2010.
- [74] P. Chakraborti, H. A. K. Toprakci, P. Yang, N. Di Spigna, P. Franzon, and T. Ghosh, “A compact dielectric elastomer tubular actuator for refreshable Braille displays,” *Sens. Actuators Phys.*, vol. 179, pp. 151–157, Jun. 2012.
- [75] J.-S. Plante, M. Santer, S. Dubowsky, and S. Pellegrino, “Compliant Bistable Dielectric Elastomer Actuators for Binary Mechatronic Systems,” pp. 121–126, Jan. 2005.
- [76] S. Shian, K. Bertoldi, and D. R. Clarke, “Dielectric Elastomer Based ‘Grippers’ for Soft Robotics,” *Adv. Mater.*, vol. 27, no. 43, pp. 6814–6819, Nov. 2015.
- [77] Y. Liu, L. Shi, L. Liu, Z. Zhang, and J. Leng, “Inflated dielectric elastomer actuator for eyeball’s movements: fabrication, analysis and experiments,” presented at the Electroactive Polymer Actuators and Devices (EAPAD) 2008, 2008, vol. 6927, p. 69271A.

- [78] I. A. Anderson, T. C. H. Tse, T. Inamura, B. M. O'Brien, T. McKay, and T. Gisby, "A soft and dexterous motor," *Appl. Phys. Lett.*, vol. 98, no. 12, p. 123704, Mar. 2011.
- [79] C. T. Nguyen, H. Phung, T. D. Nguyen, H. Jung, and H. R. Choi, "Multiple-Degrees-of-Freedom Dielectric Elastomer Actuators for Soft Printable Hexapod Robot," *Sens. Actuators Phys.*, Oct. 2017.
- [80] J.-G. Lee, J. Ryu, H. Lee, and M. Cho, "Saddle-shaped, bistable morphing panel with shape memory alloy spring actuator," *Smart Mater. Struct.*, vol. 23, no. 7, p. 074013, 2014.
- [81] A. J. Lee, A. Moosavian, and D. J. Inman, "A piezoelectrically generated bistable laminate for morphing," *Mater. Lett.*, vol. 190, no. Supplement C, pp. 123–126, Mar. 2017.
- [82] K. Oliver, A. Seddon, and R. S. Trask, "Morphing in nature and beyond: a review of natural and synthetic shape-changing materials and mechanisms," *J. Mater. Sci.*, vol. 51, no. 24, pp. 10663–10689, Dec. 2016.
- [83] I. Burgert and P. Fratzl, "Actuation systems in plants as prototypes for bioinspired devices," *Philos. Trans. R. Soc. Lond. Math. Phys. Eng. Sci.*, vol. 367, no. 1893, pp. 1541–1557, Apr. 2009.
- [84] D. E. Ingber, "Tensegrity and mechanotransduction," *J. Bodyw. Mov. Ther.*, vol. 12, no. 3, pp. 198–200, Jul. 2008.
- [85] J. Braam, "In touch: plant responses to mechanical stimuli," *New Phytol.*, vol. 165, no. 2, pp. 373–389, Feb. 2005.
- [86] J. Engelberth, "Mechanosensing and signaltransduction in tendrils," *Adv. Space Res.*, vol. 32, no. 8, pp. 1611–1619, Oct. 2003.
- [87] C. Dawson, J. F. V. Vincent, and A.-M. Rocca, "How pine cones open," *Nat. Lond.*, vol. 390, no. 6661, p. 668, Dec. 1997.
- [88] S. Armon, E. Efrati, R. Kupferman, and E. Sharon, "Geometry and Mechanics in the Opening of Chiral Seed Pods," *Science*, vol. 333, no. 6050, pp. 1726–1730, Sep. 2011.
- [89] F. Haas, S. Gorb, and R. J. Wootton, "Elastic joints in dermapteran hind wings: materials and wing folding," *Arthropod Struct. Dev.*, vol. 29, no. 2, pp. 137–146, Apr. 2000.
- [90] R. L. Marsh, J. M. Olson, and S. K. Guzik, "Mechanical performance of scallop adductor muscle during swimming," *Nature*, vol. 357, no. 6377, pp. 411–413, Jun. 1992.
- [91] C. V. Anderson, "Off like a shot: scaling of ballistic tongue projection reveals extremely high performance in small chameleons," *Sci. Rep.*, vol. 6, Jan. 2016.

- [92] J. H. de Groot and van L. Johan L, "Evidence for an elastic projection mechanism in the chameleon tongue," *Proc. R. Soc. Lond. B Biol. Sci.*, vol. 271, no. 1540, pp. 761–770, Apr. 2004.
- [93] C. V. Anderson and S. M. Deban, "Ballistic tongue projection in chameleons maintains high performance at low temperature," *Proc. Natl. Acad. Sci.*, vol. 107, no. 12, pp. 5495–5499, Mar. 2010.
- [94] G. N. Askew and R. L. Marsh, "The mechanical power output of the pectoralis muscle of blue-breasted quail (*Coturnix chinensis*): the in vivo length cycle and its implications for muscle performance," *J. Exp. Biol.*, vol. 204, no. 21, pp. 3587–3600, Nov. 2001.
- [95] M. Runge, J. Rittweger, C. R. Russo, H. Schiessl, and D. Felsenberg, "Is muscle power output a key factor in the age-related decline in physical performance? A comparison of muscle cross section, chair-rising test and jumping power," *Clin. Physiol. Funct. Imaging*, vol. 24, no. 6, pp. 335–340, Nov. 2004.
- [96] T. Kleinteich and S. N. Gorb, "Tongue adhesion in the horned frog *Ceratophrys* sp.," *Sci. Rep.*, vol. 4, Jun. 2014.
- [97] S. Felton, M. Tolley, E. Demaine, D. Rus, and R. Wood, "A method for building self-folding machines," *Science*, vol. 345, no. 6197, pp. 644–646, Aug. 2014.
- [98] D. P. Holmes, M. Roché, T. Sinha, and H. A. Stone, "Bending and twisting of soft materials by non-homogenous swelling," *Soft Matter*, vol. 7, no. 11, pp. 5188–5193, 2011.
- [99] J. Mu, C. Hou, H. Wang, Y. Li, Q. Zhang, and M. Zhu, "Origami-inspired active graphene-based paper for programmable instant self-folding walking devices," *Sci. Adv.*, vol. 1, no. 10, p. e1500533, Nov. 2015.
- [100] C. S. Haines *et al.*, "Artificial Muscles from Fishing Line and Sewing Thread," *Science*, vol. 343, no. 6173, pp. 868–872, Feb. 2014.
- [101] Y. Zhong *et al.*, "Reversible Humidity Sensitive Clothing for Personal Thermoregulation," *Sci. Rep.*, vol. 7, p. 44208, Mar. 2017.
- [102] K. Kumar *et al.*, "A chaotic self-oscillating sunlight-driven polymer actuator," *Nat. Commun.*, vol. 7, p. ncomms11975, Jul. 2016.
- [103] M. Yamada *et al.*, "Photomobile Polymer Materials: Towards Light-Driven Plastic Motors," *Angew. Chem. Int. Ed.*, vol. 47, no. 27, pp. 4986–4988, Jun. 2008.
- [104] T. Chen, J. Mueller, and K. Shea, "Integrated Design and Simulation of Tunable, Multi-State Structures Fabricated Monolithically with Multi-Material 3D Printing," *Sci. Rep.*, vol. 7, p. srep45671, Mar. 2017.

- [105] V. Gimenez-Pinto, F. Ye, B. Mbanga, J. V. Selinger, and R. L. B. Selinger, "Modeling out-of-plane actuation in thin-film nematic polymer networks: From chiral ribbons to auto-origami boxes via twist and topology," *Sci. Rep.*, vol. 7, Mar. 2017.
- [106] W. Wang, L. Yao, T. Zhang, C.-Y. Cheng, D. Levine, and H. Ishii, "Transformative Appetite: Shape-Changing Food Transforms from 2D to 3D by Water Interaction Through Cooking," in *Proceedings of the 2017 CHI Conference on Human Factors in Computing Systems*, New York, NY, USA, 2017, pp. 6123–6132.
- [107] M.-L. Dano and M. W. Hyer, "Snap-through of unsymmetric fiber-reinforced composite laminates," *Int. J. Solids Struct.*, vol. 39, no. 1, pp. 175–198, Jan. 2002.
- [108] B. Wang and K. S. Fancey, "A bistable morphing composite using viscoelastically generated prestress," *Mater. Lett.*, vol. 158, no. Supplement C, pp. 108–110, Nov. 2015.
- [109] S. Daynes, C. G. Diaconu, K. D. Potter, and P. M. Weaver, "Bistable Prestressed Symmetric Laminates," *J. Compos. Mater.*, vol. 44, no. 9, pp. 1119–1137, May 2010.
- [110] A. DeSimone, "Spontaneous bending of pre-stretched bilayers," *Meccanica*, pp. 1–8, Aug. 2017.
- [111] V. S. C. Chillara and M. J. Dapino, "Bistable morphing composites with selectively prestressed laminae," presented at the Behavior and Mechanics of Multifunctional Materials and Composites 2017, 2017, vol. 10165, p. 101650Y.
- [112] A. I. Egunov, J. G. Korvink, and V. A. Luchnikov, "Polydimethylsiloxane bilayer films with an embedded spontaneous curvature," *Soft Matter*, vol. 12, no. 1, pp. 45–52, 2016.
- [113] S. Daynes, A. Grisdale, A. Seddon, and R. Trask, "Morphing structures using soft polymers for active deployment," *Smart Mater. Struct.*, vol. 23, no. 1, p. 012001, 2014.
- [114] M. Schlecht and K. Schulte, "Advanced Calculation of the Room-Temperature Shapes of Unsymmetric Laminates," *J. Compos. Mater.*, vol. 33, no. 16, pp. 1472–1490, Aug. 1999.
- [115] Michael W. Hyer, "Some Observations on the Cured Shape of Thin Unsymmetric Laminates," *J. Compos. Mater.*, vol. 15, no. 2, pp. 175–194, Mar. 1981.
- [116] C. S. Sousa, P. P. Camanho, and A. Suleman, "Analysis of multistable variable stiffness composite plates," *Compos. Struct.*, vol. 98, no. Supplement C, pp. 34–46, Apr. 2013.
- [117] X. Lachenal, P. M. Weaver, and S. Daynes, "Multi-stable composite twisting structure for morphing applications," *Proc R Soc A*, vol. 468, no. 2141, pp. 1230–1251, May 2012.
- [118] B.-C. Yoseph, "WorldWide ElectroActive Polymers," Jul-2000.

- [119] R. Kornbluh, R. Pelrine, J. Joseph, R. Heydt, Q. Pei, and S. Chiba, "High-field electrostriction of elastomeric polymer dielectrics for actuation," in *Proc. SPIE*, 1999, vol. 3669, pp. 149–161.
- [120] C. Keplinger, T. Li, R. Baumgartner, Z. Suo, and S. Bauer, "Harnessing snap-through instability in soft dielectrics to achieve giant voltage-triggered deformation," *Soft Matter*, vol. 8, no. 2, pp. 285–288, 2012.
- [121] M. Tadayon, S. Amini, A. Masic, and A. Miserez, "The Mantis Shrimp Saddle: A Biological Spring Combining Stiffness and Flexibility," *Adv. Funct. Mater.*, vol. 25, no. 41, pp. 6437–6447, Nov. 2015.
- [122] K. A. Seffen and S. D. Guest, "Prestressed Morphing Bistable and Neutrally Stable Shells," *J. Appl. Mech.*, vol. 78, no. 1, pp. 011002-011002–6, Oct. 2010.
- [123] P. Portela, P. Camanho, P. Weaver, and I. Bond, "Analysis of morphing, multi stable structures actuated by piezoelectric patches," *Comput. Struct.*, vol. 86, no. 3, pp. 347–356, Feb. 2008.
- [124] C.-K. Cho, W.-J. Hwang, K. Eun, S.-H. Choa, S.-I. Na, and H.-K. Kim, "Mechanical flexibility of transparent PEDOT:PSS electrodes prepared by gravure printing for flexible organic solar cells," *Sol. Energy Mater. Sol. Cells*, vol. 95, no. 12, pp. 3269–3275, Dec. 2011.
- [125] A. S. Kasat and V. Varghese, "Finite element analysis of prestressed concrete beams," *Int. J. Adv. Technol. Civ. Eng.*, vol. 1(3), no. 4, 2012.
- [126] M. Pezulla, G. P. Smith, P. Nardinocchi, and D. P. Holmes, "Geometry and mechanics of thin growing bilayers," *Soft Matter*, vol. 12, no. 19, pp. 4435–4442, 2016.
- [127] M. Pezulla, N. Stoop, X. Jiang, and D. P. Holmes, "Curvature-driven morphing of non-Euclidean shells," *Proc R Soc A*, vol. 473, no. 2201, p. 20170087, May 2017.
- [128] M. S. Madhukar and L. T. Drzal, "Fiber-Matrix Adhesion and Its Effect on Composite Mechanical Properties: II. Longitudinal (0°) and Transverse (90°) Tensile and Flexure Behavior of Graphite/Epoxy Composites," *J. Compos. Mater.*, vol. 25, no. 8, pp. 958–991, Aug. 1991.
- [129] A. Chemami, K. Bey, J. Gilgert, and Z. Azari, "Behaviour of composite sandwich foam-laminated glass/epoxy under solicitation static and fatigue," *Compos. Part B Eng.*, vol. 43, no. 3, pp. 1178–1184, Apr. 2012.

## APPENDICES

## Appendix A Theoretical Analysis of Bistable Shape

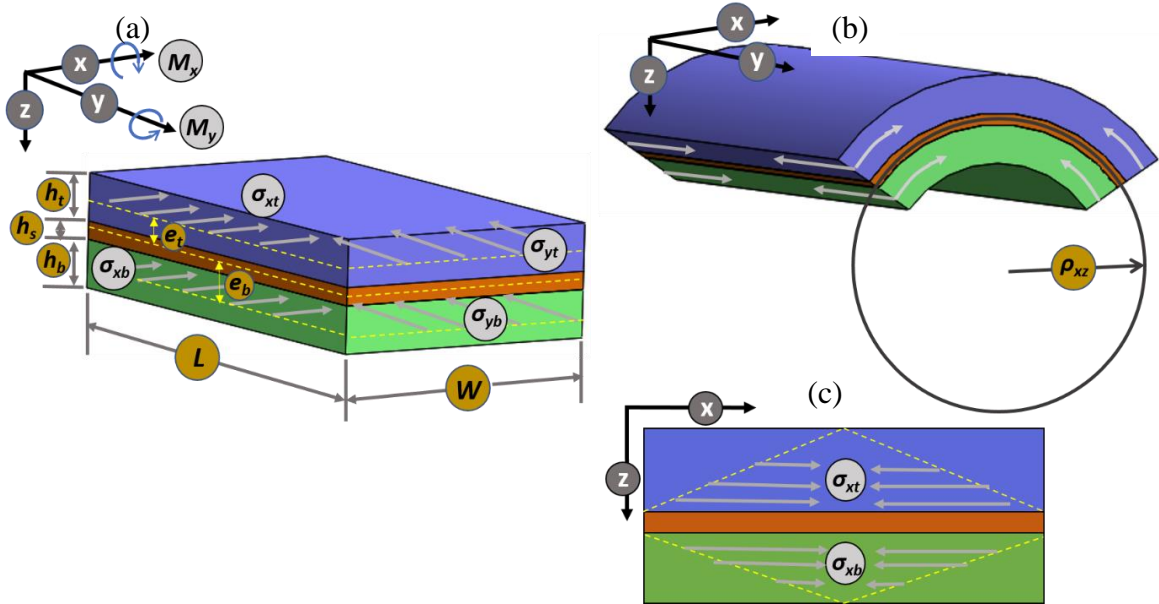


**Figure A 1. Prestrain-induced bending of a trilayered laminate.** (a) A rectangular prestrained laminate. (b) Upon removal of external constraint, the laminate self-equilibrates into state 1. (c) Stress distribution along z axis, on xz-plane for example.

In order to analyze and predict the resulting  $C_{xz}$  of the laminate we followed the standard force balance analysis used in determining stress distribution and camber in prestrained concrete structures [125]. We linear bending behavior of the laminate as well as ignore the loading due to gravity. The resulting equilibrium  $C_{xz}$  was expressed as following,

$$C_{xz} = \frac{1}{\rho_{xz}} = \frac{M_y}{EI_y} = \frac{P_{xb}e_b - P_{xt}e_t}{EI_y} \quad \text{Equation A 1}$$

Parameters are shown in Figure A 1.  $P_{xb}$ ,  $P_{xt}$  are contractile forces induced by prestrain along x axis, and  $EI_y$  is the flexural rigidity of the laminates about y axis, which resists bending in xz-plane.

Due to the sharp stiffness difference between the support layer and the prestrained DE layers ( $E_s \gg E_a$ ), there are two issues required to be addressed: **1>**. Flexural rigidity of a composite laminates; **2>**. Compressive stress distribution profile along z axis ( $\sigma_{xb}(z)$ ).

We assume the neutral axis of the laminate goes through the midplane of the support layer. For issue (1), the flexural rigidity ( $EI_y$ ) of the laminates about y axis was derived according to the symmetric sandwiched laminate [129] with minor modification:

$$EI_y = L \int E z^2 dz = \left( \frac{LE_a h_t^3}{12} + \frac{LE_a h_t^3}{3} \right) + \left( \frac{LE_a h_b^3}{12} + \frac{LE_a h_b^3}{3} \right) + \frac{LE_s h_s^3}{12} \quad \text{Equation A 2}$$

$\frac{LE_a h_t^3}{12} + \frac{LE_a h_t^3}{3}$  is the contribution of the top layer to the bending stiffness of the laminate.

$\frac{LE_a h_b^3}{12} + \frac{LE_a h_b^3}{3}$  is the contribution of the bottom layer to the bending stiffness of the laminate.

$\frac{LE_s h_s^3}{12}$  is the contribution of the support layer to the bending stiffness of the laminate.

For issue (2), we assumed that the induced stress distribution along z axis ( $\sigma_{xb}(z)$ ) linear decreases from  $\sigma_{xb}(z=0) = \sigma_{xb}$  ( $\sigma_{xb}$  is obtained from true stress-strain curve of VHB 4905) to  $\sigma_{xb}(z=h_b) = 0$ , when compressive stress is away from support plane (Fig 10b), expressing as,

$$\sigma_{xb}(z) = -\frac{\sigma_{xb}}{h_b} z + \sigma_{xb}, \quad z = [0, h_b] \quad \text{Equation A 3}$$

Because  $\epsilon_{xt}$  is 0% throughout the experiment, the bending moment ( $M_y$ ) induced by stress in x direction and stress distribution profile along z direction then is expressed as following,

$$M_y = L \int_0^{h_b} \left( -\frac{\sigma_{xb}}{h_b} z + \sigma_{xb} \right) z dz - L \int_0^{h_t} \left( -\frac{\sigma_{xt}}{h_t} z + \sigma_{xt} \right) z dz = \frac{L \sigma_{xb} h_b^2}{6} \quad \text{Equation A 4}$$

Finally, combining the expression for  $M_y$  and  $EI_y$ , the curvature  $C_{xz}$  can be expressed as,

$$C_{xz} = \frac{2(\sigma_{xb} h_b^2 - \sigma_{xt} h_t^2)}{5E_a(h_t^3 + h_b^3) + E_s h_s^3} \quad \text{Equation A 5}$$

## Appendix B Theoretical Analysis of Bistability

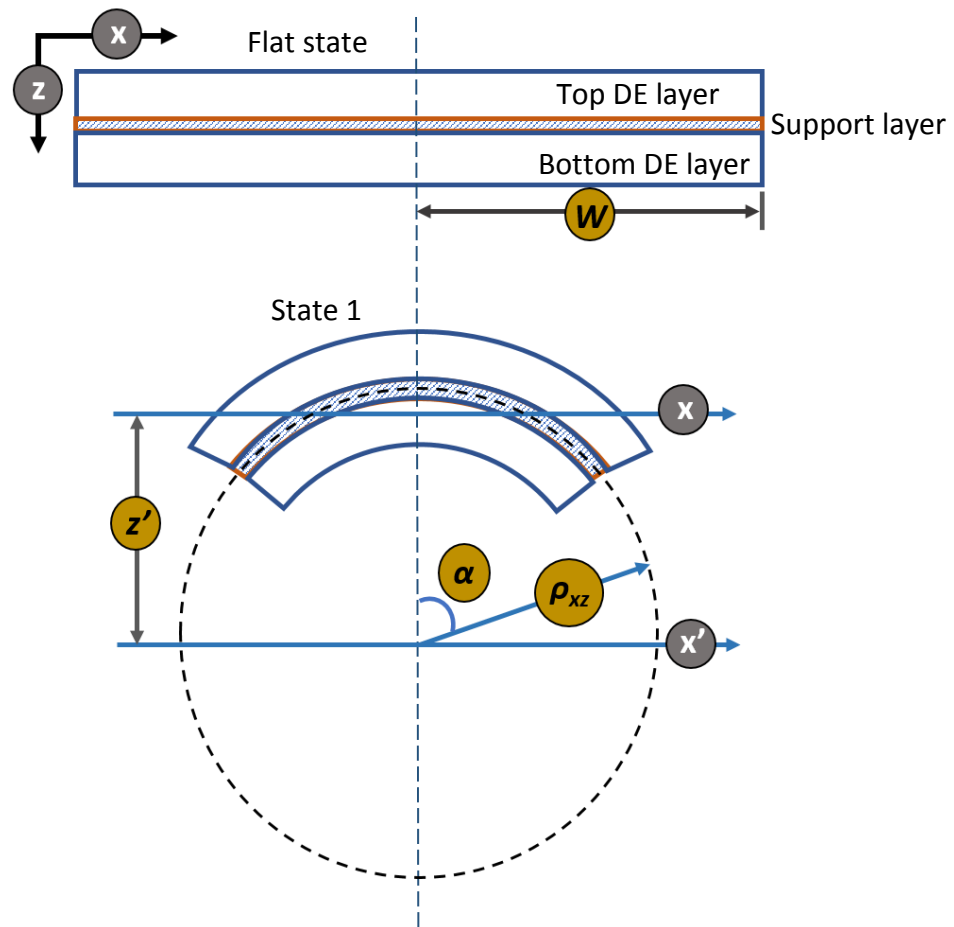


Figure A 2. Schematic of the tape spring actuator in flat status and state 1 in xz-plane.

We investigated two parameters that can effectively predict the range of bistability, when we varied the prestrain combination: **1**>. Calculated curvature of the laminate in yz-plane ( $C_{yz}$ ) in state 1, according to the Euler-Bernoulli beam theory we utilized in calculating the curvature in xz-plane of the tape spring in state 1 ( $C_{xz}$ ); **2**>. Ratio of bending moments about x and y axes ( $M_x/M_y$ ).

In order to calculate  $C_{yz}$  in state 1 (Figure A 2), which is too small to be observed in the experiment, we utilized the Euler-Bernoulli beam theory,  $C_{yz} = M_x/EI_x$ . Using same assumptions we made previously for deriving  $M_y$  (mid plane of support layer as neutral plane and linear reduction of stress along z axis),  $M_x$  can be expressed as,

$$M_x = W \int_0^{h_t} \left(-\frac{\sigma_{yt}}{h_t} z + \sigma_{yt}\right) z dz - W \int_0^{h_b} \left(-\frac{\sigma_{yb}}{h_b} z + \sigma_{yb}\right) z dz = \frac{W\sigma_{yt}h_t^2 - W\sigma_{yb}h_b^2}{6}$$

Equation A 6

In the analysis of flexural rigidity of the bent laminate about x axis ( $EI_x$ ), we simplified the Young's modulus of the trilayered laminate by following the "Rule-of-Mixture" used in determining stiffness of fiber-reinforced epoxy composites [4],  $E_c = E_m V_m + E_f V_f$ , where  $E_c$ ,  $E_m$ ,  $E_f$  are Young's modulus of composite, matrix and fiber, respectively, and  $V_m$ ,  $V_f$  are the volume fraction of the matrix and fiber in the composite, respectively. Similarly in our case, the Young's modulus of the trilayered laminate can be written as,

$$E = E_s \frac{h_s}{h} + E_a \frac{h_b + h_t}{h} \quad \text{Equation A 7}$$

Note that all the parameters are listed in Table 3-1. For the calculation of  $I_x$ , as shown in Figure A 2, we assume that the tape spring actuator in state 1 in xz-plane is an arc of a ring.  $X'$  axis is the axis goes through the center of the ring, while x axis goes through the center of mass of the laminates and is parallel to  $x'$  axis. According to the parallel axis theorem, the moment of inertia ( $I_x$ ) of the tape spring actuator in state 1 about x axis is written as,

$$I_x = I_{x'} - Az'^2 \quad \text{Equation A 8}$$

while A is the area of the cross-section of the laminates in xz-plane, and  $z'$  is the distance between x axis and  $x'$  axis.

As shown in Figure A 2, the moment of inertia of the tape spring actuator in state 1 about x axis ( $I_x$ ) is written as,

$$I_x = 2 \int_0^\alpha \int_{\rho_{xz}-h_b}^{\rho_{xz}+h_t} (\rho_{xz} \cos \theta)^2 * \rho_{xz} d\rho_{xz} d\theta - Az'^2 \quad \text{Equation A 9}$$

Where most all parameters are well defined in the previous context, Figure A 2, and Table 3-1,  $\alpha = W/2\rho_{xz}$ ,  $A = \alpha[(\rho_{xz} + h_t)^2 - (\rho_{xz} - h_b)^2]$ , and  $z' = \rho \sin \alpha / \alpha$ .

According to the calculation, there are several parameters important in determining the  $I_x$ , including the cross-sectional area ( $A$ ), ratio of thickness of DE layers to the laminates' thickness,  $C_{xz}$ , and the position of the center of mass of the actuator. The result of  $I_x$  calculation plotted and compared to the experimentally obtained  $C_{xz}$ , shown in Figure A 3. When we changed the prestrains of the DE layer, the trend of  $I_x$  change is similar to the trend of  $C_{xz}$  change, meaning the  $C_{xz}$  is predominant in determining the  $I_x$ , and thus crucial in the bending stiffness of the actuator.

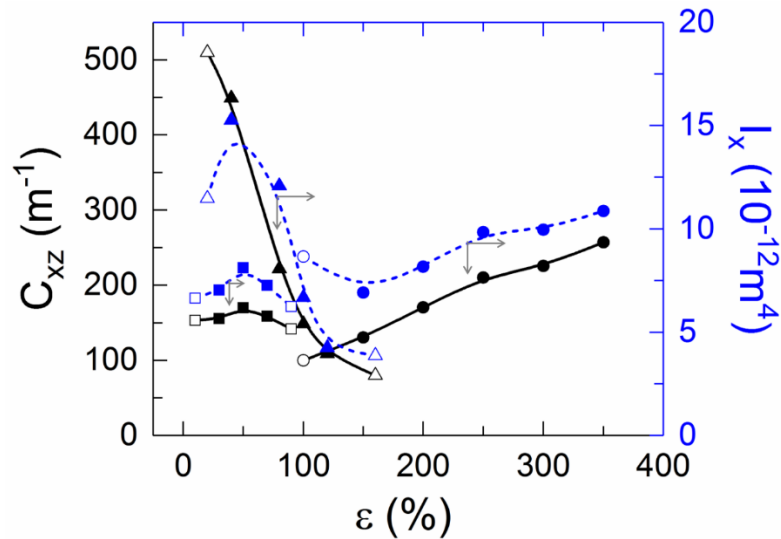


**Figure A 3. Experimental  $C_{xz}$  and  $I_x$  of tape spring actuator plotted as a function of prestrains.** Black solid lines represent the curvature change, and blue dashed lines represent moment of inertia ( $I_x$ ) change. Rectangles represent the actuators with  $\epsilon_{xb}$  as a variable, while  $\epsilon_{yb} = 100\%$ ,  $\epsilon_{xt} = 0\%$ ,  $\epsilon_{yt} = 200\%$ . Triangles represent actuators with  $\epsilon_{yb}$  as a variable, while  $\epsilon_{xb} = 50\%$ ,  $\epsilon_{xt} =$

0%,  $\epsilon_{yt} = 200\%$ . Circles represent actuators with  $\epsilon_{yt}$  as a variable, while  $\epsilon_{xb} = 50\%$ ,  $\epsilon_{yb} = 100\%$ ,  $\epsilon_{xt} = 0\%$ . Filled dots are bistable samples, and unfilled dots are monostable samples.

The ratio of bending moment is calculated as follows:

$$\frac{M_x}{M_y} = \frac{W\sigma_{yt}h_t^2 - W\sigma_{yb}h_b^2}{L\sigma_{xb}h_b^2 - L\sigma_{xt}h_t^2} \quad \text{Equation A 10}$$